Dissertation

submitted to the

Combined Faculties for the Natural Sciences and for Mathematics

of the Ruperto-Carola University of Heidelberg, Germany

for the degree of

Doctor of Natural Sciences

Put forward by

MS.-PHYS. DARYA TROFIMOVA

born in Minsk

Date of Oral Examination: 1.7.2015

Towards four dimensional visualization of air-water gas exchange

Referees:

Prof. Dr. BERND JÄHNE

Prof. Dr. KURT ROTH

Abstract: In this work, the transport of a trace gas through the air-water interface at a turbulent wavy water surface has been studied. A novel experimental technique for the visualization of the mass boundary layer has been developed. The technique is based on a system of chemical reactions to feature a binary representation of concentration fields. By penetrating through the air-water interface, the alkaline trace gas ammonia changes the temporal equilibrium of the chemical species and hence the local pH value. The shift in the pH value is visualized by the fluorescent pH indicator Pyranine.

The technique to measure a controllable fraction of the water-side mass boundary layer thickness has been verified by simulations and vertical profile measurements with a high temporal and spatial resolution. The experiments were conducted at a linear wind-wave facility at different conditions and concentrations. The suitable concentration of the fluorescent dye and the initial pH value, favorable for maintaining a step-shaped drop of the intensity at a certain depth, have been estimated to be 10^{-5} mol/L and 4, respectively.

In additional measurements at the large annular facility Aeolotron, the simplified turbulent structures are observed from below of the facility with a trifocal camera set-up. With the multiple view geometry concept, stereo based reconstruction has been performed by using the images from two cameras. Through the estimated disparity maps the third spatial dimension of the fluorescent turbulent structures is retrieved. Therefore, the processes driving air-water gas exchange can be investigated in the three spatial and the temporal dimensions.

Zusammenfassung: In dieser Arbeit wurde der Transport eines Gases von Luft ins Wasser an einer turbulenten und welligen Wasseroberfläche untersucht. Dafür wurde eine neue Visualisierungstechnik entwickelt, welche die Massengrenzschicht sichtbar macht. Die Technik basiert auf mehreren chemischen Reaktionen die eine binäre Repräsentation von Konzentrationsfeldern ermöglicht. Das alkalische Gas Ammoniak diffundiert durch die Phasengrenze und verschiebt dadurch das Reaktionsgleichgewicht und erhöht den lokalen pH-Wert. Diese Änderung des pH-Werts wird durch den Fluoreszenzindikator Pyranin sichtbar gemacht.

Die Technik, die es ermöglicht einen kontrollierbaren Teil der wasserseitigen Grenzschicht zu visualisieren, wurde durch Simulationen und vertikale Konzentrationsprofilmessungen, mit einer hohen zeitlichen und räumlichen Auflösung, verifiziert. Die Experimente wurden an einem linearen Wind-Wellen-Kanal bei verschiedenen Bedingungen und Konzentrationen durchgeführt. Die geeignetsten Konzentrationen des Fluoreszenzindikators und des pH-Wertes zu Beginn der Messung, um einen scharfen Gradienten im Intensitätsprofil bei einer bestimmten Tiefe zu erhalten, wurden bestimmt und sind 10^{-5} mol/L und 4.

In weiteren Messungen am großen ringförmigen Wind-Wellen-Kanal Aeolotron wurden mit einem trifokalen Aufbau unter dem Kanal vereinfachte turbulenten Strukturen beobachtet. Eine stereobasierte Rekonstruktion wurde durch zwei Kameras mit dem Konzept der multiple-view geometry realisiert. Durch die so erhaltenen disparity maps wurden die fluoreszierenden turbulenten Strukturen in den drei Ortsdimensionen berechnet. Dadurch ist es möglich die Prozesse, die den Austausch von Gasen zwischen Luft und Wasser beeinflussen, in den drei Richtungen sowie der Zeit zu untersuchen.

Contents

1. Introduction

1.1. Motivation: Fields of Application

The distribution of various chemical species between the big compartments of the Earth's environment - ocean and atmosphere - is of a great importance for understanding and interpreting climate change. The most obvious example is an intake of an important greenhouse gas, carbon dioxide, by the ocean. According to Khatiwala et al. (2013), the total amount of 155 PgC of anthropogenic carbon has been taken from the atmosphere by the ocean. The increase of carbon dioxide dissolved in the ocean causes the ongoing decrease in the pH value of the Earth's oceans (Doney et al., 2009), which is well known as ocean acidification problem.

Aside this example, mass transfers of chemical substances between the atmosphere and oceans, lakes, and streams are known to play a decisive role in many of the great bio-, geo- and chemical cycles, that condition the environment. The experimental study of the fluxes between ocean and atmosphere is challenging, as the physical mechanism of interfacial gas exchange is essentially complex for several reasons, e.g.:

- fluid motions on both sides of the interface are highly turbulent, which determines a stochastic feature of the transport on a wide range of spatial and temporal scales
- the interface may be disturbed and distorted into irregular shapes and, hence, interacts with the turbulence structures in both aqueous and gaseous boundary layers.

So far, no clear physically-based model describing the exchange processes through the air-water interface at smooth and wavy water surfaces has been established. However, there is a number of known near-surface turbulent processes having direct influence on a gas exchange rate - interaction of shear stress and waves causes Langmuir circulations (Thorpe, 2004; Veron and Melville, 2001), small waves and microcsale wave breaking lead to surface renewal events (Kock et al., 2012), wave breaking induces the presence of bubbles (Zappa et al., 2001). It is considered, that investigating the processes mentioned above provides with better insight into air-water gas exchange. Consequently, the visualization of concentration fields of a trace gas through the air-water interface in three spatial and the temporal dimensions is essential.

1.2. Overview of Previous Work

Most of the work done in the area of visualisation techniques concerns Laser Induced Fluorescence (LIF) methods that have recently made progress for gas exchange study. Similar to the current

studies LIF techniques have been applied for measuring one dimensional concentration profiles by Friedl (2013) and Herzog (2010). However, LIF techniques are hard to employ for visualization of air-water gas transfer across the mass boundary layer at a free water surface. Because of the necessity of high spatial and temporal resolution in order to resolve the mass boundary layer and fast turbulent processes at a highly dynamical surface, visualization of concentration fields are possible in one or rarely in two dimensional space only, that does not yield the full understanding of the mechanisms of a gas exchange. To name a few, the research on planar LIF techniques was done by Crimaldi (2008); Dani et al. (2007); Friedl et al. (2015); Mühlfriedel and Baumann (2000). Additionally, LIF techniques are impractical at large scale measurements, as the visualization of concentration fields is complicated by the waves and maintaining high spatial resolution laser-based systems is no longer feasible.

Achieving the full picture of a gas exchange in three spatial dimensions is of interest. An amount of progress towards three dimensional visualization of turbulent flows involves Particle Image Velocimetry (PIV) techniques, that investigate the momentum transfer across air-water interface. Planar PIV visualization was examined by Fabry (1998); Wang et al. (2012). Estimation of out-of-plane velocity component from PIV was managed with two 2D plane measurements by Braud et al. (2004) and Raffel et al. (1995). Close to three dimensional velocity field visualization was accomplished by Van Doorne et al. (2003) with application of the Taylor-hypothesis. Similar to current work, stereo-based visualization was done by Turney et al. (2009) using dual-camera set-up for PIV measurements. Yet, to current knowledge, no visualization technique covers the full three spatial dimensional presentation of turbulent processes.

In comparison to PIV techniques that investigate momentum transfer, LIF techniques capture the fields of mass transfer directly and, therefore, are more suitable for understanding the processes of a gas exchange.

1.3. Objectives of the Thesis

Among existing investigations concerning gas exchange, this thesis is placed within the laboratory experiments devoted to development of advanced visualization techniques. The scope of the thesis is to develop and optimize a visualization technique suitable for investigation of air-water gas exchange in three spatial dimensions at the scales larger than the mass boundary layer thickness.

For that purpose, a novel LIF technique is developed for the visualization of simplified turbulent structures of air-water gas transfer. The LIF technique for concentration profiles is modified in such a way, that the concentration fields of the observed trace gas have binary representation. In order to confirm the capability of the technique, the measurements of concentration profiles with high temporal and spatial resolution are required and are of scope of the first part of the thesis.

Additionally, the employment of the technique for the visualization measurements with multiple projections is of interest. The purpose of the experiments with trifocal set-up is to demonstrate the ability of capturing and extracting the information about turbulent structures in third spatial dimension using stereo vision algorithms.

1.4. Structure of the Thesis

Within the mentioned above scope of this thesis, it refers to two separate tasks - verification of novel LIF technique by conducting the measurement of one dimensional concentration profiles and visualization of mass boundary layer in three spatial dimensions. Accordingly, the main part of the thesis is divided in two units (chap. 4 and chap. 5). The complete thesis is organized as follows:

- Chap. 2 is partitioned into two sections. Sec. 2.1 covers the basic physical concepts necessary to understand the phenomena of air-water gas exchange. The diffusion and turbulent mechanisms of the transport within the mass boundary layer are described. Sec. 2.2 is focused on fundamental terminology and representation of the multiple view geometry concept. This part is essential for the visualization of a gas exchange in three spatial dimensions with the trifocal set-up.
- Chap. 3 is dedicated to the visualization technique applied in this thesis. Basic principles of LIF technique, the choice of the pH indicator and the trace gas are explained in sec. 3.1. Employment of the novel LIF technique for the visualization of the mass boundary layer is given in sec. 3.2.
- Chap. 4 describes two approaches accomplished for verification of the novel LIF technique - simulations of mean concentration profiles predicted by the gas exchange models (sec. 4.1) and the experiments at the linear wind-wave facility for measuring one dimensional concentration profiles (sec. 4.2). The chapter also presents the results of the experiments and draws the first conclusions on operability of the visualization technique.
- Chap. 5 covers the experiments conducted at the annual Aeolotron facility (sec. 5.1) and the data processing steps implemented to estimate the disparity maps for the acquired data (sec. 5.2). Sec. 5.3 presents the results of the measurements with the trifocal set-up and the processing of the data.
- In chap. 6, the operability of the novel visualization technique and applicability of the trifocal set-up for reconstruction purposes are discussed.
- Chap. 7 covers the summary of the results and outlook of the presented work.

2. Theory

The chapter is divided into two sections. Sec. 2.1 gives an introduction to the theory of a gas exchange at the air-water interface. Here, the main processes governing gas exchange are presented - molecular and turbulent diffusion. Gas exchange parameters and gas exchange models for mean concentration profiles are described. Sec. 2.2 covers the theory of multiple view geometry with basics of projective geometry and the details of stereo imaging. This part is essential to the experiments performed with a trifocal view registration set-up.

2.1. Gas Exchange

The physics of air-water gas exchange is complex. Yet the diffusive transfer of a gases through air-water surface can be described using the concentration flux. As gas exchange is controlled by diffusion and turbulent processes, this section covers the description of molecular diffusion and turbulence. The characteristics of gas exchange such as transfer velocity, mass boundary layer thickness and friction velocity are presented. Sec. 2.1.4 gives a summary of models for mean concentration profiles describing the transport processes at different conditions.

2.1.1. Molecular Diffusion

Molecular diffusion is due to the thermal motion of particles. It describes the net flux of molecules from the region of high concentration to the region of low concentration. For a liquid at rest this process can be expressed in a form of Fick's first law:

$$\overrightarrow{j_c} = -D\nabla c, \tag{2.1}$$

where $\overrightarrow{j_c}$ is the mass flux, ∇c is the gradient of the concentration with the proportionality constant D being a diffusion constant or diffusivity. For a steady state condition, the flux is constant and homogeneous, which results in linear variations of the concentration. The diffusion constant D depends on the transported trace gas and physical properties of the medium. Mathematically D is defined as:

$$D = \frac{1}{3}ul, \tag{2.2}$$

where l is the mean free path and u is the mean thermal velocity.

For a fluid in motion, the flux of a substance can be described by the sum of an advective flux

$\overrightarrow{j_c}^{ad} = \overrightarrow{u}\nabla c$ and the diffusive flux $\overrightarrow{j_c}^{diff} = -D\Delta c$:

$$\overrightarrow{j_c} = \overrightarrow{j_c}^{ad} + \overrightarrow{j_c}^{diff} = \overrightarrow{u}\nabla c - D\Delta c \tag{2.3}$$

With the mass conservation equation written in differential form as:

$$\frac{\partial c}{\partial t} = -\overrightarrow{\nabla}\overrightarrow{j_c} \tag{2.4}$$

and the condition for incompressible fluids:

$$\overrightarrow{\nabla}\overrightarrow{u} = 0, \tag{2.5}$$

the eq. (2.1) can be written in a form of Fick's second law:

$$\frac{\partial c}{\partial t} + \overrightarrow{u}\nabla c = D\Delta c, \tag{2.6}$$

where the term $\overrightarrow{u}\nabla c$ represents the transport of the concentration by velocity field $\overrightarrow{u}$.

The transport of momentum and heat can be described in analogy to the mass transport with formulas similar to eq. (2.1). Since the heat transfer was not of interest in this work, the further description covers mostly mass and momentum transfer processes. The transport of momentum can be described by Newton's law of viscosity (Csanady, 1973):

$$\overrightarrow{j_m} = -\nu\nabla(\rho\overrightarrow{u}), \tag{2.7}$$

where $\overrightarrow{j_m}$ is a flux of momentum, ρ is the density of the medium, $\overrightarrow{u}$ is the velocity field with proportion coefficient ν denoting the kinematic viscosity.

The equation equivalent to eq. (2.6) for momentum transport can be derived from Navier-Stokes equation assuming the case for no external forces and pressure gradients:

$$\frac{\partial\overrightarrow{u}}{\partial t} + (\overrightarrow{u}\cdot\nabla)\overrightarrow{u} = \nu\Delta\overrightarrow{u}. \tag{2.8}$$

Worth mentioning here is that the diffusion constants for gaseous and aqueous media differ significantly. Typically, diffusion constants in gases and liquids are in the order of $10^{-5}\,\mathrm{m}^2/\mathrm{s}$ and $10^{-9}\,\mathrm{m}^2/\mathrm{s}$, respectively. Smaller values for diffusion constants in liquid media explain the difficulty of investigating the mechanisms of a gas exchange, as the processes are happening on the scale 100 times smaller, than in the gaseous media.

2.1.2. Turbulence

In contrast to diffusion, turbulent transport is driven by statistical fluctuation of the velocity field. The length scale of the turbulent eddies is scaled by the distance to the interface. Far away from the water surface the eddies are larger than close to the interface. As the turbulence scales close to the interface appear smaller than the mean free path of the particles, i.e. the distance travelled by a moving particles between the collisions, the diffusion exceeds the turbulent transport closer to the

interface. Further away from the interface the sizes of the turbulent eddies become larger resulting in dominant turbulent transport.

The turbulent transport can be described in analogy to the diffusion transport. This can be maintained by Reynolds decomposition. Here the decomposition steps are presented for the mass transport, i.e. the concentration field, and velocity field. The main concept of Reynolds decomposition is to split the fluid motion and concentration transport mechanism into averaged and fluctuated parts according to the equations:

$$c = \overline{c} + c' \tag{2.9}$$

$$\overrightarrow{u} = \overline{\overrightarrow{u}} + \overrightarrow{u}' \tag{2.10}$$

The fluctuation parts of the concentration field c' and the velocity field $\overrightarrow{u}'$ are defined such that the time averaged values vanish:

$$\overline{c'} = 0 \tag{2.11}$$

$$\overline{\overrightarrow{u}'} = 0 \tag{2.12}$$

This allows to simplify the Fick's second law eq. (2.6) and Navier-Stokes equation (2.8) by substituting in the sum of the steady component and perturbations to the concentration profile and to the velocity field, respectively. Assuming the stationary one-dimensional current in x-direction, the mean values of the simplified equations are taking following forms:

$$\frac{\partial \overline{c}}{\partial t} = \frac{\partial}{\partial z}(D\frac{\partial \overline{c}}{\partial z} - \overline{c'\omega'}) \tag{2.13}$$

$$\frac{\partial \overline{u}}{\partial t} = \frac{\partial}{\partial z}(\nu\frac{\partial \overline{u}}{\partial z} - \overline{u'\omega'}) \tag{2.14}$$

with u and ω denoting the components of the velocity field in stream-wise (x-) and vertical (z-) directions. With the continuity equation (2.4), the constant scalar flux density of the concentration can be expressed as:

$$j_c = -D\frac{\partial \overline{c}}{\partial z} + \overline{c'\omega'}. \tag{2.15}$$

By comparison the eq. (2.1) for the concentration flux density, which includes the diffusion transport only, with the eq. (2.15), the term $\overline{c'\omega'}$ can be explained as a measure of the turbulent transport. Assuming that the turbulent transport is proportional to the gradient of the concentration profile, it can be expressed in a form of turbulent diffusivity K_c with the following equation:

$$\overline{c'\omega'} = -K_c\frac{\partial \overline{c}}{\partial z} \tag{2.16}$$

Including the turbulence transport alongside with the diffusion transport into eq. (2.13), the

equation of the mass transfer can be formulated as following:

$$j_c = -(D + K_c(z))\frac{\partial \overline{c}}{\partial z} \tag{2.17}$$

In analogy to the mass transport, the momentum transport can be described as a sum of diffusive and turbulent parts:

$$j_m = -(\nu + K_m(z))\frac{\partial \overline{u}}{\partial z}, \tag{2.18}$$

where the turbulent viscosity K_m corresponds to the following equation:

$$\overline{u'\omega'} = -K_m\frac{\partial \overline{u}}{\partial z}. \tag{2.19}$$

2.1.3. Gas Exchange Parameters

Transfer velocity

Due to the strong reduction of $K_c(z)$ next to the interface ($K_c(z) \to 0$), the area close to the interface originates the barrier for the gas exchange. This allows the simplified definition of the quantity, that macroscopically characterizes the rate of air-water gas transfer. It can be deducted from the eq. (2.17) by integrating over the distance from the depth z_1 to the depth z_2:

$$c(z_2) - c(z_1) = -j_c \int_{z_1}^{z_2} \frac{1}{D + K_c(z)} \mathrm{d}z \tag{2.20}$$

By definition, the flux j_c is proportional to the concentration gradient Δc with the proportionality constant k, which is called transfer velocity:

$$j_c = k \cdot \Delta c \tag{2.21}$$

With combining eq. (2.20) and eq. (2.21), the transfer velocity for the distance between the depths z_1 and z_2 can be expressed with following equation:

$$k = \frac{1}{\int_{z_1}^{z_2}(K_c(z) + D)^{-1}\mathrm{d}z} \tag{2.22}$$

Generally, the transfer velocity does depend on the distance of interest defined by z_1 and z_2. However, the term $(K_c(z) + D)$ is much smaller close to the air-water interface which strongly affects the integral value in eq. (2.22). Arranging the close to the interface area being included in the region between z_1 and z_2, the transfer velocity is not strongly dependent on the integrated boundaries.

The inverse measure of the transfer velocity is the transfer resistance:

$$R = k^{-1} \tag{2.23}$$

The transfer resistance is used as an intuitive representation of the transfer velocity. In analogy to the resistance in electrical circuits, the transfer resistances R_i of different depth layers add up

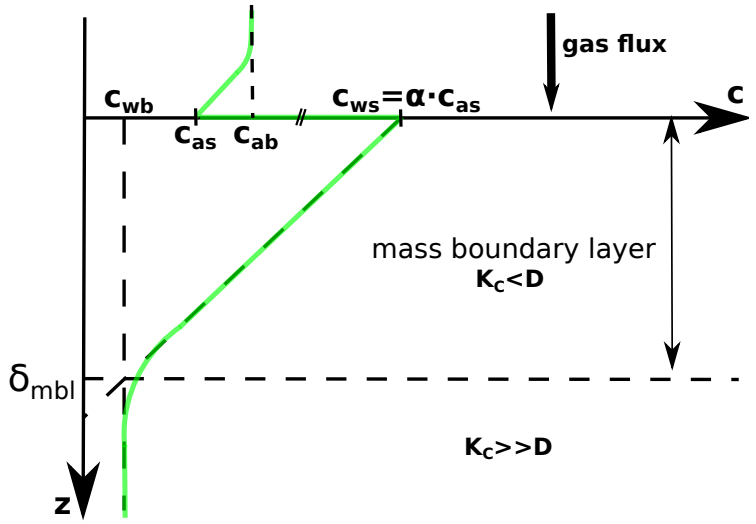

Figure 2.1.: Sketch of the mean concentration profile at the air-water interface. The mass boundary layer is defined as the depth of the intersection of the concentration gradient at the water surface and the vertical line at the value of the bulk concentration. The plot is valid for a trace gas with the solubility $\alpha > 1$.

to the total resistance of the layers. The total transfer resistance of the air-water gas exchange is partitioned in an air-sided and water-sided resistances (for more details see Kräuter (2011b)).

Mass boundary layer

The thickness of the mass boundary layer is defined as a ratio of the concentration gradient between the surface and bulk concentrations to the gradient at the water surface:

$$\delta_{mbl} = \frac{\Delta c}{-\frac{\partial \overline{c}}{\partial z}|_{z=0}} = \frac{D\Delta c}{j_c} \tag{2.24}$$

with the condition $-\frac{\partial \overline{c}}{\partial z}|_{z=0} \neq 0$. Fig. 2.1 shows the graphical sketch of a concentration profiles in the air and water side for an invasion of a gas to the water. The intersection between the concentration gradient at the surface and the vertical line at the value of the bulk concentration defines the depth of the mass boundary layer.

With eq. (2.21) the mass boundary layer can be written as:

$$\delta_{mbl} = \frac{D}{k}, \tag{2.25}$$

stating that the thickness of the boundary layer is proportional to the inverse transfer velocity.

Similarly to the thickness of the mass boundary layer as a characteristic space scale, a time constant for the process of a gas exchange can be defined as:

$$t_* = \frac{\delta_{mbl}}{k} \tag{2.26}$$

Time scale t_* can be explained as a time needed for the molecules to cross through the mass boundary layer of the thickness δ_{mbl} with velocity k. According to Jähne (2009), typical values for t_* are of 0.04-4.0 s.

Solubility

Analysing the transport processes through air-water interfaces, one needs to consider the solubility of gases. The solubility, also called as a partition coefficient, of a trace gas is relevant to the process of gas exchange since it determines whether the main resistance of transport is at the water or air side. It is based on equilibrium between the gaseous and liquid phases and defined as a ratio of the concentration at the surface in the air and water side:

$$c_{ws} = \alpha \cdot c_{as} \tag{2.27}$$

In the definition above, the solubility α is dimensionless and the concentration is usually given in mol/L. The solubility allows to distinguish the gases to three categories: slightly soluble gases with $\alpha \ll 1$, intermediate soluble gases with $\alpha \approx 1$ and highly soluble gases with $\alpha \gg 1$. Fig. 2.1 presents the sketch of the concentration profile in the water and air side for a highly soluble gases with $\alpha \gg 1$ that ensures the jump of the concentration at the water surface from c_{as} to c_{ws}.

Schmidt Number

The comparison of the mass and momentum transport can be presented with a dimensionless quantity called Schmidt number, defined as a ratio of the kinematic viscosity of the fluid and diffusion constant of a soluble gas:

$$Sc = \frac{\nu}{D} \tag{2.28}$$

With the Schmidt number in the air is roughly equal to 1 as $D \approx \nu$, in the water typical Schmidt numbers are much higher and vary in a range from the values of 100 up to the values of 2000 (Jähne and Münnich, 1980).

Equivalently, the turbulent Schmidt number can be defined as a ratio of the turbulent viscosity K_m and the turbulent diffusivity K_c:

$$Sc_t = \frac{K_m}{K_c} \tag{2.29}$$

Friction Velocity

The momentum flux j_m is caused by the shear stress τ on the water surface. To compare the velocity of a flow to the shear stress, the shear velocity, also called friction velocity, is defined with following equation:

$$u_* = \sqrt{\frac{|\tau|}{\rho}} \tag{2.30}$$

The friction velocity describes the transport of vertical momentum towards the water surface caused by the wind-induced shear stress.

Low wind velocities result in a flat water surface while high wind velocities - in wavy conditions at the water surface. Waves influence on a gas exchange as a decay of the waves to the turbulence and wave-breaking events. Wave fields interact with the wind fields appearing as surface rough-

ness. It has been shown in (Kiefhaber, 2014) that the small-scale processes increase gas transfer velocities and near-surface turbulence.

2.1.4. Gas Exchange Models

The section presents the models for mean concentration profiles of air-water gas exchange. The modelling of the transfer through the air-water interface needs to include the diffusion and turbulent transport mechanisms.

Here, only essential for the current study models are presented - film model for comprehension reasons, more complex models such as small-eddy model and surface renewal model at free and rigid interfaces with the additional assumption for the fluctuation surface renewal model. The model concepts are taken either from physical chemistry (film model) or from fluid dynamics of flow above a solid surface (complex models). A detailed description of the boundary conditions for the concentration at the interface can be found in Friedl (2013) and Münsterer (1996).

The modelling of the concentration profiles is based on solving the differential equation (2.17) with estimating the $c(z)$ dependency. For this reason, the assumptions concerning $K_c(z)$ function are ought to be made.

Film Model

The simplest model for the mean concentration depth profile is the film model. It was first presented by Lewis and Whitman (1924). The main assumption of the model states that the mass transport is caused by the molecular diffusion in a stagnant film at both sides of the air-water interface. Outside the film, the transport is governed by the turbulent processes and molecular diffusion can be neglected entirely. The schematic illustration of the film model is presented in fig. 2.2.

The mathematical expression for the mean concentration profile can be achieved by setting the constant K_c to zero and integration eq. (2.17) over the depth from $z = 0$ till the mass boundary layer thickness $z = \delta_{mbl}$.

With assuming the concentration of a gas at the water surface and in the bulk being equal to c_s and c_b, respectively, the mean concentration profile has a linear behaviour that can be expressed as:

$$c(z) = (c_s - c_b) \cdot (1 - \frac{z}{\delta_{mbl}}) + c_b \tag{2.31}$$

Within the mass boundary layer the concentration $c(z)$ decreases linearly from the value c_s to the value c_b. Below the mass boundary layer, the concentration is constant and equal to c_b due to an assumption of well-mixed water bulk. According to the film model the transfer velocity can be calculated by integrating eq. (2.22) over the same boundary conditions:

$$k = \frac{1}{\int_0^{\delta_{mbl}} D^{-1} \mathrm{d}z} = \frac{D}{\delta_{mbl}} \tag{2.32}$$

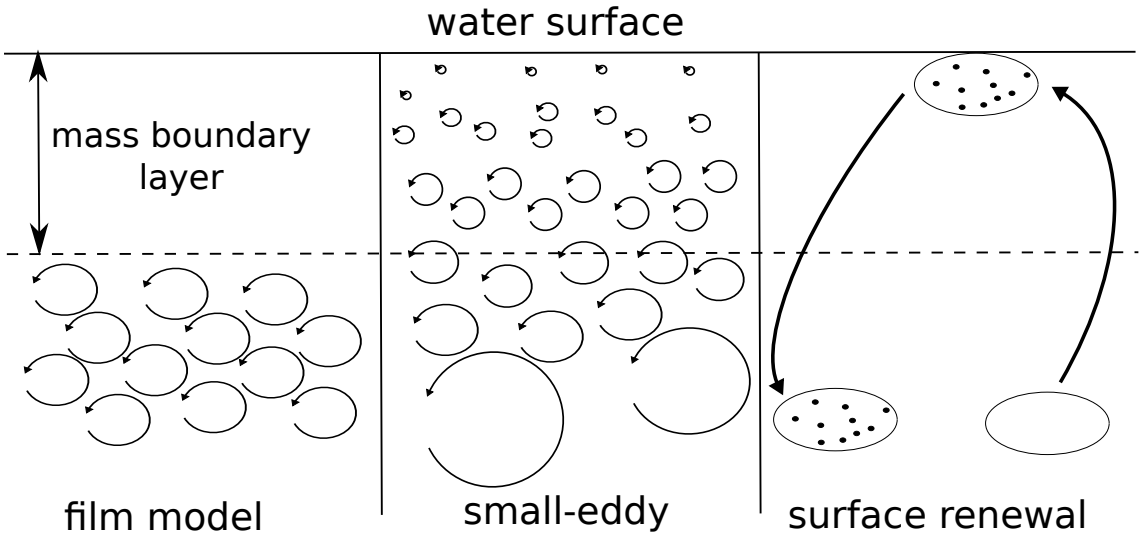

Figure 2.2.: Graphical representation of the models considered in the study. The size of the sketched eddies does not represent the space scales of the eddies, but the scale of the turbulent diffusivity. For the film model, the turbulent diffusivity is zero within the mass boundary layer and constant in the water bulk. For the small eddy model, the turbulent diffusivity decreases with the distance from the air-water interface. The sketch for the surface renewal model illustrates the transfer mechanism of the water pattern from the close to the interface area to the water bulk.

Small-Eddy Model

The small-eddy model assumes that the transport mechanisms are described with the turbulent diffusivity $K_c(z)$ varying over depth. The $K_c(z)$ at the air-water interface is agreed to be zero and presumes to grow dependent on the distance to the interface. The sketch of the water-sided mechanisms assumed for the model is shown in fig. 2.2. The derivation of the small-eddy model is given by Coantic (1986). Here, only main assumptions essential for the model are presented.

The core assumption for the models is the state of the turbulent diffusivity at various boundary condition - rigid and free interfaces. The expression for the turbulent diffusivity can be obtained by solving the averaged transport equation (2.13):

$$K_c(z) = -\frac{j_c}{\frac{\partial \overline{c}}{\partial z}} - D \tag{2.33}$$

The concept of a rigid and a free liquid-gas interface behaviour depending on the surface conditions was first underlined in Davies (1972). It stated that at low wind speeds the interface exhibits the solid smooth wall behaviour due to presence of some impurities. As soon as the surface film is broken by significant wind action, the air-water interface is considered as "free". With this aspect the turbulent diffusivity changes unevenly for different surface behaviour.

With the boundary conditions at **a rigid interface**, the turbulent diffusivity carries a cube dependence on the distance to the interface (Coantic, 1986):

$$K_c(z) \propto z^3 \tag{2.34}$$

At **a free interface**, the relation of the $K_c(z)$ constant and the depth z is quadratic (Coantic,

1986):

$$K_c(z) \propto z^2 \tag{2.35}$$

Eq. (2.34) and eq. (2.35) can be written in the general form as:

$$K_c(z) = \alpha_m z^m \tag{2.36}$$

for solving the averaged transport equations for the concentration with a given turbulent diffusivity:

$$\frac{\partial \overline{c}}{\partial t} = \frac{\partial}{\partial z}\Big[\frac{\partial \overline{c}}{\partial z}(D + K_c(z))\Big] \tag{2.37}$$

The differential equation (2.37) is solved for the steady state condition ($\frac{\partial \overline{c}}{\partial t} = 0$) assuming the following boundary conditions for the concentration:

$$\overline{c}(0) = c_s, \quad \overline{c}(\infty) = c_b \quad \text{and} \quad \frac{\partial c}{\partial z}|_{z=0} = -\frac{c_s - c_b}{\delta_{mbl}} \tag{2.38}$$

In Jähne et al. (1989), the solution for the turbulence diffusivity, i.e. the parameter α_m, is presented as following:

$$\alpha_m = \Big(\frac{\pi}{msin(\pi/m)}\Big)^m \tag{2.39}$$

The mean concentration profiles can be achieved by solving the averaged transport equation (2.37) within the proper definition of turbulence diffusivity $K_c(z)$ in dependence on the behaviour of the interface and eq. (2.38) of a steady state condition.

- **Free Interface (m = 2)** For a free interface the mean concentration profile with $m = 2$ for the steady state is written as:

$$c(z) = (c_s - c_b)\frac{2}{\pi} \cdot arccot(\frac{\pi}{2}\frac{z}{\delta_{mbl}}) + c_b \tag{2.40}$$

- **Rigid interface (m = 3)** For a rigid interface the mean concentration profile with $m = 3$ follows the expression:

$$\begin{aligned} c(z) = (c_s - c_b)\Big[\frac{3}{4} + \frac{3}{2\pi} \cdot arctan\Big(\frac{1}{\sqrt{3}} - \frac{4\pi}{9}\frac{z}{\delta_{mbl}}\Big) - \frac{\sqrt{3}}{2\pi} ln(9 + 2\sqrt{3}\pi\frac{z}{\delta_{mbl}}) \\ + \frac{\sqrt{3}}{4\pi} ln(3(27 - 6\sqrt{3}\pi\frac{z}{\delta_{mbl}} + 4\pi^2\frac{z^2}{{\delta_{mbl}}^2}))\Big] + c_b \end{aligned} \tag{2.41}$$

Surface Renewal Model

The model of surface renewal events was first proposed by Higbie (1935) and developed further by Danckwerts (1951) and Harriott (1962). The usual view of a presence of a stagnant film is

rejected. Instead it is assumed that the surface is renewed with a fresh liquid from the water bulk with a certain probability of this event. The transport between surface renewal appearances is assumed to comply with diffusion mechanisms. The core concept of the surface renewal model is shown schematically in fig. 2.2.

According to Jähne (1985), the general form for the renewal rate λ is defined as a function of the depth to the power of p and written as:

$$\lambda = \gamma_p z^p \tag{2.42}$$

For $p = 0$, the renewal rate is constant over the depth. For $p = 1$, the renewal rate grows linearly with the distance from the interface. The mathematical representation of the model can be expressed with the turbulent term in eq. (2.13) replaced by a product of the concentration c and the renewal rate λ:

$$\frac{\partial \overline{c}}{\partial t} = D\frac{\partial^2 \overline{c}}{\partial z^2} - \lambda c \tag{2.43}$$

To solve the differential equation (2.43), the same boundary conditions as for small-eddy model are used to calculate the mean concentration profiles at a free and a rigid interfaces.

- **Free interface (p = 0)** The mean concentration profile at a free interface according to the model of surface renewal events is written as:

$$c(z) = (c_s - c_b) \cdot \exp(-\frac{z}{\delta_{mbl}}) + c_b \tag{2.44}$$

- **Rigid interface (p = 1)** For a rigid interface, the mean concentration profile was first presented by Jähne et al. (1989):

$$c(z) = (c_s - c_b) \cdot \frac{1}{Ai(0)} Ai(-\frac{Ai(0)}{Ai'(0)}\frac{z}{\delta_{mbl}}) + c_b \tag{2.45}$$

- **Fluctuation profiles**

  The model of fluctuation profiles is based on an assumption that the transport mechanism at the air-water interface is controlled by periodic surface renewal events in addition to diffusion processes. The detailed description of the proposed model and the boundary conditions considered for the concentration and its gradient at the interface can be found in Friedl (2013).

  The transport equation for diffusion processes within the boundary conditions has a solution in the form of complementary error function erfc:

$$c(z,t) = (c_s - c_b) \cdot \mathrm{erfc}(\frac{z}{2\sqrt{Dt}}) + c_b \tag{2.46}$$

  The surface renewal events occur as periodic scenes with a time intervals τ. At the time $t = 0$, the concentration is assumed to be constant and equal to c_b. With increasing time,

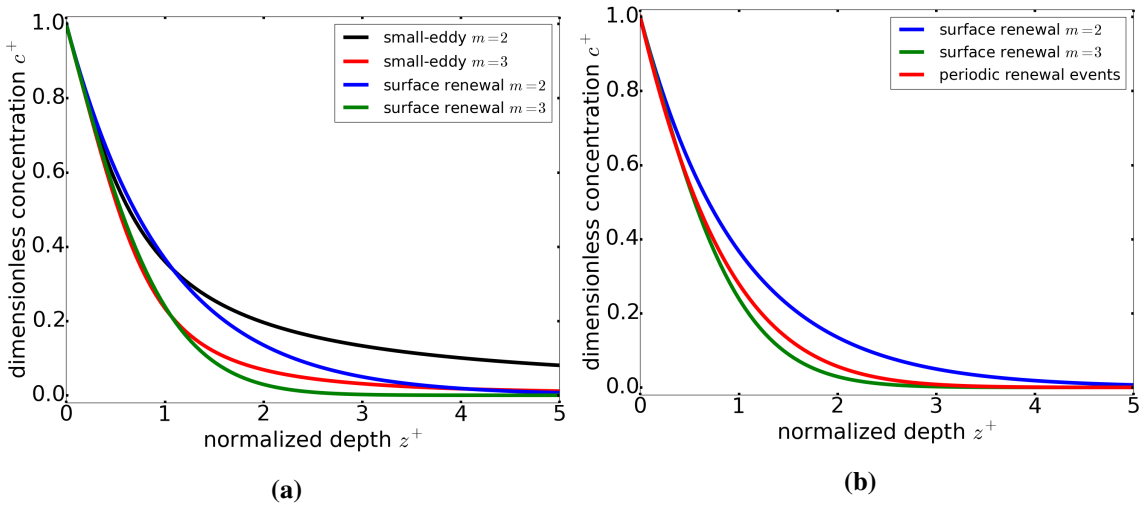

Figure 2.3.: Mean concentration profiles for the small-eddy and surface renewal models with different boundary conditions. The profiles are presented in dimensionless coordinates - normalized concentration $(c-c_b)/(c_s-c_b)$ and normalized depth z/δ_{mbl}. (a) Comparison of the small-eddy and surface renewal models for the boundary conditions at free and rigid interface. (b) Mean concentration profiles for surface renewal model at free and rigid interfaces along with the model for fluctuation profiles with periodic renewal events.

the concentration gradient at the surface decreases. After time period τ, the renewal event occurs and the concentration return to the value c_b. The solution for the mean concentration profile can be written as (Friedl, 2013):

$$c(z) = (c_s - c_b)\Big[-\frac{1}{\sqrt{\pi}}\frac{z}{\delta_{mbl}}\exp(-\frac{z^2}{4\delta_{mbl}^2}) + \frac{1}{2}(2+\frac{z^2}{\delta_{mbl}^2})\cdot \mathrm{erfc}(\frac{z}{2\delta_{mbl}})\Big] + c_b \tag{2.47}$$

Fig. 2.3a presents the shape of the concentration profiles for small-eddy and surface renewal models with the boundary conditions at a free and rigid interfaces. For illustrative reasons, the mean concentration profiles are plotted in dimensionless units for the concentration c_+ and depth z_+ defined as:

$$c_+ = \frac{c-c_b}{c_s-c_b} \quad \text{and} \quad z_+ = \frac{z}{\delta_{mbl}} \tag{2.48}$$

Fig. 2.3b shows the surface renewal model at a free and rigid interfaces along the model for the fluctuation profiles with periodic surface renewal events. The advantage of the model for fluctuation profiles prevails due to incorporation of the temporal behaviour of the concentration profiles in the fluctuation term.

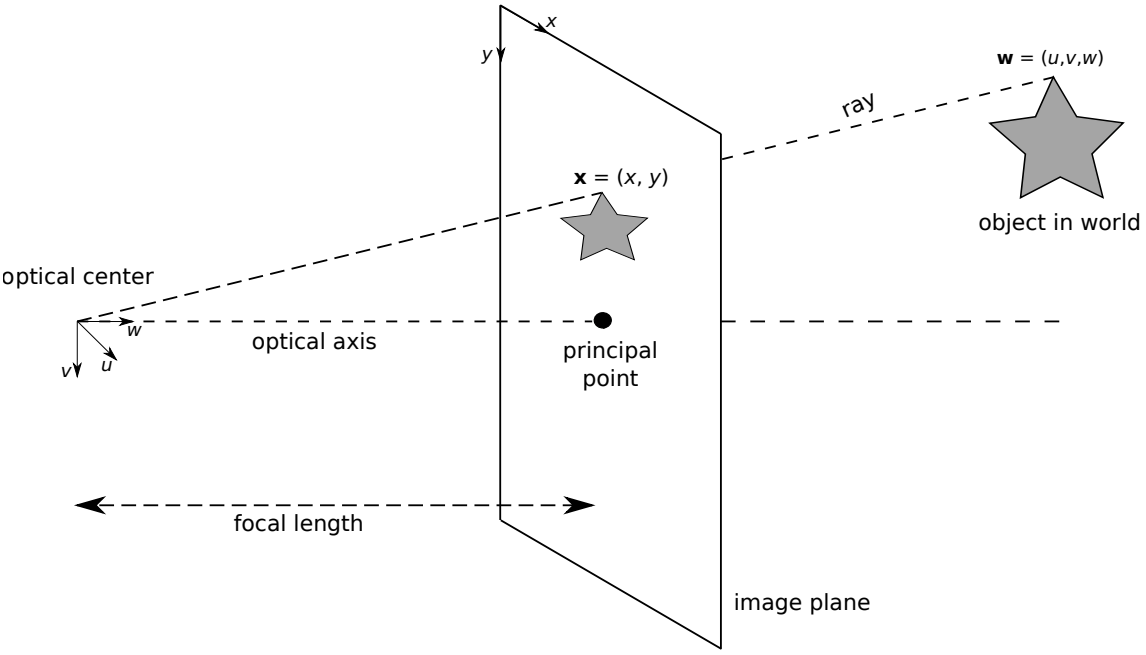

Figure 2.4.: Pin-hole camera model. The optical center is at the origin of the 3D world coordinate system. The image plane is displaced along the *w*-axis which is the optical axis. The position, where the optical axis strikes the image plane, is called principal point.

2.2. Multiple View Geometry

The section gives an overview of the basic representation, terminology and notation for multiple view geometry. It starts with a fundamental description of a projective transformation. With this transformation, a point is mapped from the real world to the image plane. Intrinsic and extrinsic parameters for the camera model are described in sec. 2.2.2. The representation of the camera model in homogeneous coordinates is explained in sec. 2.2.3. The section also covers computations for the considered transformation model. The section ends with the computation procedure for a two-view geometry, which is essential for stereo vision algorithms.

2.2.1. Basic Projective Geometry

This section introduces the main geometric ideas and notations that are required to understand the principle of two-view geometry. The geometric camera model (pinhole or projective camera) describes the process of projecting a real world point to a point in the image plane. For convenience, the virtual image is considered by placing the image plane in front of the camera. The mathematical notations and equations are equivalent to a real projective camera.

Fig. 2.4 illustrates the projective camera model. The pinhole itself is called the optical center. The virtual image is created on the image plane, which is displaced from the optical center along optical axis w. The intersection point of the optical axis and image plane is called the principal point (Prince, 2012).

The perspective projection is positioning a 3D point $\mathbf{w} = [u, v, w]^T$ in the image plane by establishing $\mathbf{x} = [x, y]^T$. For a normalized camera with focal length of one and the origin of

coordinate system (x, y) of the image plane being centered at the principal point, the projection of 3D point can be found using the relations:

$$x = \frac{u}{w} \tag{2.49a}$$
$$y = \frac{v}{w} \tag{2.49b}$$

where x, y, u, v and w are measured in the same units.

2.2.2. Intrinsic and Extrinsic Parameters

A real camera has a non unit focal length and the final position in the image is measured in pixels and not in the unit of physical distance. Therefore, the camera model must include these two effects into the mapping between points $\mathbf{w} = [u, v, w]^T$ and $\mathbf{x} = [x, y]^T$ with a constant scaling factors in both x- and y-directions (Ramalingam et al., 2011):

$$x = \frac{f_x \cdot u}{w} \tag{2.50a}$$
$$y = \frac{f_y \cdot v}{w} \tag{2.50b}$$

where f_x and f_y are the focal length parameters in x- and y- directions. Apart from accounting for the true focal length, the parameters f_x and f_y also include the photoreceptor space scaling.

In most imaging systems, the pixel position $\mathbf{x} = [0, 0]^T$ is at the top-left of the image rather than at the principal point. To cope with that, the camera model inhibits offset parameters c_x and c_y so that:

$$x = \frac{f_x \cdot u}{w} + c_x \tag{2.51a}$$
$$y = \frac{f_y \cdot v}{w} + c_y \tag{2.51b}$$

where c_x and c_y are the offsets in pixels from the top-left corner of the image to the positions where the optical axis strikes the image plane. The intrinsic or camera parameters $\{f_x, f_y, c_x, c_y\}$ describe the camera itself and can be written in a form of the so called camera matrix:

$$\Lambda = \begin{bmatrix} f_x & 0 & c_x \\ 0 & f_y & c_y \\ 0 & 0 & 1 \end{bmatrix} \tag{2.52}$$

Additionally, the projection model needs to adjust for the position and orientation of the camera,

as the camera is not always centered at the origin of the world coordinates with the optical axis aligned to the w-axis. Then the point in 3D space, which has to be transformed, can be defined in an arbitrary world coordinate system by rotation and translation transformation:

$$\begin{bmatrix} u' \\ v' \\ w' \end{bmatrix} = \begin{bmatrix} w_{11} & w_{12} & w_{13} \\ w_{21} & w_{22} & w_{23} \\ w_{31} & w_{32} & w_{33} \end{bmatrix} \begin{bmatrix} u \\ v \\ w \end{bmatrix} + \begin{bmatrix} \tau_x \\ \tau_y \\ \tau_z \end{bmatrix}, \tag{2.53}$$

or

$$\mathbf{w}' = \mathbf{\Omega}\mathbf{w} + \boldsymbol{\tau} \tag{2.54}$$

where $\mathbf{\Omega}$ and $\boldsymbol{\tau}$ are the rotation matrix and translation vector, respectively. The parameters $\{\mathbf{\Omega}, \boldsymbol{\tau}\}$ are the extrinsic parameters of the camera and define the position and orientation of the camera in the world.

The full pinhole camera model is described by combining equations (2.51) and (2.53). It implies the transformation of the point $\mathbf{w} = [u, v, w]^T$ in 3D space to the point $\mathbf{x} = [x, y]^T$ in the 2D image plane.

In practice, the pinhole camera model needs to be adjusted for the presence of lenses that collect light from a larger area and refocus it on the image plane. There are complex mathematical models that describe lens distortion. Radial distortion is a non-linear warping of the image that depends on the distance from the center of the image. It occurs when the field of view of the lens is large and results in the transformation of a straight line to a curved line.

Radial distortion is commonly modeled as a symmetric polynomial function of the distance from the image center. The final image position (x', y') is expressed as a function of the original position (x, y) (Hartley and Zisserman, 2003):

$$x' = x(1 + k_1 r^2 + k_2 r^4 + k_3 r^6) \tag{2.55a}$$
$$y' = y(1 + k_1 r^2 + k_2 r^4 + k_3 r^6) \tag{2.55b}$$

where r is the distance from the center of the image and the parameters k_1, k_2 and k_3 control the degree of distortion.

The second typical distortion is tangential distortion. It accounts for manufacturing defects. Therefore, the lens is not exactly parallel to the image plane (Bradski, 2008). It is characterized by the additional parameters p_1 and p_2:

$$x'' = x' + [2p_1 y' + p_2(r^2 + 2x'^2)] \tag{2.56a}$$
$$y'' = y' + [p_1(r^2 + 2y'^2) + 2p_2 x'] \tag{2.56b}$$

The distortion is implemented after a perspective projection and before the effect of the intrinsic parameters is corrected. Hence, the warping is relative to the optical axis and not to the origin of the pixel coordinate system.

Combining equations (2.53), (2.51), (2.55) and (2.56), one can estimate the 3D position of a point $\mathbf{w}$, given its projections $\{x_j\}_{j=1}^{J}$ in J number of cameras. With $J = 2$, the considered optimization problem is called calibrated stereo reconstruction, with $J > 2$ - multiple view reconstruction.

2.2.3. Transformation in Homogeneous Coordinates

The original mapping of a 3D world point described in Cartesian coordinate system to a 2D image point in Cartesian coordinates is nonlinear due to division by w in eq. (2.51). Therefore, the optimization problem of mapping the point from multiple projections into 3D world space requires a nonlinear optimization.

In order to make the projection equations become linear, it is convenient to represent the 2D image points and the 3D world points in homogeneous coordinates. The original Cartesian representation of the 2D image point $\mathbf{x}$ can be transformed into homogeneous coordinates using 3D vector $\widetilde{\mathbf{x}}$ such that (Szeliski, 2010):

$$\widetilde{\mathbf{x}} = \lambda \begin{bmatrix} x \\ y \\ 1 \end{bmatrix} \tag{2.57}$$

where λ is an arbitrary scaling parameter. With homogeneous coordinates, the point in projective n-dimensional space is expressed as a (n+1)-dimensional vector with the additional restriction, that any two points, whose values are proportional, are equivalent.

Additionally, it is possible to represent the point $\mathbf{w}$ in 3D space in homogeneous coordinates as a 4D vector $\widetilde{\mathbf{w}}$ such that:

$$\widetilde{\mathbf{w}} = \lambda \begin{bmatrix} u \\ v \\ w \\ 1 \end{bmatrix} \tag{2.58}$$

Converting between homogeneous and Cartesian coordinates in two dimensions involves either choosing $\lambda = 1$ and appending 1 to the original Cartesian coordinates, or dividing the first two entries of the homogeneous 3-vector by the third.

With temporal assumption that the world point $\mathbf{w} = [u, v, w]^T$ is in the same coordinate system as the camera, the camera model in homogeneous coordinates, i.e. the relation between $\mathbf{x}$ and $\mathbf{w}$,

is expressed as a set of linear equations:

$$\lambda \begin{bmatrix} x \\ y \\ 1 \end{bmatrix} = \begin{bmatrix} f_x & 0 & c_x & 0 \\ 0 & f_y & c_y & 0 \\ 0 & 0 & 1 & 0 \end{bmatrix} \begin{bmatrix} u \\ v \\ w \\ 1 \end{bmatrix} \tag{2.59}$$

To complete the pinhole camera model in homogeneous coordinates, the extrinsic parameters $\{\boldsymbol{\Omega}, \boldsymbol{\tau}\}$ that relate the world coordinate system and the camera coordinate system, are added in a matrix form:

$$\lambda \begin{bmatrix} x \\ y \\ 1 \end{bmatrix} = \begin{bmatrix} f_x & 0 & c_x & 0 \\ 0 & f_y & c_y & 0 \\ 0 & 0 & 1 & 0 \end{bmatrix} \begin{bmatrix} w_{11} & w_{12} & w_{13} & \tau_x \\ w_{21} & w_{22} & w_{23} & \tau_y \\ w_{31} & w_{32} & w_{33} & \tau_z \\ 0 & 0 & 0 & 1 \end{bmatrix} \begin{bmatrix} u \\ v \\ w \\ 1 \end{bmatrix} \tag{2.60}$$

As a camera sees the plane in the real world, it is of interest to simplify the transformation equations. It is considered that there is a direct mapping between points on the real world plane and points in the image.

The projective transformation model includes rotation, translation, scaling and shearing. Additionally, the lines are not considered to remain parallel after the projective transformation. Therefore, the relation between a point $\mathbf{w} = [u, v, 0]^T$ on a plane to the position $\mathbf{x} = [x, y]^T$ in the image is expressed as (Beutelspacher, 1998):

$$\begin{aligned} \lambda \begin{bmatrix} x \\ y \\ 1 \end{bmatrix} &= \begin{bmatrix} f_x & 0 & c_x \\ 0 & f_y & c_y \\ 0 & 0 & 1 \end{bmatrix} \begin{bmatrix} w_{11} & w_{12} & w_{13} & \tau_x \\ w_{21} & w_{22} & w_{23} & \tau_y \\ w_{31} & w_{32} & w_{33} & \tau_z \end{bmatrix} \begin{bmatrix} u \\ v \\ 0 \\ 1 \end{bmatrix} \\ &= \begin{bmatrix} f_x & 0 & c_x \\ 0 & f_y & c_y \\ 0 & 0 & 1 \end{bmatrix} \begin{bmatrix} w_{11} & w_{12} & \tau_x \\ w_{21} & w_{22} & \tau_y \\ w_{31} & w_{32} & \tau_z \end{bmatrix} \begin{bmatrix} u \\ v \\ 1 \end{bmatrix} \end{aligned} \tag{2.61}$$

Combining the two 3×3 matrices by multiplication, the resulting transformation is written in a general form of linear equations:

$$\lambda \begin{bmatrix} x \\ y \\ 1 \end{bmatrix} = \begin{bmatrix} h_{11} & h_{12} & h_{13} \\ h_{21} & h_{22} & h_{23} \\ h_{31} & h_{32} & h_{33} \end{bmatrix} \begin{bmatrix} u \\ v \\ 1 \end{bmatrix} \tag{2.62}$$

or in a matrix form:

$$\mathbf{x} = \mathbf{H}\mathbf{w} \tag{2.63}$$

Eq. (2.62) and eq. (2.63) describe a special case of a projective transformation, also called as collinearity or homography. A homography describes the mapping of the 2D coordinates of points on a plane in a real world to the position of the points in an image of that plane.

The homography matrix $\mathbf{H}$ has nine entries, although it contains eight degrees of freedom, as the entries are redundant with respect to scale. It can be seen in eq. (2.62), that the constant scaling of all nine values produces identical transformation, as the scaling is canceled by redefining the parameter λ:

$$\lambda = h_{31}u + h_{32}v + h_{33} \tag{2.64}$$

As plane-to-plane transformations are described by homographies, so are the transformations between multiple images of a real-world plane. Considering the case of two cameras, the transformation of the points on the plane in the real world to the points on the image of the first camera is given by 3×3 matrix $\mathbf{T}_1$ and similarly mapping to the second camera image is performed with matrix $\mathbf{T}_2$. Hence, the mapping from image 1 to image 2 can be written as:

$$\mathbf{T}_3 = \mathbf{T}_2\mathbf{T}_1^{-1} \tag{2.65}$$

2.2.4. Two-View Geometry

Many tasks of computer vision are based on the problem reconstructing a scene in a real world with certain number of cameras capturing the same scene. The optimisation problem for eq. (2.63) with two cameras is called stereo reconstruction problem. The estimation of the 3D position of a point in a world space based on its projection from two cameras is possible on condition of known intrinsic and extrinsic parameters of the cameras.

To find the intrinsic and extrinsic parameters, one needs to consider a geometrical relation between the images from the cameras as it depends on the intrinsic parameters of the cameras and their relative translation and rotation.

The case of two cameras viewing the same scene in the real world is presented in fig. 2.5. Considering the projection of the conceptual point **w** in the real world into the point $\mathbf{x}_{\text{left}}$ in the image plane of the left camera, the position of the point **w** along the ray from the optical center of the left camera is not defined. As the second camera is viewing the same point **w**, the projection of the point lies somewhere along the line in the image plane of the second camera. This line is called epipolar line.

As all the rays pass through the optical center of the camera, the epipolar lines must converge in a point in the second image plane. This point is known as the epipole.

To present the notation of two-view geometry in a mathematical form, one can assume that the center of the world coordinate system is at the optical center of the left camera, so the rotation matrix and the translation vector are $\{\mathbf{I}, \mathbf{0}\}$. The second camera may be in a general position $\{\boldsymbol{\Omega}, \boldsymbol{\tau}\}$. For simplicity, one can consider normalized cameras with $\boldsymbol{\Lambda}_1 = \boldsymbol{\Lambda}_2 = \mathbf{I}$. Then in

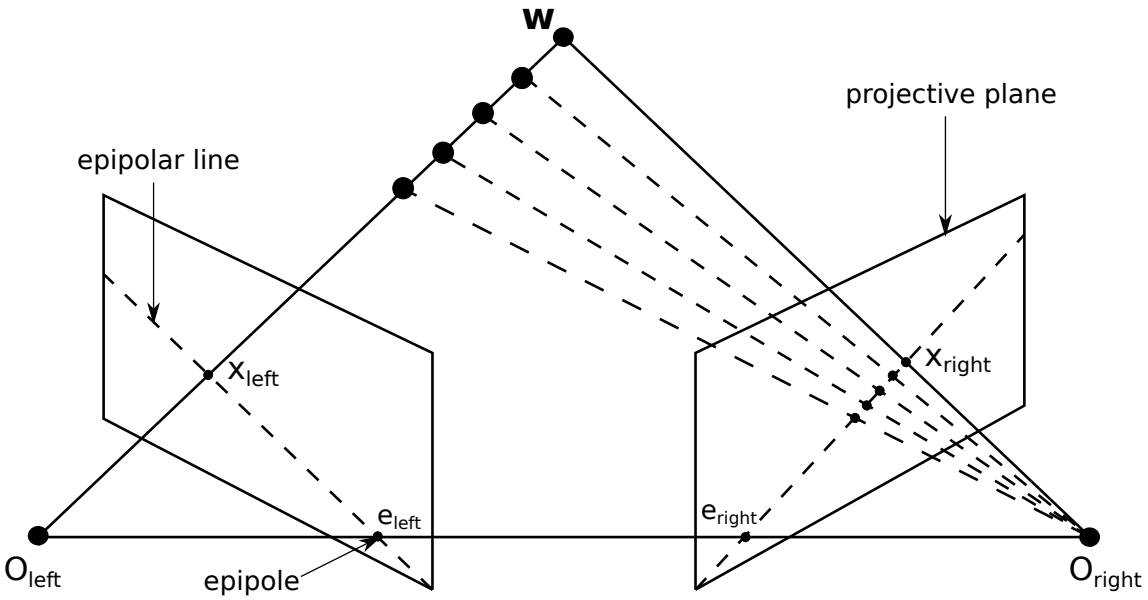

Figure 2.5.: The definition of epipolar line. Considering point $\mathbf{x}_{\mathrm{left}}$ in the first image, the projected 3D point **w** lies along the ray passing from the optical center $\mathbf{O}_{\mathrm{left}}$ of the left camera. The projection of the point **w** in the plane of the right camera should lie on the projected line. The projection of the ray is a line in the right projective plane, which is referred as epipolar line. In analogy, the same representation is valid for the left camera and point $\mathbf{x}_{\mathrm{right}}$.

homogeneous coordinates, a 3D point is projected into two image planes as:

$$\lambda_1 \widetilde{\mathbf{x}}_1 = [\mathbf{I}, \mathbf{0}] \widetilde{\mathbf{w}} \tag{2.66a}$$

$$\lambda_2 \widetilde{\mathbf{x}}_2 = [\boldsymbol{\Omega}, \boldsymbol{\tau}] \widetilde{\mathbf{w}} \tag{2.66b}$$

where $\widetilde{\mathbf{x}}_1$ and $\widetilde{\mathbf{x}}_2$ are the observed positions of the point $\mathbf{w}$ in the first and second camera, respectively.

Several mathematical operations with the set of the equations (2.66) lead to an explicit relation of the vectors $\widetilde{\mathbf{x}}_1$ and $\widetilde{\mathbf{x}}_2$ (Prince, 2012):

$$\widetilde{\mathbf{x}}_2^T \boldsymbol{\tau} \times \boldsymbol{\Omega} \widetilde{\mathbf{x}}_1 = 0 \tag{2.67}$$

Since the cross product operation $\boldsymbol{\tau}\times$ is expressed as multiplication by the 3×3 matrix $\boldsymbol{\tau}_\times$ defined as:

$$\boldsymbol{\tau}_\times = \begin{bmatrix} 0 & -\tau_z & \tau_y \\ \tau_z & 0 & -\tau_x \\ -\tau_y & \tau_x & 0 \end{bmatrix} \tag{2.68}$$

the eq. (2.67) has the form:

$$\widetilde{\mathbf{x}}_2^T \mathbf{E} \widetilde{\mathbf{x}}_1 = 0 \tag{2.69}$$

where $\mathbf{E} = \boldsymbol{\tau} \times \boldsymbol{\Omega}$ is knows as the essential matrix. The 3×3 essential matrix computes the geometric relation between two cameras.

With arbitrary intrinsic matrices $\boldsymbol{\Lambda}_1$ and $\boldsymbol{\Lambda}_2$ of two cameras, the general projection equations are:

$$\lambda_1 \widetilde{\mathbf{x}}_1 = \boldsymbol{\Lambda}_1 [\mathbf{I}, \mathbf{0}] \widetilde{\mathbf{w}} \tag{2.70a}$$

$$\lambda_2 \widetilde{\mathbf{x}}_2 = \boldsymbol{\Lambda}_2 [\boldsymbol{\Omega}, \boldsymbol{\tau}] \widetilde{\mathbf{w}} \tag{2.70b}$$

and the vectors $\widetilde{\mathbf{x}}_1$ and $\widetilde{\mathbf{x}}_2$ are related as:

$$\widetilde{\mathbf{x}}_2^T \mathbf{F} \widetilde{\mathbf{x}}_1 = 0 \tag{2.71}$$

with a definition of the fundamental matrix as:

$$\mathbf{E} = \boldsymbol{\Lambda}_2^T \mathbf{F} \boldsymbol{\Lambda}_1 \tag{2.72}$$

The fundamental matrix is further decomposed for an estimation of the rotation and translation between the cameras. From multiple images of known object, the intrinsic parameters of the cameras can be estimated. And with eq. (2.72), the rotation and translation between the cameras are found.

The pipeline procedure of the two-view reconstruction of static 3D scene based on two images taken from unknown position of the cameras can be explained chronologically with following steps (Prince, 2012):

Learn intrinsic parameters of the cameras

The estimation of intrinsic parameters of the camera is referred as camera calibration procedure. Viewing a special calibration target with sufficient number I of 3D points $\{\mathbf{w}_i\}$ on the surface and the corresponding projections in J images, the solution of eq. (2.63) is found with following approach:

- estimate J extrinsic matrices, which relate the object frame of the reference to the camera frame in each of J images
- estimate the intrinsic parameters by defining minor variations for the estimated extrinsic matrices.

A few iterations of this procedure yields the initial guess of the intrinsic parameters of the camera with sufficient number of the reference points and sufficient number of the taken images of the calibration target.

Learn extrinsic parameters of the cameras

Knowing the intrinsic parameters of the cameras and capturing the image of a real scene, to compute extrinsic parameters of the cameras one needs to perform following steps:

- compute the image features and find the initial matches of the features between two images
- compute the fundamental matrix using an eight-point algorithm for solving eq. (2.71) (Hartley and Zisserman, 2003)
- refine the matches knowing the epipolar geometry (if the match is not close to the induced epipolar line, it is rejected)
- estimate the essential matrix from the computed fundamental matrix by using eq. (2.72)
- decompose the essential matrix to a rotation matrix and a translation vector (Hartley and Zisserman, 2003).

Infer the 3D coordinates of a point in the plane relative to the cameras, given its image positions

Given J calibrated cameras in known positions (the cameras with known $\mathbf{\Lambda}, \mathbf{\Omega}, \boldsymbol{\tau}$), the coordinates of 3D point $\mathbf{w}$ in a real world can be estimated from the corresponding projections in the images $\{\mathbf{x}_i\}_j$ solving eq. (2.60) (Prince, 2012).

Rectification of the images

To cope with the computer vision tasks of depth estimation (also called as dense reconstruction), the preprocessing of the images known as rectification is needed. Dense stereo algorithms generally assume that the corresponding point in the image lies on the same horizontal scan line in the other image. Therefore, the goal of the rectification is to preprocess the images from two cameras so that each epipolar line is horizontal and the epipolar lines associated with a point fall on the same scan line to the point in the other image (Prince, 2012).

The rectification procedure is equivalent to a rearrangement of the cameras such that the motion from one to another is pure horizontal and both image planes are perpendicular to the w-axis (see fig. 2.4).

There is an entire family of homographies that, applied to the images, accomplish the goal of rectification (Liansheng, 2009; Loop and Zhang, 1999). It is performed by applying a series of transformations $\mathbf{\Phi} = \mathbf{T}_1\mathbf{T}_2\mathbf{T}_3$, which altogether move the epipole $\mathbf{e}$ to a position at infinity $[1,0,0]^T$.

At first, the coordinate system is centered at the principal point by a transformation with matrix $\mathbf{T}_1$:

$$\mathbf{T}_1 = \begin{bmatrix} 1 & 0 & -c_x \\ 0 & 1 & c_y \\ 0 & 0 & 1 \end{bmatrix} \tag{2.73}$$

Then the image is rotated about its center until the epipole lies on the x-axis:

$$\mathbf{T}_2 = \begin{bmatrix} cos[-\theta] & -sin[-\theta] & 0 \\ sin[-\theta] & cos[-\theta] & 0 \\ 0 & 0 & 1 \end{bmatrix} \tag{2.74}$$

where $\theta = arctan[e_y, e_x]$ is the angle of the translated epipole $e = [e_x, e_y]$. Finally, the epipole is translated to infinity by the transformation $\mathbf{T}_3$:

$$\mathbf{T}_3 = \begin{bmatrix} 1 & 0 & 0 \\ 0 & 1 & 0 \\ -1/e_x & 0 & 1 \end{bmatrix} \tag{2.75}$$

After these transformations, the epipole in the second image is at infinity in the horizontal direction. The epipolar lines in this image must converge at the epipole, and are consequently parallel and horizontal as desired. The rectification of the second image is analogous to $\mathbf{\Phi}$ transformation, but the details are emitted for simplicity reasons.

3. Visualization Technique

The chapter describes the details of two experimental techniques suitable for visualization of concentration fields in water. The first part of the chapter gives a short overview of basic principles of laser induced fluorescence (LIF) techniques used for visualisation of concentration fields of a trace gas in the water. The second part of the chapter covers a description of a novel LIF technique for boundary layer visualization that was used for the experiments performed in this work.

3.1. Laser Induced Fluorescence for Concentration Profiles

The LIF techniques are important for air-water gas exchange studies, since they allow the visualization of gas concentration fields near the water surface (Asher and Litchendorf, 2009; Herlina and Jirka, 2007; Walker and Peirson, 2008). Hence, the mechanisms driving the exchange processes can be investigated directly at the surface and different conceptual models (see sec. 2.1.4) can be tested. To perform the LIF method a fluorescent chemical compound (dye) is mixed to the water prior to an experiment. This chemical re-emits light upon laser excitation depending on the local concentration of the investigated gas. As a result of a reaction of the tracer with water molecules the pH value changes and, hence, modifies the fluorescent intensity. The florescent light is observed with a camera and from the local changes in the intensity the local concentration of the tracer is obtained.

The LIF technique is a non-invasive method for the visualization of concentration fields as it does not disturb the turbulent flow in the examined medium. The concentration of the fluorescent dye is kept sufficiently low to neglect the surface activity caused by the presence of the fluorophore.

This section describes the main concepts used for the realization of the technique. First, the basic principles of fluorescence with fundamentals of absorption and emission processes are discussed. Then the chemical components that were used in this study are described in detail as the right choice of chemicals is of importance for the technique. The last part covers the stepwise explanation of the measuring approach.

3.1.1. Basic Principles of Luminescence

A simple model describing the absorption and emission processes is a two or three level atomic system (Lakowicz, 2006). In the Jablonski diagram, showed in fig. 3.1 the singlet ground, first, and second electronic states are marked as S_0, S_1 and S_2, respectively.

Every allowed transition is marked with an arrow and can be described with the rate constant k_i. The transition rate k_i is a probability of the transition per unit time and can be defined by Fermi's

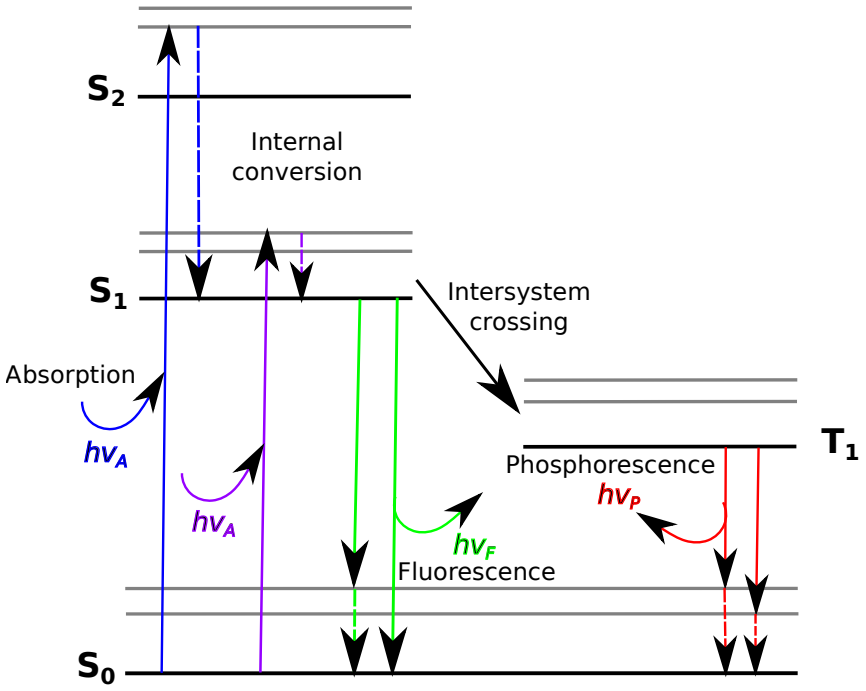

Figure 3.1.: Jablonski diagram for three level atomic system with possible transitions. S_0 is the ground state, S_1 and S_2 are the excited states and T_1 is the triplet state. The transition arrows indicate the transfer of the system in between the energy levels due to absorption, internal conversion, intersystem crossing and emission processes.

golden rule (Binney and Skinner, 2008):

$$k_{(i \to j)} = \frac{2\pi}{\hbar} |\langle f|H'|i\rangle|^2 \rho \tag{3.1}$$

where ρ is a number of final states per unit of energy and $\langle f|H'|i\rangle$ is the matrix element of the perturbation H' between the final and initial states. The relation of the transition rate and the life time τ_i of the considered state is written as:

$$k_i = 1/\tau_i \tag{3.2}$$

The absorption of photons with the energy $h\nu_A$ causes the transition of the fluorophore molecules from the ground state S_0 to some higher vibrational level of either S_1 or S_2 (blue and purple up arrows in fig. 3.1). Within less than 10^{-12} seconds (Lakowicz, 2006), the molecules are relaxed to the lowest vibration level of S_1 by internal conversion processes. Depending on the energy states of the quantum mechanical system, there are three options of further events:

Fluorescence

The transition of an excited molecule to the ground state occurs by emission of a photon. As fluorescence takes place typically in about 10^{-8} seconds, the process of internal conversion generally occurs before the fluorescence emission. Therefore, the emission of fluorescence originates from a thermally equilibrated excited state, which is at the lowest vibrational energy of S_1.

Due to energy dissipation by internal conversion from S_2 state or within S_1 state, the energy of

emitted photon is lower, and therefore yields longer wavelength than the excitation photon $h\nu_A$. The difference in energy or wavelength represented by ($h\nu_A$ – $h\nu_F$) is called the Stokes shift and causes the red-shift of the emission spectrum. This effect is essential for the sensitivity of the LIF technique. Having a large Stokes shift prevents the re-absorption of the emitted fluorescent light and ensures clear registration of the fluorescent light.

The most important criteria for the selection of a suitable fluorophore are the fluorescent lifetime and quantum yield. The fluorescent quantum yield of a fluorophore is a ratio of number of emitted photons to the number of absorbed photons (Lakowicz, 2006) and within the notation of rate constants defined as:

$$\Phi_f = \frac{k_r}{k_r + k_{nr}} \tag{3.3}$$

with the radiative rate constant k_r and non-radiative rate constant k_{nr}, that includes all possible non-radiative transitions such as internal conversion and intersystem crossing.

The fluorescent lifetime is an average time the excited fluorophore molecules spend in the singlet state S_1 before spontaneous emission of fluorescent light. The lifetime is given by:

$$\tau_f = 1/(k_r + k_{nr}) \tag{3.4}$$

The typical value of fluorescent lifetime is from 10^{-9} up to 10^{-7} seconds.

Phosphorescence

The fluorophore molecules in the state S_1 can also reach the triplet state T_1 by intersystem crossing with spin reversion (right part of fig. 3.1). The probability of intersystem crossing is higher when the vibrational levels of the states S_1 and T_1 overlap. In this case little or no energy is necessary for the transition. Phosphorescence as an emission from the state T_1 occurs due to the transition to the vibrational levels of the ground state (as a transition to the singlet ground state is forbidden).

Quenching

The alternative mechanism for the excited fluorophore molecules to reach the ground state S_0 is a non-radiative decay. It may take place by intermolecular energy transfer to a different molecule. This process of energy transfer via collision or resonance transfer is termed quenching or sensitization.

Described relaxation mechanisms of excited fluorophore molecules present the core of LIF techniques. In the current study the relaxation process in the form of fluorescence was used. The application of LIF technique based on quenching effect with oxygen as a trace gas is described in Friedl (2013). The performance of the LIF technique controlled by fluorescent pH sensitive indicators is shown in Herzog (2010).

3.1.2. Fluorescent Dye

The basic idea of the measuring technique used in the current study is based on a change in intensity of the emitted fluorescent light due to the presence of a trace gas.

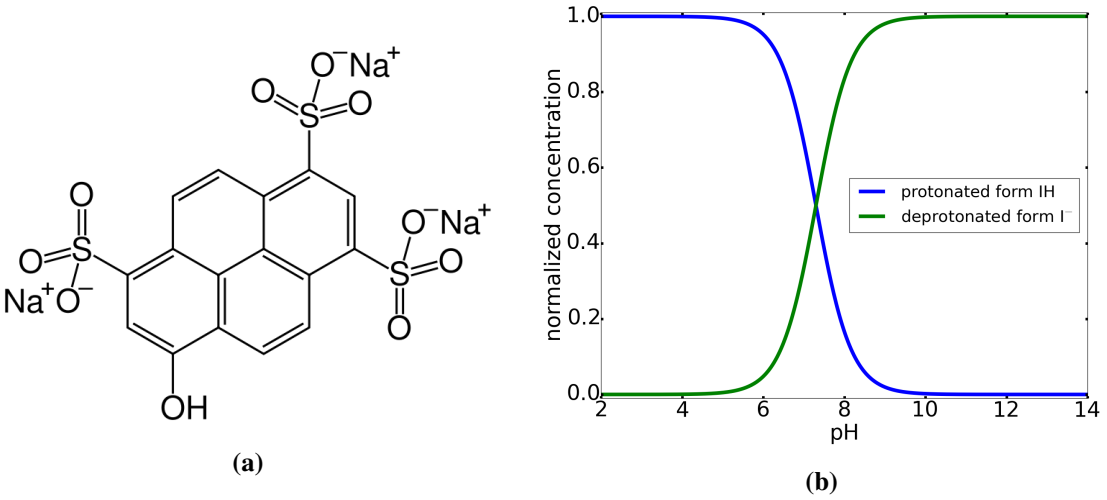

(a) **(b)**

Figure 3.2.: Characteristics of Pyranine: (a) Molecular structure of Pyranine with Na^+ and OH bindings presenting Pyranine as a fourfold charged anion. The picture is taken from Tran-Thi et al. (2000). (b) Concentration of protonated and deprotonated components of Pyranine in dependence on pH value, i.e. $-\log_{10}(H_3O^+)$, normalized to the total concentration of Pyranine. The buffer point of equal concentrations of both components is at pH = 7.3.

The selection of the appropriate fluorescent dye should fulfil the number of requirements that were listed in Crimaldi (2008):

- the absorption wavelength of the dye must be suitable for available laser excitation wavelengths
- the fluorescent dye needs to provide high quantum yield to maximize the fluorescent signal
- a large Stokes shift is desired to reduce the probability of re-absorption
- the dye needs to be soluble in water
- the insensibility to photobleaching processes and temperature changes is preferable
- the surface activity in water should be low to avoid an influence on a gas transfer

Other reasons not related to the LIF technique are that the fluorescent dye is suppose to be non or low toxic to simplify the process of water disposal and to be relatively cheap to provide multiple measurements with the desired concentrations of the fluorescent dye.

For the current study the fluorescent indicator 8-hydroxypyrene-1,3,6- trisulfonic acid trisodium salt $C_{16}H_7Na_3O_{10}S_3$ (abbreviated as HPTS and also called Pyranine) was selected as fluorescent dye. The molecular structure of Pyranine is presented in fig. 3.2a. The molecular mass of Pyranine is 523.4 g/mol.

Pyranine was used in previous studies to measure concentration profiles. The most similar work was conducted by Herzog (2010) by performing measurements of the concentration profiles of hydrogen chloride gas with Pyranine as fluorescent pH indicator.

Dissociation in water

Dissolved in water, Pyranine is present in two forms - protonated and deprotonated forms - according to the following reaction:

$$\mathrm{IH} + \mathrm{H_2O} \leftrightarrow \mathrm{I^-} + \mathrm{H_3O^+} \tag{3.5}$$

where $\mathrm{I^-}$ is the deprotonated form of the fluorophore or the base component, while IH is the protonated form or the acid component. The deprotonation reaction occurs from left to right, while protonation reaction from right to left. The time constant of the protonation reaction of Pyranine is 5.6 ns. Therefore, the protonation reaction is happening much faster than the transport process of a tracer gas through the boundary layer (according to Jähne (2009), the transport of a tracer gas through the boundary layer takes approximately 0.04-4 seconds).

The dissociation constant of eq. (3.5) defines the individual concentrations of the components depending on the hydrogen concentration as:

$$\mathrm{K_a} = \frac{[\mathrm{I^-}][\mathrm{H_3O^+}]}{[\mathrm{IH}]} \tag{3.6}$$

Further the logarithmic measure of the acid dissociation constant pK_a is used instead of K_a as the constant K_a covers many orders of magnitude. Constant pK_a is defined as:

$$\mathrm{pK_a} = -\log_{10}\mathrm{K_a} \tag{3.7}$$

Depending on the concentration of additional ions in the solvent, the dissociation constant for Pyranine varies from 7.3 to 8.04. The measurement of the pK_a constant at different concentrations and various buffer solutions were performed by Avnir and Barenholz (2005, 2006); Barnadas-Rodríguez and Estelrich (2009); Tran-Thi et al. (2000). The value of 7.3 from Avnir and Barenholz (2005) was used for the simulations conducted in sec. 4.1.

Absorption characteristics

The studies on the extinction coefficient of Pyranine were performed by Wolfbeis et al. (1983) and Prayer (1997). It was established that the total extinction coefficient of Pyranine is linearly dependent on the concentration of the components (either base or acid component) and non-linearly dependent on the pH value, i.e. the concentration of $\mathrm{H^+}$.

The absorption maxima of the protonated and deprotonated forms of Pyranine are at 403 nm and 454 nm (O'Neil, 2006). According to the measurements performed in this work, the maxima for the corresponding forms lie at 403.4 nm and 454.2 nm (fig. 3.3a). The difference of 51 nm in the maxima of the absorption curves of the Pyranine components allow an excitation mode of each component individually.

The absorption peaks are at 455 nm for high pH values. At this wavelength Pyranine in alkaline solutions emits more light than in acid solutions, since only the deprotonated form $\mathrm{I^-}$ is excited. Additionally, these settings are desired for the experiments as the wavelength region around 455 nm is suitable for available blue light diode lasers.

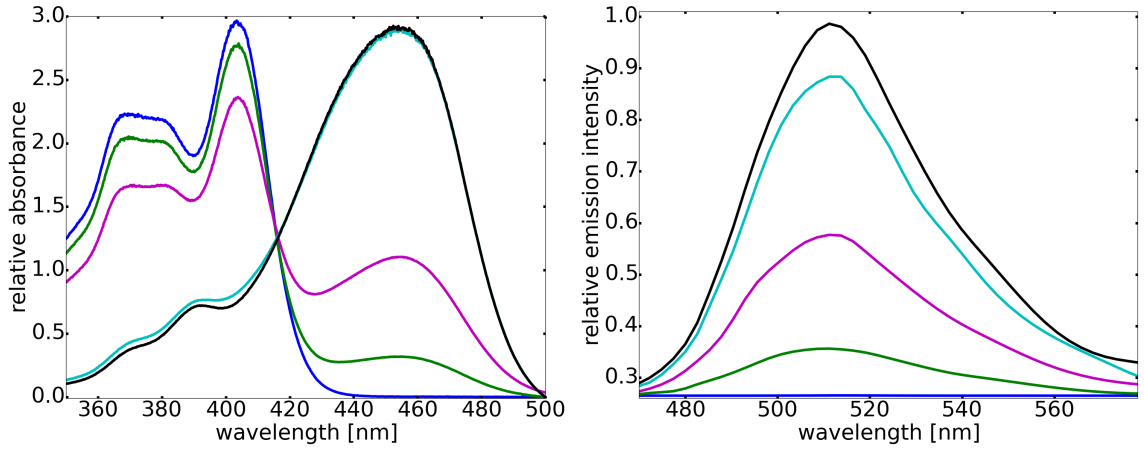

(a) **(b)**

Figure 3.3.: (a) Absorption spectra of Pyranine measuread at different pH values of the solvent: pH = 4 (blue line), pH = 6.5 (green line), pH = 7 (purple line), pH = 9 (light blue line) and pH = 11 (black line). (b) Emission spectra of Pyranine measured at an excitation wavelength of 455 nm for the identical pH values as in (a). The emission plot is taken from (Wolfbeis et al., 1983).

The isosbestic wavelength, at which both base and acid components of Pyranine have the same absorption independent on pH value, is found at 415.6 nm Wolfbeis et al. (1983). This wavelength can be used to calculate the total concentration of Pyranine as the light is equally absorbed by both components.

Fluorescent characteristics

The fluorescent dye Pyranine belongs to the group of fluorophores that are an exceptions of the mirror-image rule stating that emission spectra are typically independent of the excitation wavelength.

The emission spectrum of Pyranine (fig. 3.3b) shows none of the vibrational structure seen in the absorption spectrum (fig. 3.3a). The reason for observed difference in the spectra is due to ionization of the hydroxyl group. For the molecules in the excited state the dissociation constant pK_a decreases, shifting the system to the mode with the dominant deprotonated form of Pyranine. Therefore, the emission mostly occurs from the base component I^- that has a broad emission spectrum.

In this way, the emission spectrum is a mirror image of the absorption of the deprotonated Pyranine form at high pH values. Yet the components of Pyranine may be excited with the diverse wavelengths, the emission spectra of both components are identical.

According to Avnir and Barenholz (2005), with an excitation wavelength of 455 nm the maxima of the emission spectrum is at 511 nm as shown in fig. 3.3b. Observed maxima for absorption and emission spectra of Pyranine result in a large Stokes shift of 56 nm. As it was mentioned before, a large Stokes shift is desirable to prevent the re-absorption of emitted light.

Quantum yield

According to Wolfbeis et al. (1983), Pyranine provides a high quantum efficiency with a quantum yield being nearly one. This implies that nearly all absorbed light is emitted as fluorescence

and almost nothing is transferred to the other forms of energy.

pH sensibility

As it was already seen in fig. 3.3a, the absorption and emission spectra of Pyranine are pH sensitive. Due to essential difference in emission spectra in dependence of pH value, Pyranine is also referred to as pH indicator. This feature is of a great importance for the visualization technique that was used in the experiments. Due to the high pH sensibility around the pKa value (approx. 7), Pyranine is an appropriate dye for the novel boundary layer visualization (BLV) technique. This is explained in more detail in sec. 3.2.

Many studies were performed comparing different fluorescent pH indicators on their sensibility to temperature changes, photo bleaching and quenching. A broad study by Wolfbeis et al. (1983) selected Pyranine as the most appropriate fluorescent pH indicator to measure the differences of local pH values in the aqueous state.

3.1.3. Trace Gas

For the LIF experiments it is also important to select the right tracer. The gas must be soluble to dissolve in water. Additionally, the gas needs to react with the water molecules to change the pH, which can then be measured by the pH indicator.

In the current study ammonia NH_3 was selected as a trace gas. The molar mass of ammonia is 17.031 g/mol. At normal conditions with a temperature of 25 °C and a pressure of 1 kPa, the densities of ammonia in liquid and gaseous phases are 0.60285 g/cm^3 and $7.7882{\cdot}10^{-3}$ g/cm^3, respectively. Ammonia has a high critical temperature around 132 °C. A 25% solution of ammonia was used during the experiments. By using a bubble flask, ammonia is always in equilibrium between air and water and is flushed into the air space of the facility.

Dissociation in water

In aqueous solutions, ammonia acts as a base, acquiring hydrogen ions from H_2O to produce ammonium and hydroxide ions. Therefore, ammonia exists in aqueous solution either as ammonium ions or ammonia itself, according to the following equilibrium reaction:

$$\mathrm{NH_{3(aq)}} + \mathrm{H_2O} \leftrightarrow \mathrm{NH_4^+} + \mathrm{OH^-} \tag{3.8}$$

As not all of the dissolved ammonia reacts with water to form ammonium ions, a substantial fraction remains in the molecular form. Therefore, ammonia is considered as a weak base. A quantitative indicator of the strength of eq. (3.8) is given by the ionization constant:

$$pK_b = -log_{10}K_b = -log_{10}\left(\frac{[\mathrm{NH_4^+}][\mathrm{OH^-}]}{[\mathrm{NH_3}]}\right) \tag{3.9}$$

At the room temperature of 25 °C the value of the dissociation constant pK_b of ammonia is 4.75. Therefore, the ammonium ions are largely predominant at neutral or slightly basic pH values of the solvent. According to Hales and Drewes (1979), the base dissociation constant of ammonia is

temperature dependent and the relation is expressed by the following equation:

$$log_{10}K_a = -0.09018 - \frac{2729.92}{T} \tag{3.10}$$

Solubility

A high solubility of ammonia is required in order to achieve relatively high concentrations of ammonia in the aqueous solution. For ammonia the high solubility can be explained by the polarity of NH_3 molecules and their ability to form hydrogen bonds. With the hydrogen bonds between water molecules being broken, they can be replaced by equivalent bonds between water and ammonia molecules.

The physical solubility α defines the ratio of surface concentrations of NH_3 of a gaseous and aqueous phases:

$$\mathrm{NH_3|_g} \overset{\alpha}{\rightleftharpoons} \mathrm{NH_3|_{aq}} \tag{3.11}$$

The values for physical solubilities of ammonia reported in the literature diverge strongly from α = 812 up to α = 2256 (Clegg and Brimblecombe, 1989; Dasgupta and Dong, 1986; Hales and Drewes, 1979; Holzwarth et al., 1984; Sander, 2014; Shi et al., 1999). Large variations in the measured solubility constants can be explained by different conditions during the experiments performed in the different works. Holzwarth et al. (1984) and Hales and Drewes (1979) reported diverse values of physical solubility of ammonia for different absolute concentrations of ammonia. Other diversities might be related to the temperature dependence. According to Hales and Drewes (1979), the relation of the physical solubility to the temperature is:

$$log_{10}\alpha = -1.69 + \frac{1477.7}{T} \tag{3.12}$$

Additionally, the diversity might be due to the different pH values at which the solubility was measured. At lower pH value the effective solubility changes due to the reaction (3.9). The effective solubility is defined as:

$$\alpha_{\mathrm{eff}} = \alpha(1 + 10^{-\mathrm{pH}+\mathrm{pK_a}}) \tag{3.13}$$

For further estimations, the physical solubility of ammonia was considered to be 1713 as reported by Dasgupta and Dong (1986), where the aqueous solubility of ammonia was studied by the use of microporous membrane tubes. The solubility was calculated under relatively low concentrations of ammonia from 0.002 to 0.1 M at alkaline solutions with pH value from 6 to 10. Those conditions were close to the conditions of the LIF measurements performed in the study.

Ammonia as a high soluble gas has nearly no resistance in the water-sided mass boundary layer and therefore is an air-side controlled gas.

Diffusion coefficients

The diffusion constants of ammonia for aqueous and gaseous phases are $1.72{\cdot}10^{-5}\,\mathrm{cm^2/s}$ and $0.23\,\mathrm{cm^2/s}$, respectively (Yaws, 1999). Additionally, the diffusion of the ammonium and hydro-

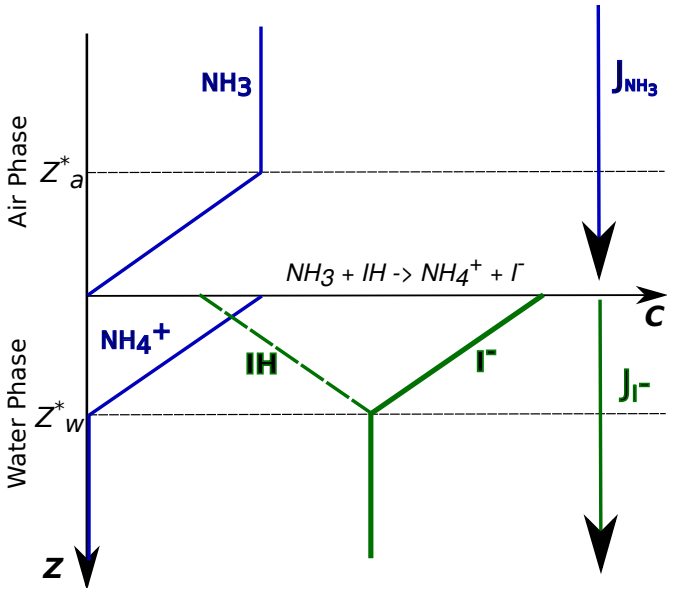

Figure 3.4.: Simplified sketch of NH_3 invasion into the water: Coresponding concentrations of dissociated ions and Pyranine components are presented. The profiles are assumed to satisfy the film model (sec. 2.1.4). The horizontal dashed lines represent the mass boundary layer in the air and water side. The flux of the ammonia in the air side is replaced by the flux of the I^- component in the water side.

gen ions suppose to be taken into account. With the diffusivity of hydrogen ion and ammonium ion being $5.28{\cdot}10^{-5}\,\mathrm{cm}^2/\mathrm{s}$ and $1.96{\cdot}10^{-5}\,\mathrm{cm}^2/\mathrm{s}$, respectively, the coupled diffusion coefficient is $2.9{\cdot}10^{-5}\,\mathrm{cm}^2/\mathrm{s}$.

3.1.4. Measuring Approach

The main concept of the LIF technique is to visualize the change of the concentration of the trace gas dissolved in water. It can be performed by replacing the flux of the trace gas with the flux of the indicator form which concentrations can be easily measured (the concept was first proposed by Hiby (1983)). In the current case the flux of ammonia is replaced by the flux of the fluorescent dye Pyranine.

To understand the transport of ammonia through the air-water interface, the case of invasion experiment is considered. By adding ammonia into the air side of the facility, the ammonia molecules diffuse towards the water surface. The sketch of considered fluxes in the air and water side is shown in fig. 3.4. For simplicity the concentration profiles in the air and water phases are assumed to comply with the film model (sec. 2.1.4). As the difference in the thickness of the boundary layers at the water and air phases are not of interest here, they are marked at the same distance from the water surface.

Considering the case of initial pH value close to the buffer point of Pyranine (approximately 7) and the value of Pyranine concentration of $10^{-5}\,\mathrm{mol/L}$, the concentration of hydrogen ions OH^- and H_3O^+ in the water are two orders of magnitude smaller than the concentration of Pyranine components IH and I^-, therefore the $[OH^-]$ and $[H_3O^+]$ can be neglected. With this assumption, the absorbed NH_3 almost instantaneously undergoes the chemical reaction that takes place at the

water surface:

$$NH_3 + IH \rightarrow NH_4^+ + I^- \tag{3.14}$$

As all NH_3 is assumed at the water surface, the concentration of NH_3 at the surface comes to zero. The flux j of NH_3 in the air is given by the transfer velocity in the air and the bulk concentration of NH_3 in the air side, i.e:

$$\mathrm{j} = \mathrm{k_a}[NH_3]_a|_{\mathrm{bulk}} \tag{3.15}$$

Due to conservation of the mass, the flux of NH_3 in the air side is equal to the flux of produced by the reaction (3.14) NH_4^+ ions. As the reaction includes the formation of I^- as well as NH_4^+, the component of I^- is being transported through the aqueous boundary layer in the same way as ammonium. Therefore, the flux in the water side is expressed as:

$$\mathrm{j} = -\mathrm{k_w}([I^-]_w|_{\mathrm{bulk}} - [I^-]_w|_{\mathrm{surface}}) \tag{3.16}$$

Due to equality of eq. (3.15) to eq. (3.16), the flux of ammonia in the air is replaced by the flux of I^- molecules of Pyranine in the water side.

Exciting Pyranine molecules with a laser illumination, I^- molecules emit light that can be captured. The more ammonia is penetrated through the water surface, the more I^- molecules are produced and the higher brightness of emitted light is observed. Therefore, the concentrations of ammonium NH_4^+ ions can be derived from the fluorescent intensities as it is directly proportional to the concentration of I^- ions.

The tracer concentrations and initial conditions in this case are needed to fulfil the buffer point condition. As at the buffer point the change in the concentration of fluorescent base component of Pyranine, hence, the change in intensities, is linear dependent on the change of ammonia concentration. For this reason, it is of interest to keep the water as a neutral solution to ensure the equal concentrations of both components of the fluorescent dye (with the value for the dissociation constant of fluorescent dye being close to 7). The experiments of described LIF technique with Pyranine as a fluorescent dye and hydrogen chloride as a trace gas were performed by Herzog (2010).

3.2. Laser Induced Fluorescence for Boundary Layer Visualization

This section covers the details of the boundary layer visualization (BLV) technique that was used in the experiments. The descriptions of the main objective of the modification purpose, essential requirements for its realization and the induced measuring scheme are presented.

3.2.1. Main Objective

Apart from the advantages of LIF techniques mentioned in sec. 3.1, the techniques are difficult to apply for the visualization of air-water gas transfer across the mass boundary layer at a free water surface. Because of the necessity of a high spatial and temporal resolution in order to resolve the mass boundary layer and fast turbulent processes, the visualization of concentration fields are mostly limited to the visualization in two dimensions which does not yield the full understanding of the mechanisms of a gas exchange.

The scope of this work was devoted to simplification of the concentration fields of observed molecules, i.e. the base component I^- of fluorescent dye Pyranine. This is achieved by demanding the vertical concentration profiles to have a steep decay at the certain depth, benefiting in a step-shape brightness profiles. Gained in such a way concentration fields can be considered binary as they carry constant value of fluorescent intensity close to the surface and no fluorescence in the bulk. The binary concentration fields of I^- allow to feature time sequences of three dimensional concentration fields using multi view geometry methods.

The first steps towards the BLV technique were proposed by Hiby (1968). Jähne et al. (1985) modified the technique of Hiby (1968) to make it applicable at large wind-wave facilities. The first application of the technique used with identical chemical system is presented in Kräuter et al. (2014).

3.2.2. Requirements

In order to accomplish the desired sharp drop of the fluorescent profile, ammonia must effect the emission characteristics of the fluorescent component. As it is shown in fig. 3.3b, the emission intensity has a strong dependence on the pH value of the solvent. Therefore, ammonia has to change the ratio of the hydrogen ions. This is achieved by providing an acidic solution at the start of ammonia invasion. For this condition in contrast to eq. (3.8), ammonia would act as a strong acid according to the reaction:

$$\mathrm{NH_{3(aq)} + H_3O^+ \leftrightarrow NH_4^+ + H_2O} \tag{3.17}$$

with the acid dissociation constant defined as:

$$\mathrm{pK_a = -log_{10}K_a = -log_{10}\left(\frac{[NH_3][H_3O^+]}{[NH_4^+]}\right)} \tag{3.18}$$

According to Clegg and Brimblecombe (1989), the dissociation constant pK_a of ammonia is 9.25. Since the water is acid at the beginning of a measurement, ammonia dissolved in water is instantaneously reacting with the H_3O^+ ions to ammonium NH_4^+ ions. Depending on the flux of ammonia to the water, the change in pH value is either small or significant enough for effecting the emission of the base component of Pyranine. The desired case is achieved with relatively high fluxes of ammonia. If the pH value gets closer to the pK_a value of the reaction (3.18), more ammonia is dissolved in water without reacting to ammonium. Additionally, eq. (3.8) leads to an

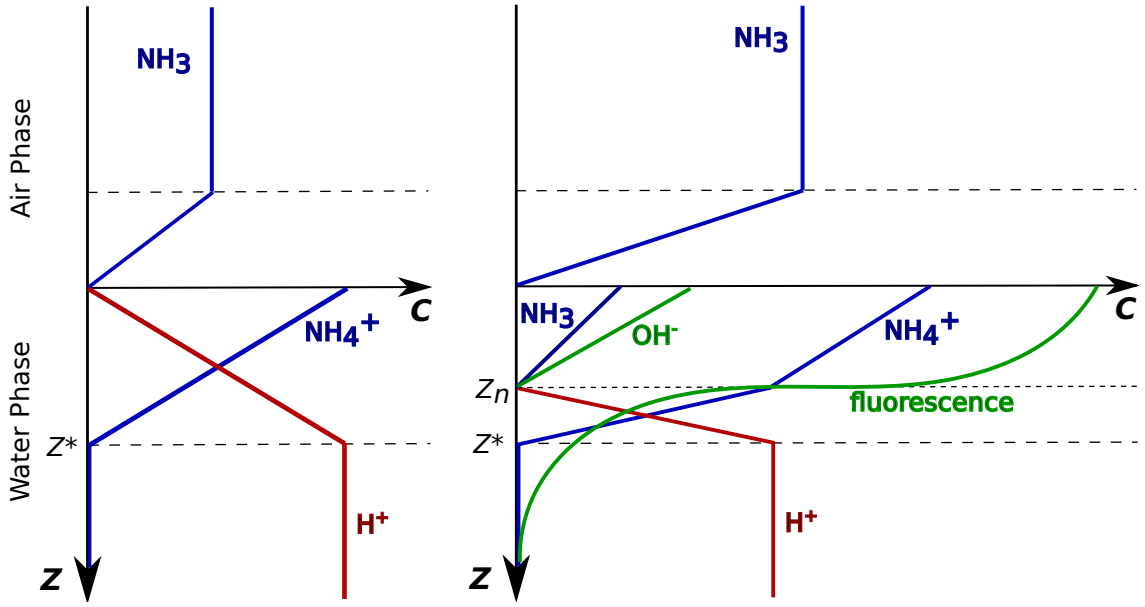

Figure 3.5.: The sketch of NH_3 invasion into the acid water: The left side shows the case of low concentration of NH_3 in the air side. The incoming ammonium molecules are consuming H^+ ions with increasing the pH from the bulk value of 4 to the value of 7 at the water surface. The flux of H^+ ions is the opposite to the flux of dissolved ions of ammonium NH_4^+. The right side shows the case with relatively high ammonia concentration. With spare ammonia molecules, OH^- hydrogen ions are produced ensuring sufficient increase of pH from 7 to large values. The depth of neutral condition is shifted downwards. The region with pH value greater than 7 is considered to be fluorescent.

increase of OH^- ions in the water and the pH value increases further. Hence, the surface pH value changes from acid to alkaline and this leads to an increase in fluorescent intensity.

3.2.3. Measuring Approach

A sketch of the ammonia concentration profiles with the extreme case of a low pH value at the start of the invasion process is shown in fig. 3.5. The concentration profiles are assumed to comply with the film model (sec. 2.1.4). The jump of the ammonia concentration at the water surface is declared by the solubility of ammonia being larger than one (the value of 1713 was considered according to Dasgupta and Dong (1986)). The boundary layer thickness in the water side is larger than the thickness of the mass boundary layer in the air side. This was reported by Jähne (1991) and Jähne and Haußecker (1998). In fig. 3.5 the sizes of the boundary layer in the air and water side do not hold the correct scales for illustrative reasons.

To be able to neglect the dye concentration during the measurements, low concentrations are used, which are at least two orders of magnitude smaller than the concentration of the hydrogen ions. By choosing a pH value of 4 at the start of each measurement the concentration of Pyranine is at least smaller than 10^{-6} mol/l. Therefore, the concentrations of the species I^-, IH and OH^- can be neglected.

To achieve a step shaped intensity profile, two cases have to be described in more detail. On the left side of fig. 3.5 the first case of a low ammonia concentration in the air and, hence, a low flux from air to water is shown. At this condition, the change in the concentration of the hydrogen

ions occurs within the boundary layer, marked as a dashed line in the water side. The flux of the hydrogen ions is opposite but equal to the flux of ammonium ions NH_4^+. At the shown condition in fig. 3.5 (left) the pH value at the surface is increasing from a value of 4 in the bulk to a value of 7 at the water surface. Since Pyranine starts to emit fluorescent light at higher pH values, if excited in the blue wavelength range, at the shown condition no light is observed.

The second case is shown in the right side of fig. 3.5. The concentration of ammonia in the air is higher than in the first case and, hence, a higher flux of ammonia to the water is achieved. At this condition all hydrogen ions are consumed by the reaction (3.8) and ammonia is dissolved in water by eq. (3.17). Therefore, the neutral depth (pH = 7) is shifting down towards the bulk of the water. Depending on the concentration of ammonia the neutral depth is located at a certain depth, which is a fraction of the mass boundary layer or with sufficient ammonia is at the depth of boundary layer thickness. The area above the neutral depth is fluorescent as its pH value is larger than 7.

The sharp step-shaped drop of the intensity is enabled by the logarithmic definition of the pH value on the H^+ concentration. Therefore, the linear increase of the hydrogen concentration leads to a logarithmic increase of the pH value. Since the hydrogen concentration at a pH value of 7 is close to zero even small changes in the hydrogen concentration lead to a large increase of the pH value. Therefore, a sharp change in the fluorescence of Pyranine is ensured and the intensity can be approximated as a binary field.

It is worth mentioning that the profiles presented in fig. 3.5 show mean profiles of the concentration distribution according to film model (sec. 2.1.4). As it will be shown in sec. 4.3, the shape of single profiles changes in time due to dynamic conditions during the experiment. This enables the investigation of such turbulent processes as detachments of the fluorescent layer from the water surface and its propagation to the bulk. On the other hand, it is possible to compare the mean concentration profiles with the profiles of corresponding models discussed in sec. 4.3.4 and to check at which conditions the boundary conditions change from a free to a rigid interfaces.

4. Verification of Visualization Technique and Profile Measurements

This chapter includes two methods to verify the experimental technique described in sec. 3.2. The first part of this chapter is focused on simulations of mean concentration profiles predicted by the gas exchange models described in sec. 2.1.4. The second part of the chapter describes experiments at a linear wind-wave facility for measuring one dimensional profiles with the usage of the novel LIF technique for boundary layer visualization (see sec. 3.2). A description of the wind-wave tunnel, the experimental set-up, calibration procedure, the experiments itself and the data processing steps are described. The last section of the chapter presents the comparison of simulated concentration profiles for different gas exchange models with experimental one dimensional profiles.

4.1. Simulations

The section presents main concepts and assumptions necessary for calculating mean concentration profiles conforming to the boundary layer visualization (BLV) technique. The prescribed mean concentration profiles from the gas exchange models are considered as an input. As a result, the fluorescent intensity profile is computed within a certain model by solving a non-linear system of equations. The section also includes the results of simulation in the presence of carbon-dioxide.

4.1.1. Main Assumptions

To verify the capability of the visualization technique formulated in sec. 3.2, the mean concentration profiles of the fluorescent component I^- of Pyranine need to be calculated. In order to estimate a distribution of concentration of the fluorescent base component I^- over depth, one needs to consider charge conservation principle for all ions present in water. As it was mentioned in sec. 3.2, at the start of a tracer gas invasion the water must be acid. For that purpose hydrogen chloride solution was added to the water resulting in presence of Cl^- ions in addition to hydrogen ions. Being mixed in water Pyranine contributes with deprotonated form as I^- ions. With ammonia penetrating through the air-water interface and inducing presence of the ammonium ions NH_4^+, the conservation law for the chemical species of the considered system is written as:

$$[H^+] + [NH_4{}^+] = [I^-] + [OH^-] + [Cl^-] \tag{4.1}$$

In addition to eq. (4.1), the dissociation reactions of Pyranine and ammonia with known acid dissociation coefficients pK_a^{IH} and $pK_a^{NH_3}$ for the dissociation process in the water need to be

included:

$$\mathrm{K_a^{IH}} = \frac{[\mathrm{I^-}][\mathrm{H_3O^+}]}{[\mathrm{IH}]} \tag{4.2}$$

$$\mathrm{K_a^{NH_3}} = \frac{[\mathrm{NH_3}][\mathrm{H_3O^+}]}{[\mathrm{NH_4^+}]} \tag{4.3}$$

The total concentration of Pyranine is fixed and presented as the sum of protonated and deprotonated forms:

$$[\mathrm{IH}]_{\mathrm{tot}} = [\mathrm{IH}] + [\mathrm{I^-}] \tag{4.4}$$

According to eq. (3.8), dissolved in water ammonia exists in two forms. Therefore, the total concentration of ammonia is defined as a sum of ammonia molecules in aqueous solution and ammonium ions:

$$[\mathrm{NH_3}]_{\mathrm{tot}} = [\mathrm{NH_3}]_{\mathrm{aq}} + [\mathrm{NH_4^+}] \tag{4.5}$$

Due to the nonlinearity of the set of eq. (4.1), eq. (4.2), eq. (4.3), eq. (4.4) and eq. (4.5) the solution i.e. the function of $[\mathrm{I^-}]$ in dependence on $[\mathrm{NH_3}]_{\mathrm{tot}}$ does not have an explicit form. Therefore, the set of equations was solved numerically for a number of certain fixed values for $[\mathrm{IH}]_{\mathrm{tot}}$ and [HCl] (using built-in *fsolve* function of *SciPy.optimize* package in *iPython*). The solution gives the corresponding set of concentrations of all components in the water. With a certain number of fixed parameters ($[\mathrm{IH}]_{\mathrm{tot}}$ and [HCl]), a defined relation between $[\mathrm{NH_3}]_{\mathrm{tot}}$ and $[\mathrm{I^-}]$ is found:

$$[\mathrm{I^-}] = P([\mathrm{NH_3}]_{\mathrm{tot}}) \tag{4.6}$$

The function P used further for calculating fluorescent intensity profiles. Examples of functions P, pH value and fluorescent component dependencies are presented in fig. 4.1.

In a first set of simulations, the effect of different concentrations of $\mathrm{IH_{tot}}$ and HCl on the fluorescence distribution was studied. As the goal of these simulations was to estimate the concentration of chemical components maintaining step-shaped brightness profiles, the simulations were performed at diverse conditions. As it is suggested in sec. 3.2, the increase in penetrating through the water surface ammonia changes the pH value. The dependency of pH value on $[\mathrm{NH_3}]_{\mathrm{tot}}$ was calculated for different Pyranine concentrations (fig. 4.1a). The initial pH value was kept equal to 4 due to fixing the HCl concentration to 10^{-4} mol/L. With a change of $\mathrm{IH_{tot}}$ concentration from 10^{-6} up to 10^{-3} mol/L, the change of pH value appears to be sharper at lower concentrations of $\mathrm{IH_{tot}}$. This can be explained by the influence of the buffer point of Pyranine, as the ratio of Pyranine forms is pH dependent (see fig. 3.2b). As the initial pH value was fixed to 4 for all conditions, the start of the change in pH value arises at the same $\mathrm{NH_3}$ concentration (the concentration needed to consume all $\mathrm{H_3O^+}$ ions according to eq. (3.17)). With the change of pH value, the chemical equilibrium of the $\mathrm{I^-}$ and IH Pyranine components is shifted. Fig. 4.1b shows the ratio of the fluorescent deprotonated form of Pyranine to the total amount of Pyranine in the water in dependence on the total ammonia concentration. As the change of pH value appear from 4 to 10, Pyranine undergoes the transformation from the case of dominant protonated form IH to the case

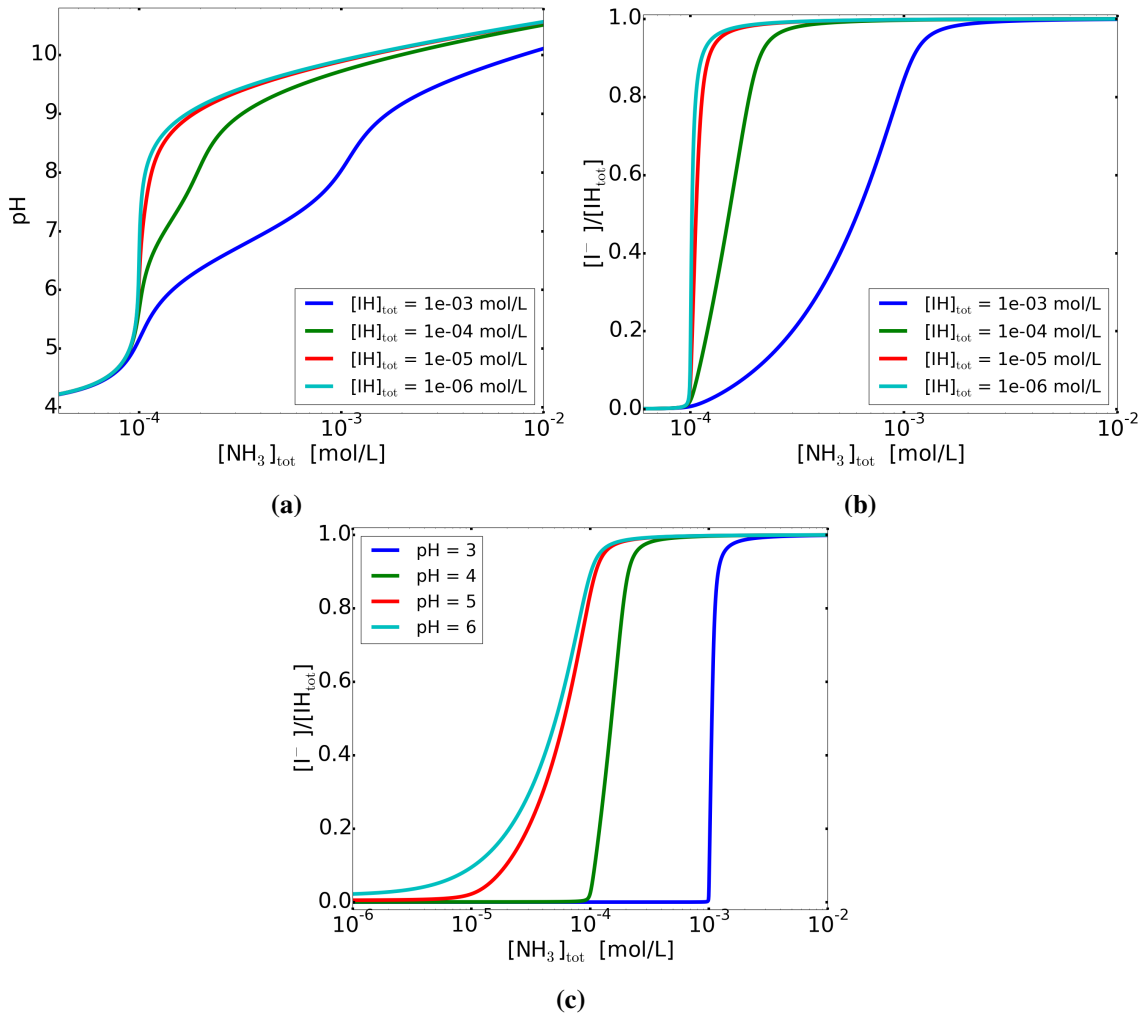

Figure 4.1.: Simulated relations of the chemical components depending on the amount of $[NH_3]_{tot}$: (a) Examples of pH dependencies and (b) the $[I^-]$ dependencies for different $[IH]_{tot}$ values. The HCl concentration was fixed to 10^{-4} mol/L providing initial pH value of 4 and IH_{tot} concentration was varied from 10^{-6} up to 10^{-3} mol/L. Lower concentrations of IH_{tot} ensure steeper dependences of pH value and ratio of fluorescent component I^- to IH_{tot} in relation to NH_3tot concentration. (c) Example of the $[I^-]$ dependencies for different [HCl]. The IH_{tot} concentration was fixed to 10^{-4} mol/L. HCl concentration was varied from 10^{-6} up to 10^{-3} mol/L providing the cases of weak acid with pH value of 6 up to strong acid cases with pH value of 3.

of dominant deprotonated form I^- (see fig. 3.2b). The transformation occurs step-shaped with lower values of IH_{tot}. Hence, there is a trade-off between high fluorescent signal at high Pyranine concentrations and desired step-shaped change in the brightness that can be achieved with low Pyranine concentrations only.

In fig. 4.1c the ratios of fluorescent deprotonated form of Pyranine to the total amount of Pyranine for different [HCl] values, i.e. the initial pH values, are presented. The change to the pH with visible I^- component is observed at the different concentrations of NH_{3tot}. Therefore [HCl] value sets up the boundary limit for the appearance of fluorescent component I^-.

Both relations mentioned above are crucial for further selection of component concentrations used in the experiments.

4.1.2. Depth Profiles for Different Models

To verify the novel BLV technique discussed in sec. 3.2, one needs to simulate the depth concentration profiles of the gas-exchange models described in sec. 2.1.4 for different compositions of the chemicals involved. The brightness profiles, related to $[I^-]$ profiles, are needed to have a sharp drop of the intensity providing the binary representation of concentration profiles.

As the distribution of $[NH_3]_{tot}$ over depth is assumed to comply with the mean concentration profiles for considered models, the distribution of fluorescent Pyranine component $[I^-]$ can be calculated using the function P from sec. 4.1.1.

In this part five different gas exchange models are considered to obtain the mean profiles of $[NH_3]_{tot}$ depth distribution. For each of the $[NH_3]_{tot}$ depth profiles, the resulting profiles of I^- are calculated. The profiles were computed assuming fixed values for the total ammonia concentration at the water surface $[NH_3]_{tot}|_{surface}$ and the mass boundary layer thickness z^*. The distribution of $[NH_3]_{tot}$ was calculated according to the profiles from sec. 2.1.4 with $[NH_3]_{tot}|_{bulk} = 0$. For the calculated value of $[NH_3]$ at every depth, the value of $[I^-]$ was obtained by the use of appropriate P function.

The brightness profiles replicating the shape of $[I^-]$ distribution profiles and the real profiles of $[NH_3]_{tot}$ distribution for film model, small eddy model and surface renewal model at the free and rigid interfaces and fluctuation model (see sec. 2.1.4) are shown in fig. 4.2a–c. The main distinction between the mean I^- profiles and the $[NH_3]_{tot}$ profiles is a steep decrease of concentration at a certain depth. The simulated mean profiles for different models diverge stronger than the real profiles of $[NH_3]_{tot}$ due to sensibility of the BLV technique to the local equilibrium of the chemical system. Fig. 4.2d shows an example of pH value, fluorescent component $[I^-]$ distribution and $[NH_3]_{tot}$ distribution over depth. One can clearly see from this figure, that the steep drop of $[I^-]$ component is due to the drop of pH value from the alkaline condition at the surface to the acid condition in the water bulk. The depth where the drop happens is called neutral depth as the change occurs at pH$\approx$7.

The profiles in fig. 4.2a–d were calculated for a mass boundary layer thickness of 0.2 mm. The Pyranine concentration and initial pH value were fixed to 10^{-5} mol/L and 4, respectively (as those conditions provide the step-shaped brightness profiles, see sec. 4.1.1). Furthermore the same conditions were chosen for further experiments.

In fig. 4.2a–c, the film model, fluctuation model, small eddy and surface renewal models at free and rigid interfaces are presented. As it was described in sec. 2.1.4, the transition from smooth to wavy conditions at the water surface requires a change in the description of the interface from a rigid wall to a free surface. With the wavy surface, i.e. the models at free interface, sufficient to pH change $[NH_3]_{tot}$ values appear at large depths that provides the shift of the brightness profiles towards the water bulk (fig. 4.2a). Therefore, the slope of each calculated $[NH_3]_{tot}$ profiles defines the neutral depth for simulated $[I^-]$ profiles. This can help finding an appropriate gas exchange model that gives a best description of the experimental data at diverge conditions.

In order to understand the functioning of the method in detail, the profiles for one model (surface renewal model at the free interface) were calculated using dissimilar conditions:

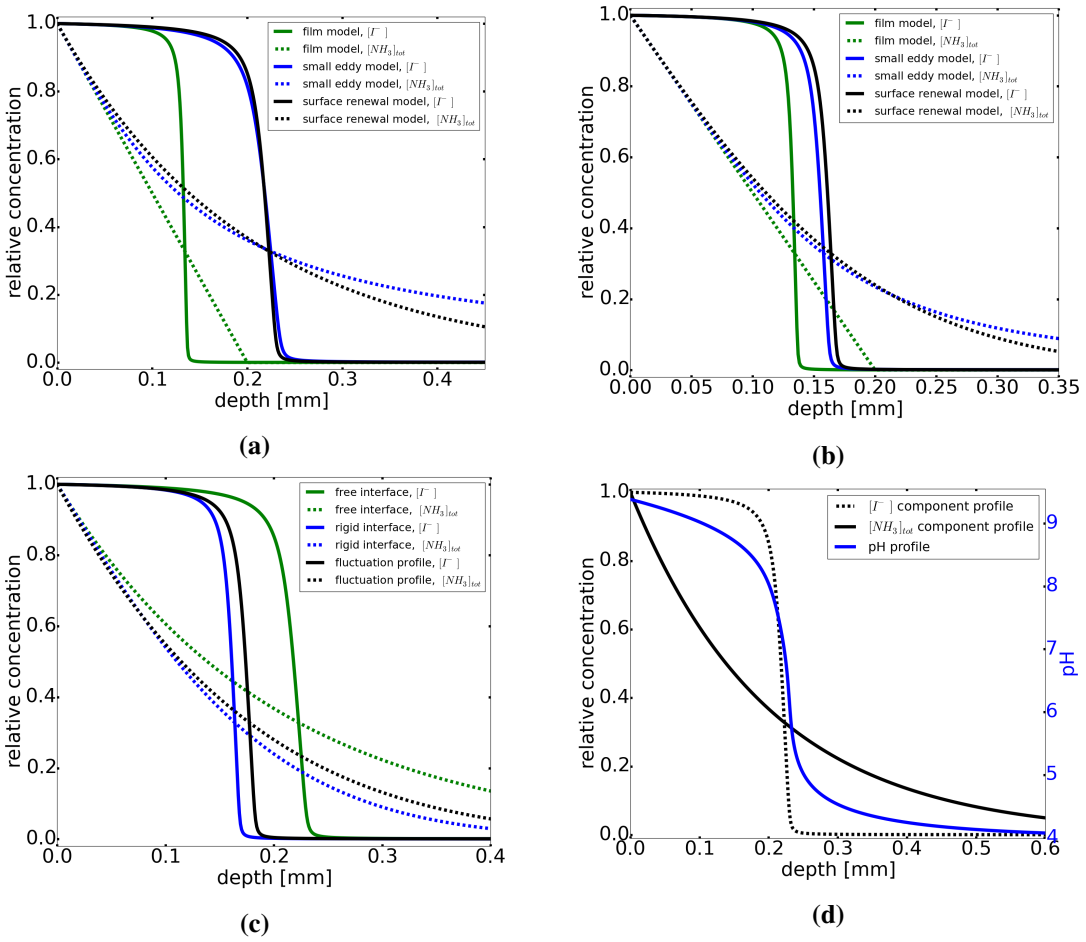

Figure 4.2.: Simulated depth profiles for the gas exchange models: (a) Depth profiles of I^- concentration for the film model, small eddy and surface renewal models at free interface and (b) at rigid interface. (c) Depth profiles of I^- concentration for the surface renewal model at free and rigid interfaces with fluctuation model. (d) The depth profiles of $[NH_3]_{tot}$, $[I^-]$ and pH value for the surface renewal model at free interface. The profiles were calculated with fixed boundary layer thickness of 2 mm, initial pH value of 4 and total concentration of Pyranine of 10^{-5} mol/L.

- **Different Pyranine concentrations**

  As it can be seen in fig. 4.1b, the total Pyranine concentration influences on the shape of $[I^-]$ to NH_{3tot} relation. To understand this effect, one can think of a case of a high Pyranine concentration, comparable to the concentration of H_3O^+ in the water. In this case the dissolution reaction of Pyranine

$$IH + H_2O \leftrightarrow I^- + H_3O^+ \tag{4.7}$$

  would increase the pH value shifting the reaction to the left side of eq. (4.7). Therefore, selection of a reasonable Pyranine concentration is a trade of between the steepness of the brightness profiles and sufficiently high signal-to-noise ratio.

  Fig. 4.3a shows simulated brightness profiles for the case of initial pH value of 4 and boundary layer thickness of 0.2 mm. For the exaggerated case of $[IH]_{tot} = 10^{-3}$ mol/L, the simu-

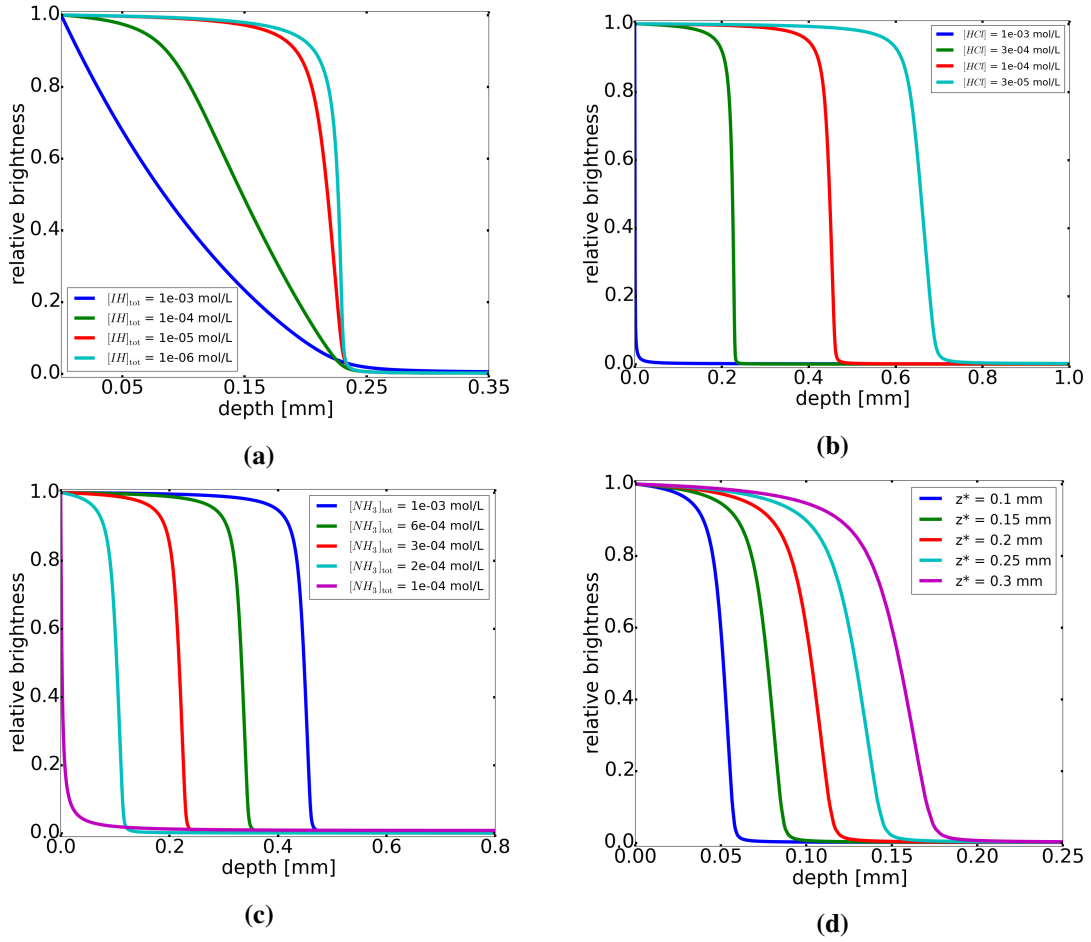

Figure 4.3.: Simulated depth profiles according to surface renewal model at free interface for different (a) IH_{tot} concentration, (b) HCl concentrations, (c) concentration of NH_{3tot} at the water surface and (d) mass boundary layer thicknesses. For the plots (b)-(d) the concentration of Pyranine is fixed to the value of 10^{-5} mol/L. The plots (a),(c) and (d) were calculated with initial pH value of 4. The concentration of ammonia at the water surface was varied from 10^{-3} to 10^{-4} mol/L to ensure the visible change in the profiles for different conditions.

lated profiles presents an unacceptable form with a low-pitched slope. Binary representation of the concentration profiles is not possible as the change in pH value occurs slowly within the mass boundary layer. For the performed experiments the total concentration of Pyranine of 10^{-5} and 10^{-6} mol/L were selected providing close to step-shaped profiles.

- **Different hydrogen chloride concentrations**

  The initial concentration of HCl in the water defines the starting pH value. It determines the critical ammonia concentration required for a sufficient change of pH value, i.e. appearance of fluorescence. At the same time, [HCl] influences on the steepness of the brightness profiles for the reason described above. Fig. 4.3b shows an example of the simulated profiles with four hydrogen chloride concentrations (with a reasonable concentration of Pyranine of 10^{-5} mol/L and high concentration of ammonia at the water surface of 10^{-3} mol/L). To ensure appearance of fluorescent signal at the ammonia concentrations suitable for the facility, the HCl concentration of 10^{-4} mol/L was chosen.

- **Different ammonia concentrations**

  In the fig. 4.3c simulated profiles with different ammonia concentration at the water surface are shown. Within the set, the mass boundary layer thickness is fixed. With the increase of surface ammonia concentration, the condition of pH value larger than 7 is fulfilled for larger distances from the water surface, resulting in larger neutral depths. Therefore, with increasing the ammonia concentration, different depths within the boundary layer can be investigated. The steepness of the profiles is not affected by the change of the NH_{3tot} concentration at the water surface.

- **Different boundary layer thicknesses**

  Fig. 4.3d shows an example of the brightness profiles for different values of the boundary layer thickness. Since the equilibrium state of the chemical system is not changed, the profiles keep their shape and get shifted into the depth with an increase of the boundary layer thickness.

The shape of the depth profiles presented in the fig. 4.3a–b indicates the suitable for binary representation of $[I^-]$ profiles concentrations of Pyranine and initial pH value. The concentrations of approximate 10^{-6} and 10^{-4} mol/L for Pyranine and hydrogen chloride were selected as reasonable values for obtaining step-shaped brightness profiles.

4.1.3. Influence of Carbon Dioxide

As the system is sensitive to slight changes in pH value, the presence of CO_2 in the air might influence on the shape of concentration profiles in the water. An example of a time series recorded with no ammonia gas in air and water at a low wind speed is shown in fig. 4.4. The initial pH value of the water is approximately 10 to demonstrate the invasion of CO_2 into the water with following decrease of pH value. The drop of fluorescence (dark areas in fig. 4.4) can be explained by the local decrease of pH due to the reaction of carbon dioxide with water. In order to check the impact of this effect, the simulations from sec. 4.1.1 were repeated with additional components in the form of dissolved carbon dioxide - HCO_3^- and CO_3^{2-}.

Considering the presence of carbon dioxide in the water, the equilibrium of the carbonate system can be described as:

$$CO_2 + H_2O \overset{K_1}{\Leftrightarrow} HCO_3^- + H^+ \overset{K_2}{\Leftrightarrow} CO_3^{2-} + 2H^+ \tag{4.8}$$

The coefficients K_1 and K_2 are the first and second dissociation constants for carbonic acid in the equilibrium. The dissociation constants are (Jähne, 1980):

$$K_1 = \frac{[HCO_3^-][H^+]}{[CO_2]} \approx 4 \cdot 10^{-7} \text{mol/l} \tag{4.9}$$

$$K_2 = \frac{[CO_3^{2-}][H^+]}{[HCO_3^-]} \approx 2 \cdot 10^{-10} \text{mol/l} \tag{4.10}$$

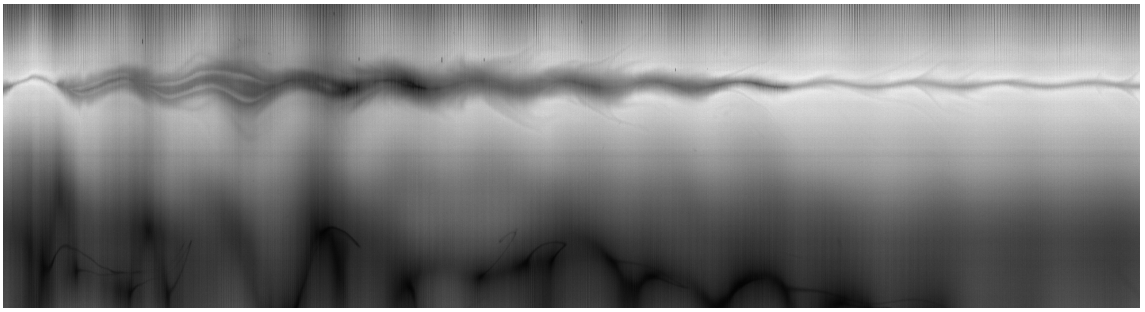

Figure 4.4.: An example of a time sequence of CO_2 invasion to the water causing the change of local pH values. In order to make the pH change visible, the initial pH value was set to 10. The images were recorded with 200 fps. x-direction represents time coordinate with total acquisition duration of 37.5 sec. y-direction represents the water depth of a total length of 10.4 mm. The black line at the upper part of the image is the water surface. Above the water surface the reflection of the light due to the camera tilting is seen. Below the water surface turbulent structure of CO_2 invasion are visible.

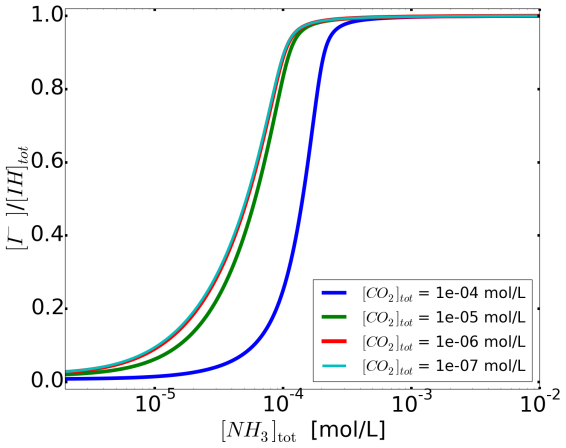

Figure 4.5.: The dependence of the ratio of fluorescent component I^- to IH_{tot} in relation to $NH_{3\mathrm{tot}}$ for different concentrations of CO_2 at the water surface. For the visible difference the initial pH value and Pyranine concentration were set to 6 and 10^{-4} mol/L, respectively. As the red and light blue lines for low concentrations of CO_2 overlap, the profiles for the case with absence of CO_2 will be identical to the profiles of low CO_2 values.

With an example case of initial pH value of 4 (as it was found in sec.4.1.2 as appropriate pH value for the start of ammonia invasion), concentration of CO_3^{2-} can be neglected due to 6 orders of magnitude larger concentration of HCO_3^- (Society, 2005). Therefore, the charge conservation for the chemical system including carbon dioxide is written as:

$$[\mathrm{H^+}] + [\mathrm{NH_4^+}] = [\mathrm{I^-}] + [\mathrm{OH^-}] + [\mathrm{Cl^-}] + [\mathrm{HCO_3^-}] \tag{4.11}$$

Assuming the average of indoor CO_2 level of 400 ppm according to IPCC (2007) and Bakker et al. (2014), CO_2 solubility constant of 0.9 (according to Sander (2014)), the surface concentration of CO_2 lies around 10^{-5} mol/L. Therefore, the simulations were performed as described above with having the air-sided concentration of CO_2 varying from 10^{-7} up to 10^{-4} mol/L. With the initial conditions preselected for further experiments, no visible difference in the profiles was found. To gain noticeable change in the profiles, i.e. shift the system closer to high pH sensible

mode, [HCl] was fixed to considerably low value of 10^{-6} mol/L. The relations of the normalized fluorescent component concentration to total ammonia concentration for different air-sided concentrations of CO_2 are shown in fig. 4.5).

As the only noticeable change in chemical species distribution due to CO_2 impact occurs at high concentrations of 10^{-4} mol/L equal to ≈ 3000 ppm, the presence of CO_2 can be neglected for the concentration profile simulations.

4.2. 1D Profile Measurements

The section includes a full description of measurements performed at the small linear wind-wave facility at the Institute of Environmental Physics at the University of Heidelberg (Winter, 2011). It covers a short overview of the wind-wave channel, the details of the experimental LIF set-up, the experimental routine and the following data processing steps. The section ends with the computational analysis of the images recorded using the novel BLV technique (see sec.3.2).

The measurements of one dimensional brightness profiles were performed at diverse conditions and various concentrations of chemical components in order to verify the capability of the BLV technique along with the simulations performed in sec.4.1.2.

4.2.1. Experimental Set-up

The main components of the experimental set-up are described below.

The wind-wave facility: A complete description of the wind-wave facility can be found in Winter (2011), Warken (2010) and Krah (2014). Here, the details essential for the conducted measurements are described.

In fig. 4.6 a 3D overview sketch of the wind-wave tunnel is shown. The whole facility has a length of about 4 m, a width of about 1 m and a height of about 1.5 m. With a water level of 3.5 cm, the water and air volumes of the tank are 22 L and 220 L, respectively. The turbine on the left side of fig. 4.6 generates wind speeds from 1.5 m/s up to 7 m/s. The wind blows from left to right and is circulated through the pipes in the back of the facility. For easy optical access, the walls, top and bottom of the facility are made of Schott Borofloat 33 glass. Moreover, to allow the measurements of reactive chemicals (ammonia in current case), the facility was built entirely of highly chemically resistant materials. Two top covers of the facility have windows made of fused silica glass with high UV transmittance. One of the covers was used at the measuring section for laser access and another - for concentration measurements with a UV-spectrometer.

A 3D sketch of the full LIF set-up used for one dimensional concentration profile measurements is shown in fig. 4.7. The laser module and focusing optics unit are placed above the top cover of the facility at the measuring section. The laser module is mounted such that the light beam (blue line in fig. 4.7) passes through the fused silica glass window. The light excites the Pyranine molecules dissolved in water and induces fluorescence along the light path (green line). To capture the fluorescent light, two cameras are mounted in front of the side glass wall at the same measuring

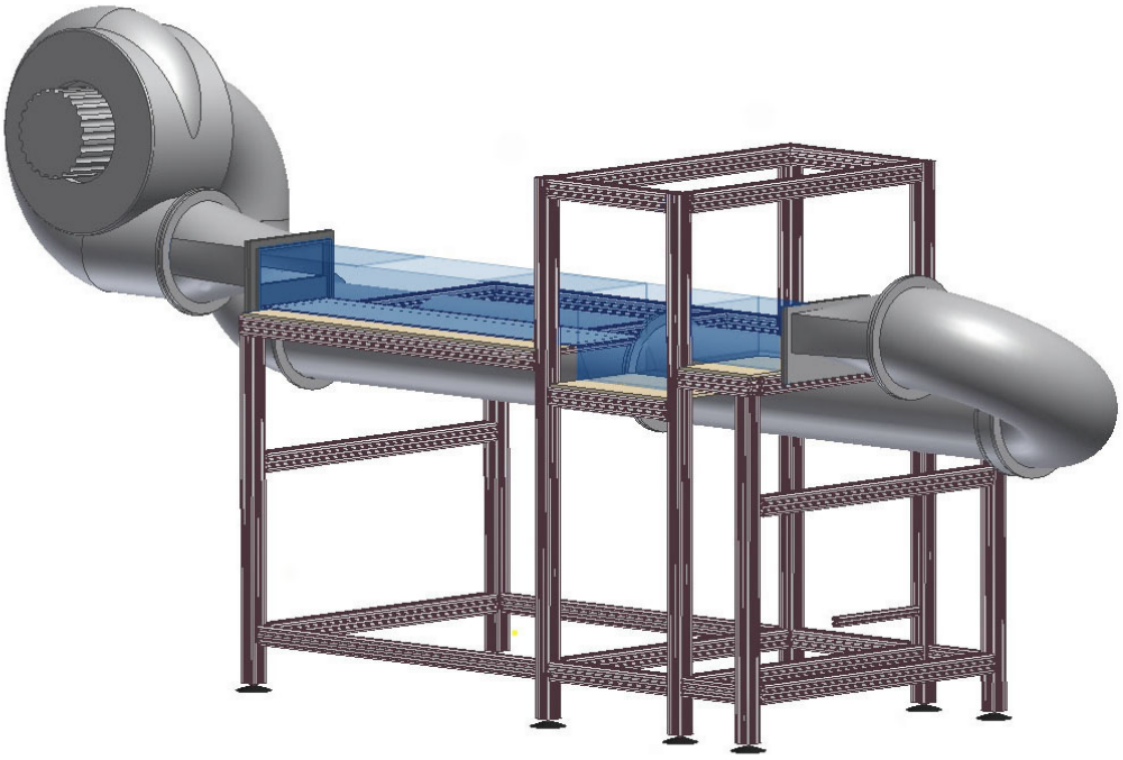

Figure 4.6.: Overview 3-D sketch of the linear wind-wave facility Warken (2010). The blue volume is the glass part, of which the lower part is filled with water, the upper part is the air space. The turbine generating the wind is on the left side. The tubing for the air flow is shown in the back. The measuring section is the area in between the vertical bars with the deeper water level.

section aligned to the laser beam. Worth mentioning here is that the sided location of the cameras are of advantage due to the absence of the reflected laser light from the water surface.

The lower camera is placed closely below the level of the water surface to observe water-sided vertical concentration profiles. The tilting of the cameras is necessary to view the surface point of the water at the wavy conditions. The extreme case with a steep wave slope of an angle s_y being larger than the camera tilting angle δ is presented in the fig. 4.8. Due to tilting of the camera, the recorded images carry the reflection of the fluorescent light from the water surface. Particularly this fact complicates the surface detection procedure (Friedl, 2013). Therefore, the second upper camera is placed symmetrically to the lower camera in order to observe the water surface from the air side of the facility. As the laser beam in the air side is not seen (due to absence of fluorescent molecules in the air), the detection of the water surface position in the image from the upper camera can be realized by a thresholding procedure. This is explained in more details in sec. 4.2.4. Hence, the position of the water surface in the image from the lower camera can be calculated.

The laser: A diode laser with a wavelength of 445 ± 5 nm was used as illumination source. According to the manufacturer's data sheet, the model NANO 250-445-450 by RGB-Lasersysteme GmbH provides maximum laser power of 456 mW and a divergence angle smaller than 0.8 mrad. The shape of the beam is elliptic with a cross section of $1.1 \times 2.8\,\mathrm{mm}^2$. Fig. 4.9a shows the laser controller and the laser head. The controller unit regulates the laser output power with the input

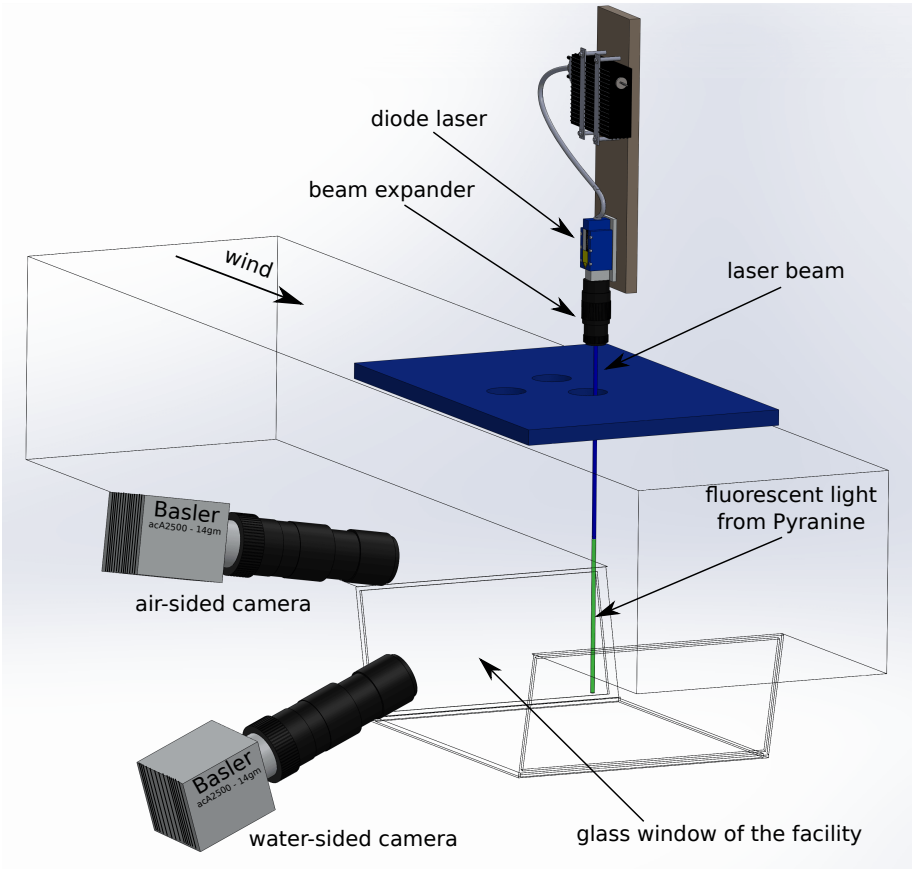

Figure 4.7.: Sketch of the LIF set-up with a segment of the wind-wave facility. The laser module and the focusing optics are place above the cover plate of the facility. The laser beam is focused at the water surface and excites Pyranine molecules mixed in water. Green fluorescent light is captured with two Basler cameras looking through the side glass window. The usage of Scheimpflug optics allows focusing of the cameras tilted in opposite angles to a vertical line.

control voltage. The linear relation of the output laser power and control voltage is presented in the fig. 4.9b. For the measurements the laser power was set at about 50% of the maximum to ensure that the fluorescent dye is not saturated. The laser is thermo-stabilized with a temperature control unit to provide a stable output wavelength and beam shape. The small size of the laser unit allows variable positions of the laser for aligning the beam with the glass window of the cover lid.

Fig. 4.10 shows the shape of the beam profile with no focusing optics. The beam profile was measured by placing a Basler acA2500-14gm camera with no lens facing the laser module at a distance of 45.5 cm. To reduce the light reaching the camera sensor, a reflecting mirror with a transmission coefficient of 1 % and an absorbing neutral density filter with an optical density of 2.5, i.e. transmission coefficient of 0.3 % were placed in front of the camera sensor. In y-direction the beam profile has a Gaussian form and in x-direction - non-Gaussian. The next section describes a procedure for focusing the laser beam in both direction with a beam expander.

The beam expander: A beam expander was used to focus the laser beam from the exit of the laser module onto the water surface at the measuring section. The focusing of the laser beam is essential for following reasons: i) Most importantly, a highly focused laser beam provides high

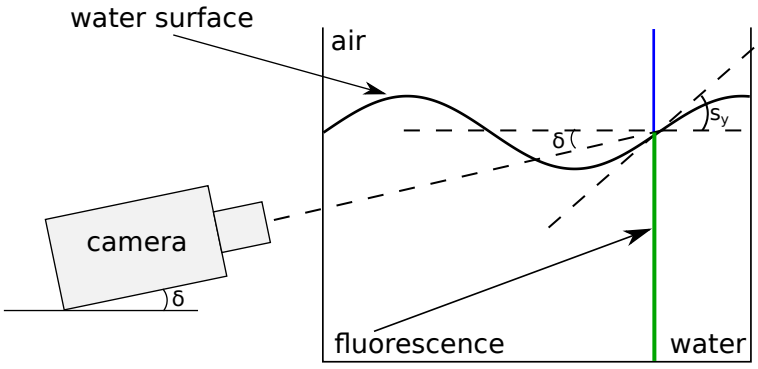

Figure 4.8.: The sketch of the tilted camera at limiting case, when the water surface is not visible due to steep slope of the wave at the focusing position of the laser beam.

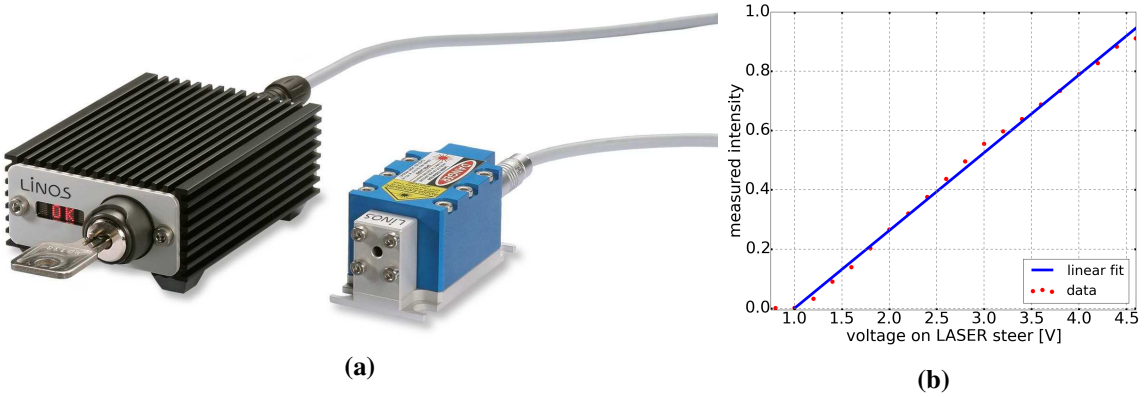

(a) **(b)**

Figure 4.9.: Laser info: (a) Picture of the laser controller and the laser head used for the experiments in the study. (b) Measured laser power in dependence on control voltage with a linear fit function.

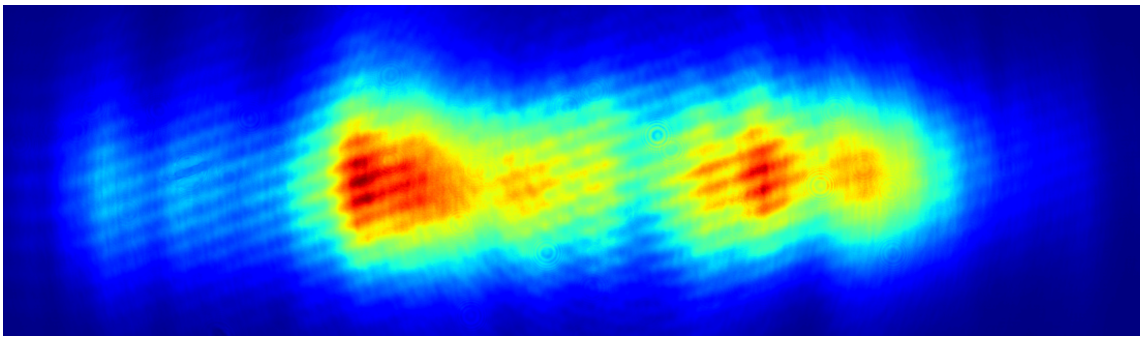

Figure 4.10.: The cross section of the laser beam measured with a beam profiler composed of a reflecting mirror and a neutral density filter. The vertical y-direction has a size of 2.42 mm and the horizontal x-direction has a size of 7.04 mm.

depth resolution. For the unfocused beam, the intensities from different depths appear at different camera pixels. ii) The focusing of the beam ensures acceptable signal-to-noise ratio for low integration times i.e. high frame rates. iii) Further, higher intensities at the water surface secure the capability of the surface detection algorithm.

For the configuration of the beam expander the Galileo arrangement with a diverging and con-

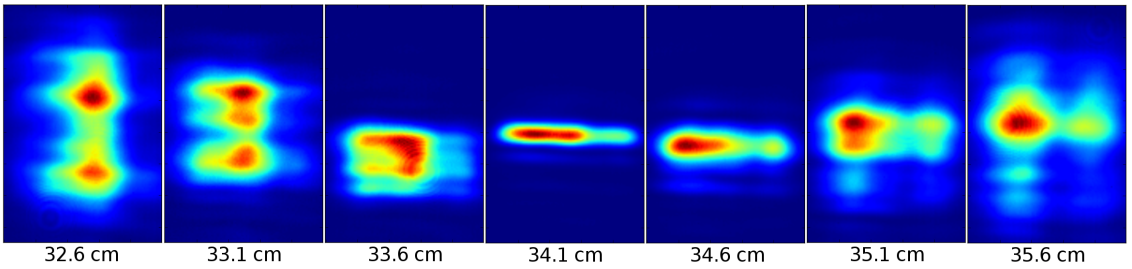

Figure 4.11.: Cross sections of the laser beam collimated with the beam expander. The distance between camera sensor and the end of the beam expander are indicated on the graph. The vertical y and horizontal x directions have a size of 0.78 mm and 0.52 mm, respectively. The images are turned by 90 degrees in comparison to the fig. 4.10.

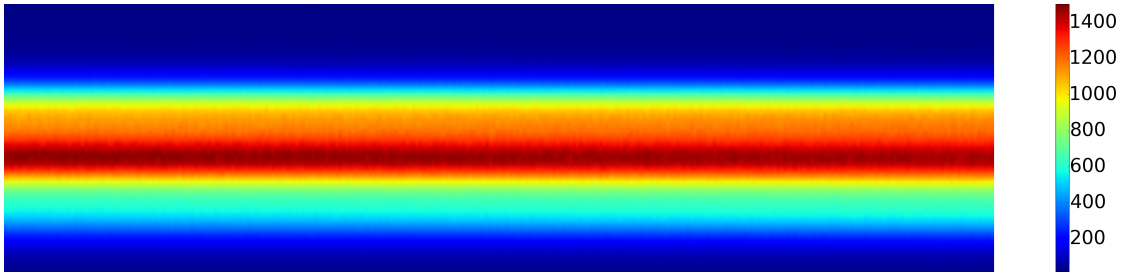

Figure 4.12.: The shape of the laser profile in the water bulk with focusing the laser beam at the water surface. The image is turned by 90 degrees. The image size in vertical and horizontal directions are 1.54 mm and 0.33 mm, respectively.

verging lenses was chosen over Kepler arrangement with two positive lenses. The reasons for this choice are the following: i) While dealing with high powerful lasers, the Galileo configuration allows to avoid massive power densities that occur in the Kepler intermediate focusing point. ii) The Galileo set-up maintains reduced installation length L which is approximately given by L= $|f_1|$-$|f_2|$ compared to the Kepler set-up where L= $|f_1|$+$|f_2|$.

The beam expander was made with a concave and a convex lenses with focal distances of 50 and 100 mm, respectively. The lenses were placed 6.5 cm apart and mounted on the laser exit using the Linos tubing system. The set-up enables to slightly change the distance between the lenses with the range of 6 mm to achieve a suitable position of the laser module. Cross sections of the laser beam were measured by varying the distance between the beam expander and the camera sensor with a shift of 0.05 mm (starting at the distance of 33 cm). Fig. 4.11 presents the cross section profiles with larger intervals of 5 mm for noticeable variation. The working focusing distance of the beam expander was estimated by calculating the standard deviation of the x-axis. A distance of 34.1 cm between the beam expander and the water surface was selected for further measurements. The resulting size of the focusing point is $33\times187\,\mu m^2$. The laser orientation was chosen such that the x-axis of the camera is aligned with the less focused direction of the laser profile.

Fig. 4.12 shows the shape of the laser beam focused at the water surface as it is seen in the water-sided camera. The light is emitted by Pyranine molecules mixed in water. The water surface position is not visible in the image. The selecting of the region is explained in sec. 4.2.4.

The cameras: The visualization of fluorescent light was performed using two Basler acA2500-

14gm cameras with Aptina MT9P031 CMOS sensors. The cameras have a pixel size of $2.2 \times 2.2\ \mu m^2$ and an image resolution of 2592×1944. The full height of 2592 pixels is used for the vertical profile measurements. In the horizontal direction, only 64 out of 1944 lines are read out. The selected region is sufficient for the width of the laser beam and enables higher frame rates. With 64 lines the cameras are able to operate at a frame rate of 363 fps (frames per second) in contrast to the frame rate of 14 fps for the full image resolution. The measurements were performed at 320 fps and 350 fps depending on the conditions of the experiment (laser input voltage, wind speed, Pyranine and ammonia concentrations). The cameras were used in global shutter reset mode with a fixed exposure time for all pixels in the image. The cameras had to be synchronized to be able to detect the water surface. Hence, the cameras were triggered externally with a signal generator. The data were recorded in monochrome mode with a pixel depth of 12 bit.

The camera lenses and adapters: Tamron M118FM50 industrial lenses with fixed focal length of 50 mm and aperture range of f/2.8-22 were used for both cameras. The lenses have minimized distortion of less than 0.1 % with close focusing to shorten the object distance from 0.5 to 0.2 m.

Even though the cameras were located side-ways, additional filtering is needed for elimination of the reflected light from the blue laser. Schneider Kreuznach high-pass color filters 022-MRC were used for this purpose. The cut-on wavelength of the filters is 490 ± 10 nm.

As the cameras are tilted at certain angles, the focal planes are no longer aligned with the plane containing the vertical laser beam. Due to the tilting of the focal planes in the opposite directions, the inclination of the laser beam to achieve an inclined image plane is no longer a solution (the image plane in this case can be aligned with only one of the two inclined focal planes (Bigler, 2002)).

To tilt the focal planes of both cameras back to the vertical plane aligned with the laser beam, a Scheimpflug optic is needed. The basic optical geometry of a Scheimpflug principle is shown in fig. 4.13a. The principle states that if a lens is tilted such that the lens plane intersects the image plane, the plane of sharp focus must also pass through that same line of intersection. This rule applies for thin, rectilinear, flat-field lenses only (Engelmann, 2000; Zang and Prasad, 1997).

The correction for the "thick" lenses Scheimpflug rule is called the Hinge rule and states that the plane of sharp focus, the front focal plane and the parallel-to-image plane intersect along a common line: the Hinge line (see fig. 4.13b).

To satisfy the Hinge rule, two customised Scheimpflug adapters were used in the experiments. Each adapter was placed between the camera and the lens and allowed the tilt of the lens plane by 5 degrees. The fixed angle of the Scheimpflug adapters limits the choice of the distance between the camera sensor and the lens and the distance of the image plane to the observed object in x and y directions. A similar Scheimpflug set-up was presented in Zang and Prasad (1997) and Bigler (2002).

The geometry of the Scheimpflug principle for tilted cameras was modified as the optical path length is different for upper and lower cameras due to different air and water refraction coefficients.

The spectrometer set-up: For monitoring the air-sided ammonia concentration an absorption spectrometer was used. The basic principle of absorption spectroscopy is described by Beer-

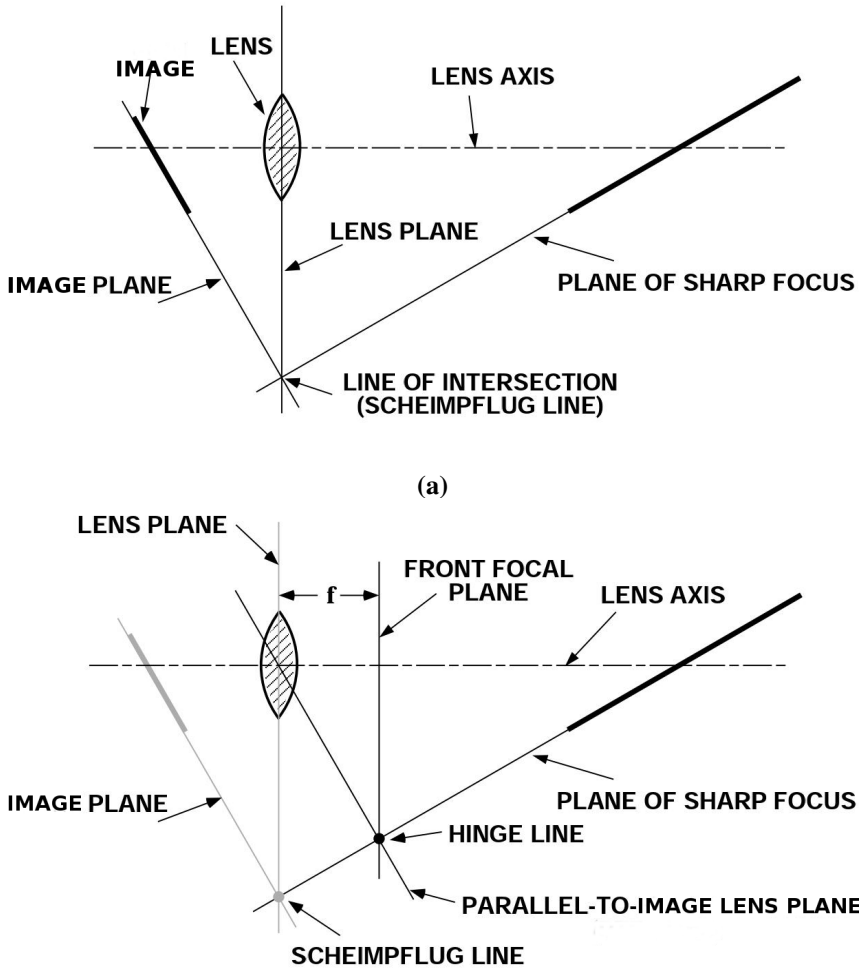

Figure 4.13.: The geometry of Scheimpflug optic (Kerr, 2006): (a) The basic optical geometry of a view camera. The lens axis and the image plane are no longer perpendicular to one another. As a consequence, the plane of sharp focus is tilted. (b) The Hinge rule presents the parallel-to-image plane and front focal plane intersecting with the plane of sharp focus at one single point.

Lambert law:

$$I(\lambda, l) = I_0(\lambda) \cdot exp(-\sigma(\lambda)cl), \tag{4.12}$$

where I is the measured spectrum, I_0 is the light spectrum with no gas in the medium, σ is the absorption cross section and l is the length of the light path. The presence of additional gases in the air side of the facility complicates the calculation of ammonia concentration. Therefore the direct usage of Beer-Lambert law for estimation of ammonia concentration is not feasible. The Differential Optical Absorption Spectroscopy (DOAS) invented by Platt et al. (1979) was selected for current measurements as it allows simultaneous measurements of different gases in the medium. It is also capable of separating the changes in the spectra caused by illumination conditions and actual difference of the gas concentrations. A detailed description of the DOAS technique can be found in Platt and Stutz (2008).

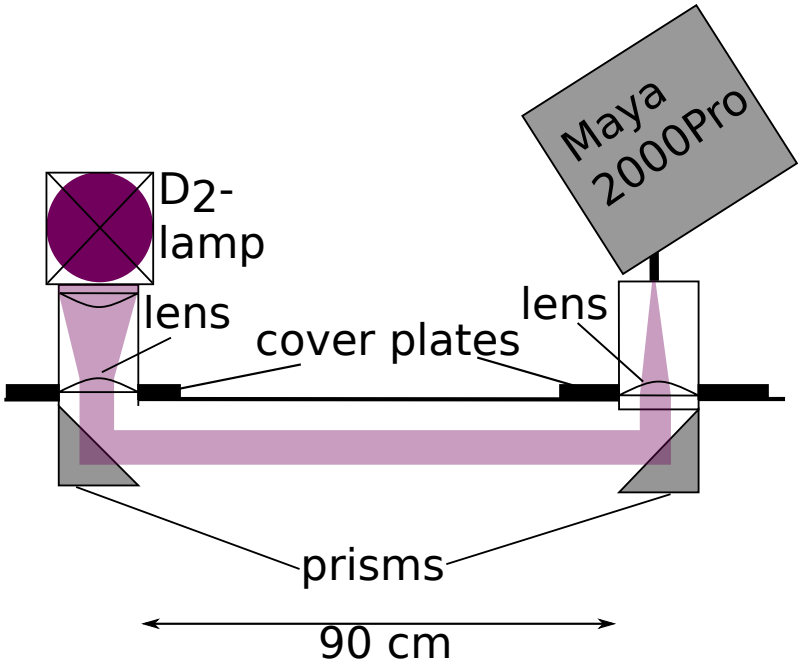

Figure 4.14.: The sketch of spectrometer set-up installed at the linear wind-wave facility. The deuterium lamp was used as a light source. The light path in the air side of the facility is of 90 cm. The Maya 2000Pro spectrometer is aligned with the outgoing light beam for the registration of the spectra.

A custom made UV spectrometer was constructed for the estimation of ammonia concentration. Fig. 4.14 shows the sketch of the spectrometer set-up at the linear wind-wave facility. An Heraeus Deuterium Lamp D_2^{plus} was used as a light source. The path of the light beam is fixed in between the UV lenses. The light beam from the deuterium lamp is focused and polarised by two lenses. By a prism the light is reflected and enters the air side of the facility. It is redirected along the wind direction for 92 cm. With the second reflecting prism and the lens mounted at the measuring section, the light is redirected and focused to the slit of a Maya 2000Pro spectrometer (see fig. 4.15a). The spectrometer is working in a range of 190.5-294.1 nm with a total number of channels of 2068. The recorded spectrum of the deuterium lamp is presented in fig 4.15b. The air-sided ammonia concentration was calculated by evaluation of the measured spectra by *DOASIS* software (Kraus, 2006) with a script developed in Kräuter (2015).

4.2.2. Calibration

The section provides the details of calibration of the LIF optical set-up and calibration of the cameras that are necessary for further data processing.

Calibration of the optical set-up: In order to check the right positioning of the cameras, a Ronchi ruling element with alternating black and white bars of constant width was used as calibration element. An Opal Ronchi ruling with 10 lines per mm was selected for the current study. In fig. 4.16, in comparison to the water-sided image (fig. 4.16b), the air-sided image (fig. 4.16a) appears to be sharper due to higher magnification (due to different refraction coefficient of air and water). The water-sided image is additionally blurred due to the light distortion along the path in

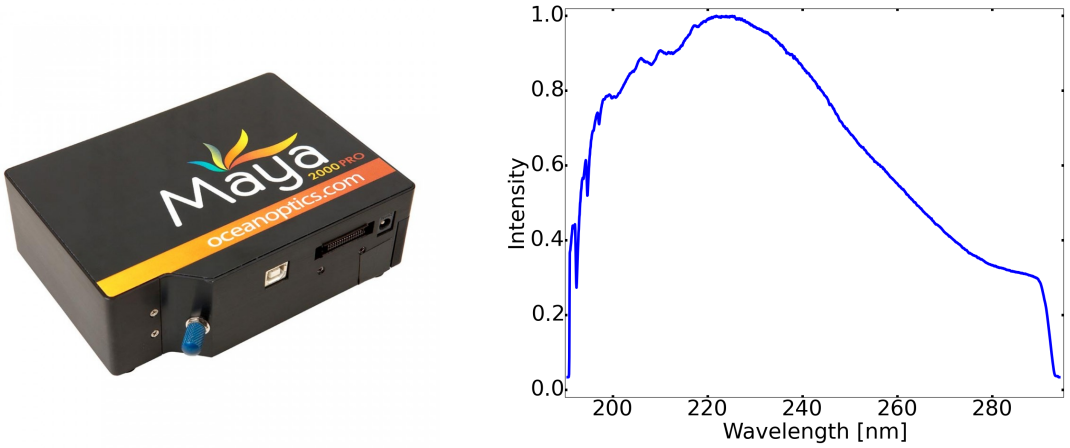

(a) **(b)**

Figure 4.15.: (a) The body of the Maya spectrometer used for the measurements of ammonia concentration. (b) The spectra of deuterium lamp in the absence of ammonia gas in the air side of the linear wind-wave facility.

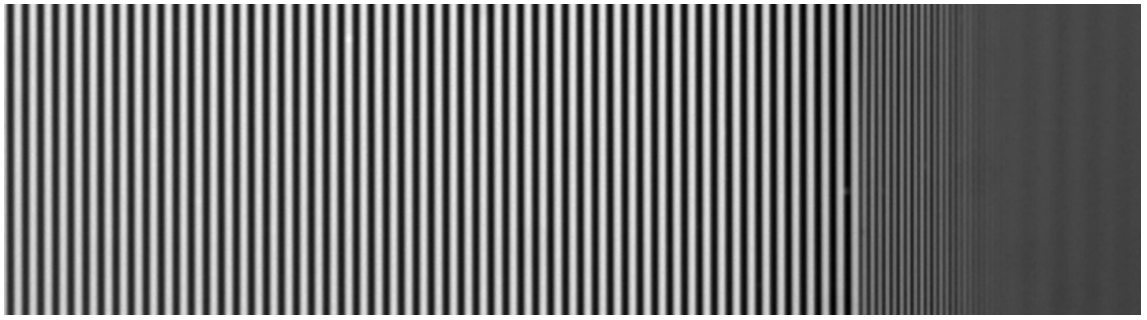

(a)

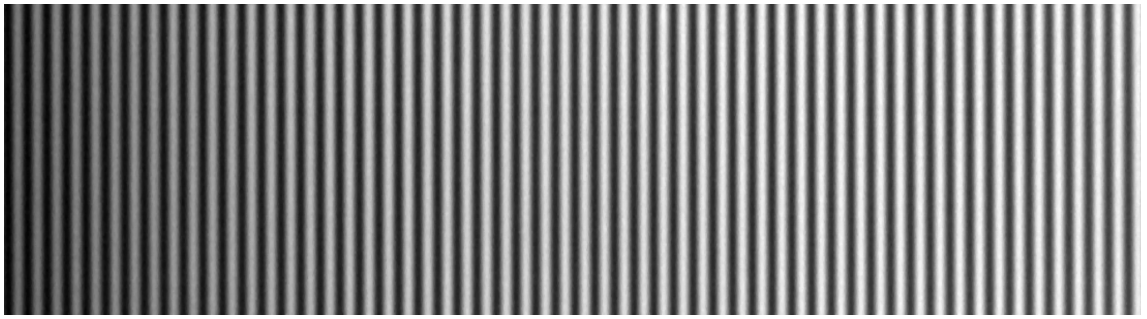

(b)

Figure 4.16.: The images of the Ronchi ruling element taken by (a) air-sided camera and (b) water-sided camera. The dimension of the images are $2.07 \times 7.59\,\mathrm{mm}^2$ and $1.56 \times 5.72\,\mathrm{mm}^2$ for air-sided and water-sided cameras, respectively. The images are turned by 90 degrees.

the water. By tuning the tilting angle and positioning in x and y directions of both cameras, the bright lines of the Ronchi ruling were set up to be at the same distance. With such camera positions the Ronchi ruling element is in the focal planes of both cameras.

Additionally, the Ronchi ruling element was used for calculation of the image scales. The image scales in horizontal direction were calculated for both cameras by detecting the position of the stripes in the images. The horizontal direction in the image corresponds to the vertical

direction in space. The pixel size in object coordinates are 6.89 μm and 5.13 μm for the air-sided and water-sided cameras, respectively.

With the pixel size of 2.2 μm, the magnification factors are 0.319 for the air-sided camera and 0.429 for the water-sided camera.

According to the Beer-Lambert law, the intensity of the laser beam decreases with the distance from the water surface z:

$$I(z) = I_0 \cdot exp(-\epsilon c z), \tag{4.13}$$

where ϵ is the extinction coefficient, c is the concentration of Pyranine and I_0 is the intensity of the laser beam at the water surface. According to Herzog et al. (2010), the extinction coefficient of Pyranine is $2.44{\cdot}10^4\,\mathrm{M}^{-1}\mathrm{cm}^{-1}$ for high pH values of about 10. Assuming the chosen in sec. 4.1.2 Pyranine concentration of 10^{-6} mol/L and entirely fluorescent water bulk, the drop of the intensity is estimated to be less than 0.1 %. Therefore the correction for the decrease of the fluorescent intensities over depth can be excluded.

Calibration of the cameras: To minimize fixed-pattern noise for every taken image, a dark image is subtracted from all recorded images. The dark images were taken for both cameras at the same exposure time as the images during the experiments.

The images needed to be corrected for shading and vignetting effects of the camera lenses, filters and most importantly of the fact that the camera sensor is not aligned to the lens plane due to the presence of the Scheimpflug adapters. For that purpose the cameras with sensor-to-lens orientation identical to sensor-to-lens orientation during the experiments were placed in front of a homogeneous illuminated surface, Ulbrich sphere.

First, the average over 10000 frames dark images for each camera were subtracted from the recorded images as well as from the images of the Ulbrich sphere. Then, every taken image from both cameras was divided by the normalized images of the homogeneous illuminated surface.

4.2.3. Experimental Procedure

For the experiments, the linear facility was filled with deionised water up to a filling level of 3.5 cm providing the water height at the measuring section of 12.3 cm and a water volume of 22 L. To gain an initial pH value of 4, 2.2 ml of 1 M solution of hydrogen chloride was injected and well mixed in the water. The air and water side of the facility were closed. The desired wind speed was turned on in advance in order to reach wave equilibrium. Ammonia gas was injected into the air side of the facility. A bubble flask with 25 % ammonia solution was used. CO_2 free air was bubbled through the ammonia solution with saturated air in the bubble flask being injected into the facility at the right end of the tubing system (see fig. 4.6). The ammonia injection was regulated by a flux controller with the working range of possible fluxes from 0.2 up to 20 ml/min. The laser power was switched on in advance as the laser module needs certain time to gain a stable beam profile. The recording of the images was started manually by a *Heurisko* workspace after reaching an approximate equilibrium of ammonia in the air side. This was possible by simultaneously

monitoring the ammonia concentration by *DOASIS* software.

The experiments were divided into three subsets determined by the conditions the concentration profiles of ammonia were measured at:

I Ammonia concentration: The experiments were performed with a fixed Pyranine concentration and initial pH value. A Pyranine concentration of 10^{-6} mol/L and a pH value of 4 were selected to ensure the steep shapes of the brightness profiles as shown in the sec. 4.1.2. The wind speed was set to the lowest value with a turbine frequency of 5 Hz, providing a friction velocity of 2.46 cm/s, that maintained the condition of no waves (Krah, 2014). The condition of no waves was preferable in order to eliminate detachment events, that take the bright fluorescent areas from the water surface down to the water bulk. Those events disturb the statistics of constant neutral layer depth due to appearance of fluorescent at different depths. This set was thought to provide experimental profiles with constant, but different neutral depth as in fig. 4.3c. For the different ammonia fluxes, the range of ammonia concentrations was 10 to 50 ppm.

II Pyranine concentration: The second set of experiments was conducted with fixed wind speed, ammonia concentration, initial pH value but different Pyranine concentration to verify the change in steepness of the profiles as it is shown in fig. 4.3a. The condition of no waves was fulfilled for the same reason explained above. The concentration of the Pyranine was varied from 10^{-6} up to 10^{-5} mol/L. Higher concentrations were abandoned due to over saturation of the images at the lowest laser power. The initial pH value was set to 4. The flux rate for ammonia injection was kept constant to provide similar ammonia concentration in the air side of the facility.

III Wind speed: The final set of different wind speed values was performed to investigate the scales and frequencies of the turbulent eddies, most importantly surface detachment events. A pH value of 4 and a Pyranine concentration of 10^{-6} mol/L were used for this set. The turbine frequency was varied from 5 up to 11 Hz yielding the range of friction velocities from 2.46 up to 6.41 cm/s. The flux rate of ammonia injection was adjusted within the subset for every wind speed which provided constant ammonia concentration of about 14 ppm.

The summary of the conditions used during the measurements of the three sets are shown in the tab. 4.1. For the three sets the laser power was set to 50 % of maximum power (from 1.5 up to 1.8 mV) to avoid photo-bleaching effects. For most of the measurements an integration time of 2.5 ms was used that allows high temporal resolution which is necessary to resolve fast turbulent events at the friction velocities up to 6.41 cm/s. Such settings allow to perform the measurements with the rate of 320 fps. The images were recorded continuously for 3.4 minutes. Longer acquisition times were not feasible due to fast changes of the conditions in the facility.

4.2.4. Data Processing

During the experiments at the linear wind-wave facility, the data were recorded in image sequences of 65535 single frames of 64×2592 pixels. Each pixel is presented as a single integer value of 12 bits, i.e. a gray value between 0 and 4095.

Set number	f [Hz]	u_* [cm/s]	NH_3 [mL/min]	IH_{tot} [mol/L]	pH	T_w [°C]
I	5	2.46	4.0	10^{-6}	3.9	23.3
	5	2.46	5.0	10^{-6}	4.0	22.9
	5	2.46	6.0	10^{-6}	3.9	23.3
	5	2.46	7.0	10^{-6}	3.8	23.5
	5	2.46	8.0	10^{-6}	3.8	23.4
	5	2.46	10.0	10^{-6}	3.8	23.3
	5	2.46	15.0	10^{-6}	3.8	23.4
	5	2.46	20.0	10^{-6}	3.7	22.8
II	5	2.46	4.0	10^{-6}	3.7	23.1
	5	2.46	4.0	$2{\cdot}10^{-6}$	3.8	22.8
	5	2.46	4.0	$5{\cdot}10^{-6}$	3.9	22.9
	5	2.46	4.0	$8{\cdot}10^{-6}$	3.9	22.7
	5	2.46	4.0	10^{-5}	3.8	22.9
III	5	2.46	5.0	10^{-6}	3.9	23.4
	6	3.13	6.0	10^{-6}	4.0	22.7
	7	3.74	6.5	10^{-6}	3.9	23.5
	8	4.51	7.5	10^{-6}	3.7	23.3
	9	5.46	8.0	10^{-6}	3.7	22.8
	10	6.11	9.0	10^{-6}	3.9	23.3
	11	6.41	10.0	10^{-6}	3.9	23.1

Table 4.1.: Measurement conditions at the linear wind-wave facility according to the three sets described above - different ammonia concentration, different Pyranine concentration and different wind speed conditions. The friction velocities u_* for different were taken from Krah (2014).

The scheme of the data processing of recorded images is presented in fig. 4.17. The computational algorithm was subdivided in two separate steps. The analysis of the air-side images yields the water surface position for each frame. From the known correspondence of the air- and water-sided cameras, the water surface position in the image coordinates of the water-sided camera is computed. This information is then used in processing the water-side images.

At first, the recorded images from both cameras were corrected for the fixed-pattern noise, shading and vignetting effects (see sec. 4.2.2).

Center selection: The recorded images were cut off around the maximum value of the laser beam. This was performed for including minimum level of noise during the width-averaging procedure as the signal-to-noise ratio decreases towards the side regions of the image. This procedure as well improved the time performance of the surface detection algorithm.

For each single frame, the depth-averaged fluorescence profile was fitted with a Gaussian function as shown in fig. 4.18a. The central points of the profile were selected for further processing. An example of the 7 points selection is shown in fig. 4.18b. In comparison to 3 and 5 pixels wide regions, 7 pixels as a width of final selected region gave better results and speed up the computational process in comparison to larger areas.

Surface detection: The surface detection algorithm was performed on the images from the air-

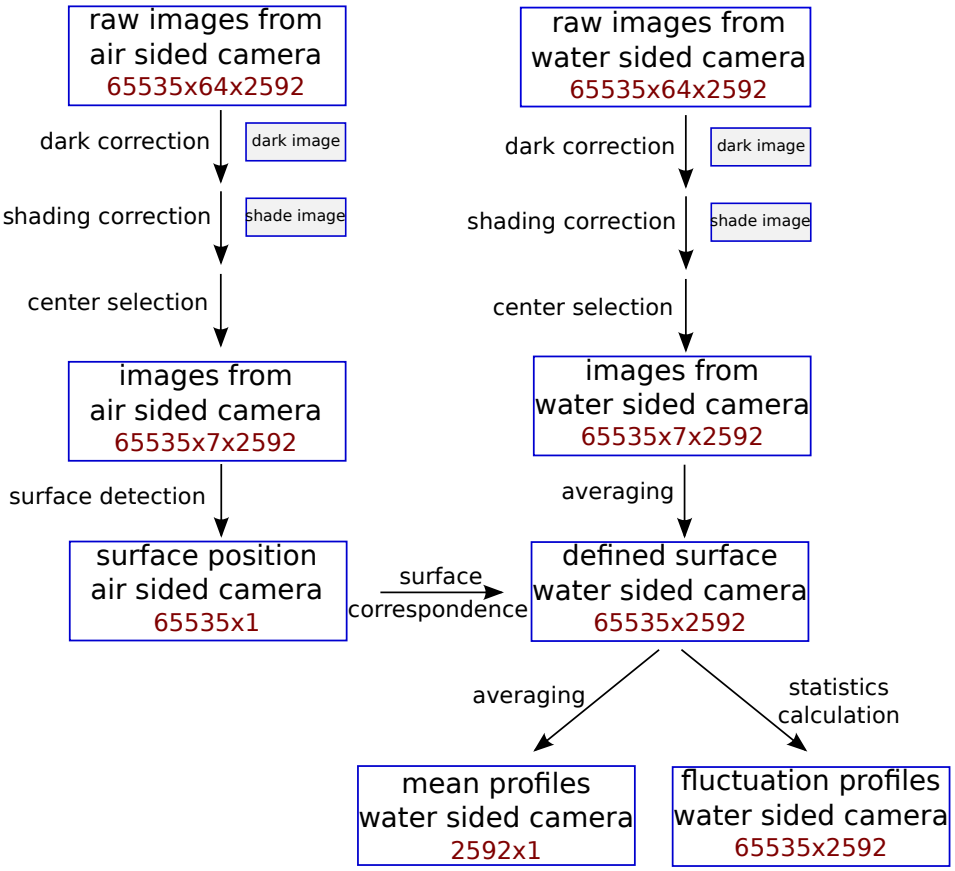

Figure 4.17.: The scheme of data processing of LIF images from air-sided and water-sided cameras.

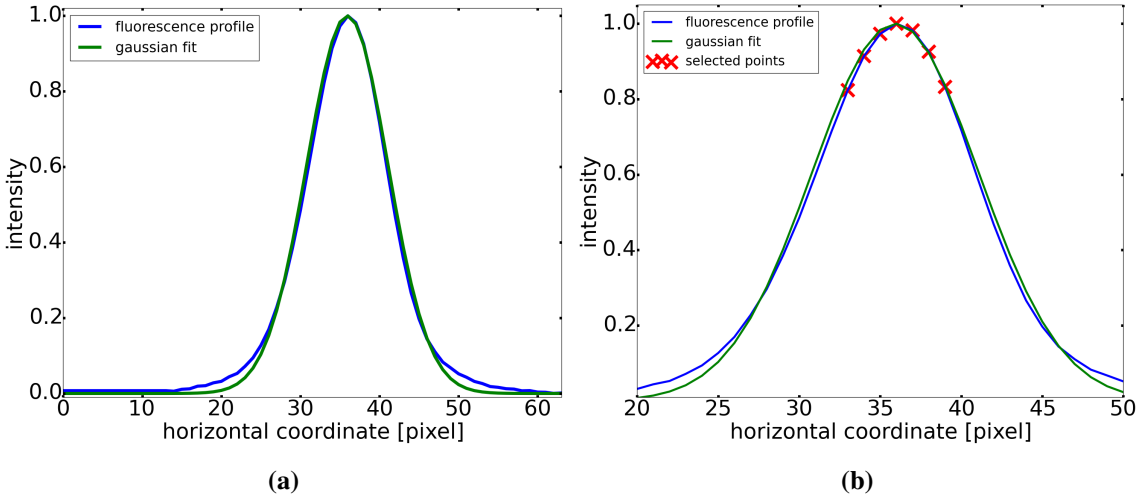

Figure 4.18.: (a) Fluorescence profile averaged over the depth coordinate with a Gaussian fit. (b) The 7 points centered at the maximum of a Gaussian fit were selected for the averaging procedure.

sided camera that were cut off within the preselected region. The surface detection algorithm was carried out in the following steps: i) Image binarization was performed using an adaptive thresh-

olding algorithm. The usage of a global threshold value was not acceptable due to the complicated behaviour of the fluorescence close to the water surface. A block size of 5 pixels was used to calculate an adaptive threshold value for the local neighbourhood. *ADAPTIVE_THRESH_MEAN_C* function from *OpenCV* package in *iPython* was used. The binarization procedure arranged in this way does not include a data loss of the observed fluorescent scene. ii) The edges in the binary images were detected by the use of Canny filtering. The depth of the first found straight horizontal line (presence of brightness along the width direction) was assumed to be the depth of the water surface.

As turbulent processes occur at wavy conditions and effect the fluorescent patterns, additional constraints were included to improve robustness of the detection algorithm. An upper boundary on the change of the water surface level between two successive frames could be safely placed. The value of the permitted shift of the water surface was varied from 5 up to 30 pixels for different wind speed conditions. If the condition was not fulfilled the step i) of the surface detection algorithm was repeated with global threshold value. This step guarantees the determination of the water surface even at the low fluorescent intensities as well as for thin fluorescent structures.

If the water surface position was not found, the current frame was noted as a frame with undefined surface position and was assigned the position of the water surface from the previous frame. At last, the curve of the water surface was smoothed by the use of a Gaussian filter.

Examples of the time sequence images from the air-sided camera with the estimated position of the water surface are presented in fig. 4.19. Conditions with low wind speeds, i.e. non-wavy water surfaces, do not comprise any difficulties for the algorithm. Fig. 4.19a shows an example with a friction velocity of 2.46 cm/s. At higher friction velocities (e.g. 6.11 cm/s, see fig. 4.19b), areas of low fluorescent intensities may occur at the surface. The algorithm is still able to estimate the position of the water surface. For the highest friction velocity used in the experiments - 6.41 cm/s - regions of undefined water surface position (fig. 4.19c) are present. However the algorithm is still able to snap the surface positions in upcoming frames.

Surface correspondence: The transformation from the coordinate system of the upper camera images to the coordinate system of the lower camera images is assumed to be linear. The assumption is based on the achievement of the focal planes of both cameras being align with the plane of the laser beam. Therefore, the transformation of the coordinate systems does not include rotation but scaling and shifting and, thus, can be expressed by a linear function. The linear function was estimated by finding the peaks in the images of Ronchi ruling (fig. 4.16) and further used to achieve the position of the water surface in the lower camera images.

Water-sided time sequences of fluorescence profiles for the friction velocity of 3.74 cm/s are presented in fig. 4.20. The raw sequence including the reflection of the fluorescence at the water surface is shown in fig. 4.20a. Using the known water surface position, the reflection can be discarded (see fig. 4.20b).

Averaging: Mean fluorescent brightness profiles are obtained by averaging the time sequences along the time coordinate. As the images were taken at wavy conditions, the surface elevation due to the waves needs to be taken into account. This can be performed by transforming the vertical

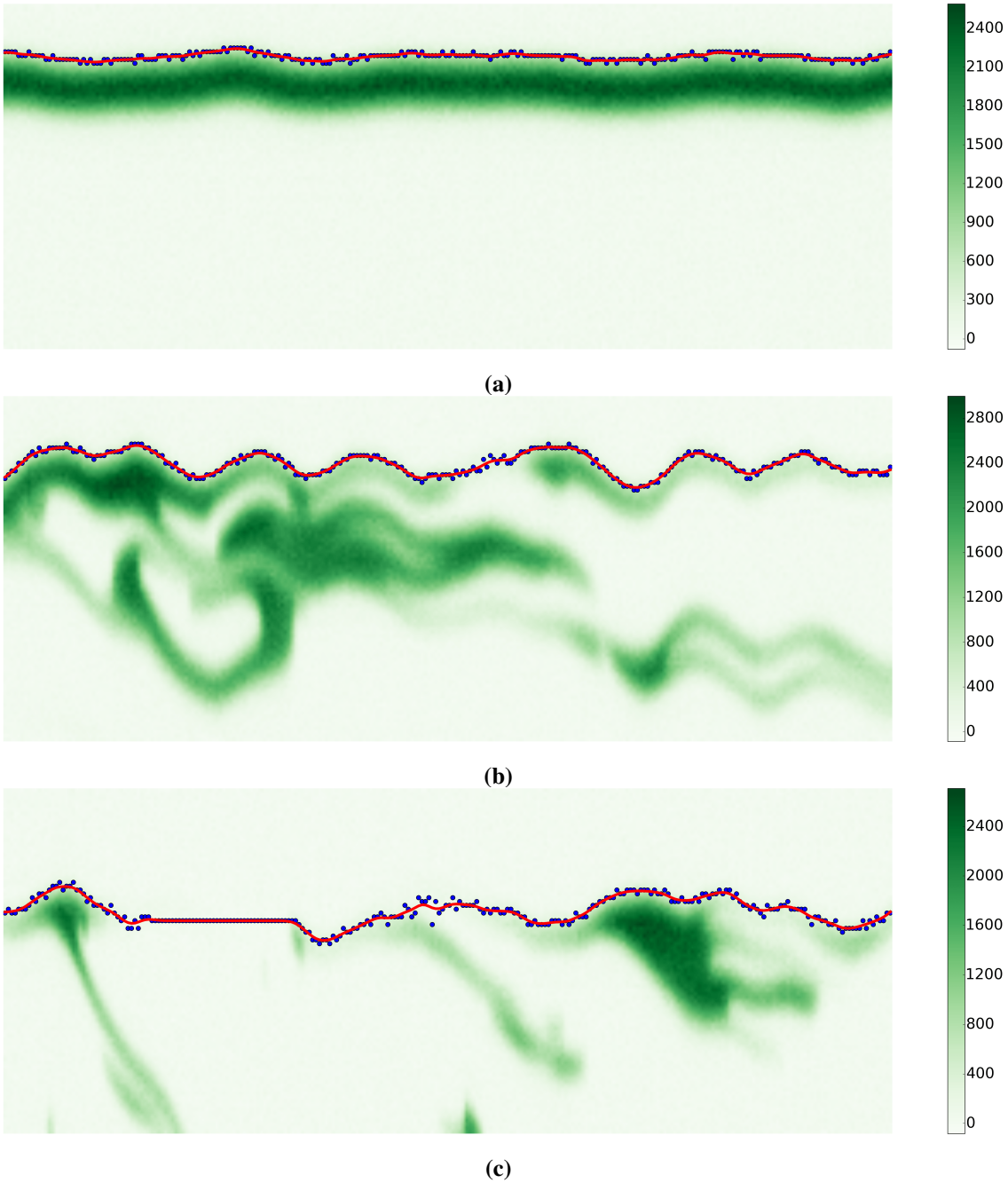

Figure 4.19.: The performance of the surface detection algorithm on the images from the air-sided camera. Blue dots represent the estimated surface position for each frame, the red solid line is Gaussian-smoothed water surface. The scale of the images is 0.65 s and 0.62 mm in time (horizontal) and depth (vertical) directions, respectively. (a) The image at low friction velocity of 2.46 cm/s with no turbulent structures. The algorithm finds the surface position with no failure. (b) The image at 6.11 cm/s with presence of turbulent events. The turbulence disturbs the water surface and causes the transport of the fluorescent structures from the water surface to the water bulk. With low intensities at the water surface, the algorithm is able to snap the position of the water surface due to soft thresholding and additional constrains. (c) The image at a friction velocity of 6.41 cm/s with presence of areas with no fluorescence close to the water surface. The algorithm is not able to estimate the water surface position. However, it is able to find the water surface in upcoming frames.

profiles of a single frame to the relative depth of the water surface. The correct coordinate system for measuring the water depth is a curvilinear coordinate system. The curvilinear coordinate sys-

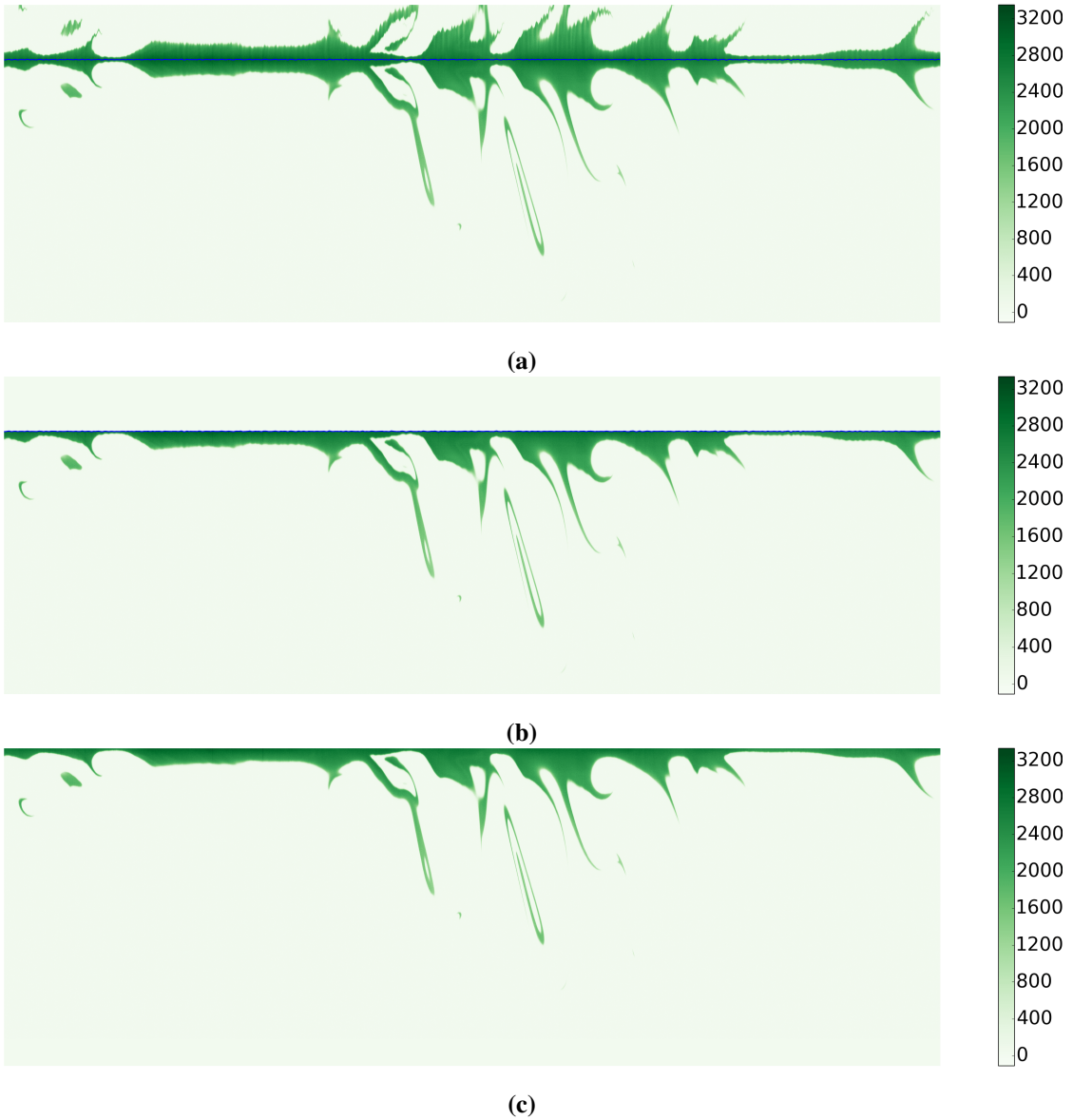

Figure 4.20.: The data processing of the images from water-sided camera. The scale of the images is 18.75 s and 11.96 mm in time (horizontal) and depth (vertical) directions, respectively. (a) The image contains the reflection of the fluorescence from the water surface. The blue line represents the water surface position. (b) The reflection from the water surface is removed by eliminating the bright areas above the water surface. (c) The image contains the concentration profiles being transformed to a curvilinear coordinate system.

tem includes the temporal and spatial modification of the water surface. According to Hsu et al. (1981) the transformation of the image coordinates to the wave coordinate system is performed by vertical shift:

$$z = z^* + f(z^*) \cdot \eta(t) \tag{4.14}$$

where z is the depth in the image coordinate system, z^* is the depth in the curvilinear coordinate system, η is the water surface elevation and $f(z^*)$ is a function that decreases monotonically from the value of 1 at the water surface to the value of 0 at the bottom of the facility. Assuming, that the

water surface ascent is small, the vertical shift satisfies:

$$z = z^* - \eta(t) \tag{4.15}$$

The resulting image of the time sequence from fig. 4.20a in the curvilinear coordinate is shown in fig. 4.20c.

The mean brightness profiles were calculated by averaging the profiles in the curvilinear coordinate system over the number of recorded frames [1] under fixed condition. The single frame profiles with unknown positions of the water surface were eliminated from the averaging procedure. A similar procedure was performed by Friedl (2013).

Analysis of turbulent structures: The time sequences of the profiles from the water-sided camera were analysed to calculate the statistics of observed turbulent structures.

The estimation of the neutral layer depth z_{nl} in analogy to the estimation of the mass boundary layer thickness δ_{mbl} with eq. (2.24) is no longer possible as the profiles have a step-shaped drop at a certain depth. Therefore, the neutral layer depth z_{nl} was estimated for each frame using an adaptive thresholding algorithm on the concentration profiles transformed to the curvilinear coordinate system.

An algorithm for statistical analysis of the depth distribution of the turbulent structures and the frequencies of separate single detachment events was written in *iPython*. The detachment event was considered to take place if multiple fluorescent areas over depth were separated by blank regions. For single frame the number of fluorescent patterns and their depth were calculated. If in the following frame the structures kept similar form, the detachment event was considered as time continuation of the previous event. Additionally, the scales of the single separate structures in space coordinates were estimated.

4.3. Results of 1D Measurements

4.3.1. Time Images of 1D Profiles

Examples of the temporal development of ammonia concentration profiles for different wind speeds are presented in the form of time-depth images (*t-z* images) in figures 4.21 and 4.22. The images were obtained by implementing the data processing steps as described in sec 4.2.4 in *iPython*. For each wind speed, the water surface position was calculated from the air-sided camera images and then reassigned to the images from the water-sided camera.

The surface detection algorithm developed in this study is robust to the shape of the profiles from the water-sided camera, i.e. the presence of the reflection from the water surface depending on the wave slope. The dependence of the surface detection on wave slope was one of the main issues of the detection algorithm of Friedl (2013). If no fluorescence is observed at the air-water interface, the presented surface detection algorithm fails. This does not imply that no ammonia is

[1] Mostly 65535 frames were considered for averaging. Unless the conditions at the high wind speeds were changing fast, the full sequence was divided in parts.

(a)

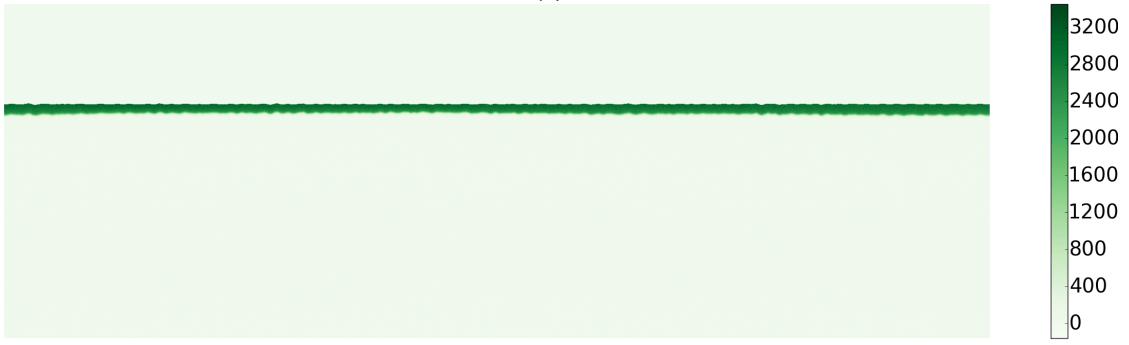

(b)

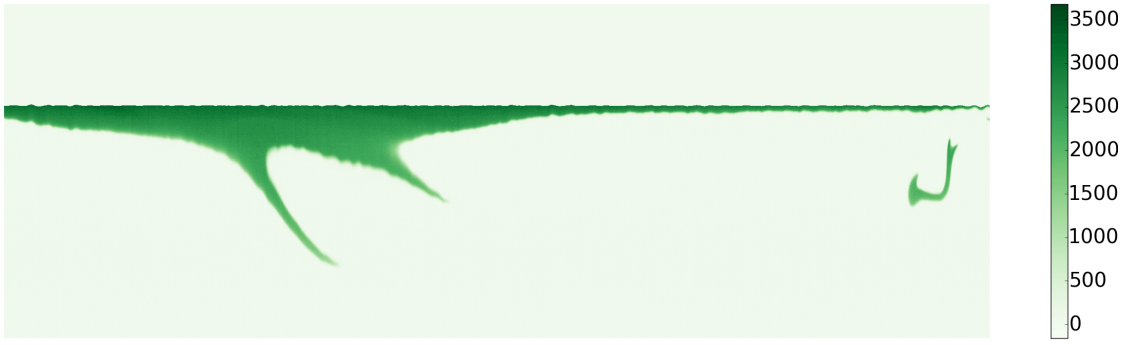

(c)

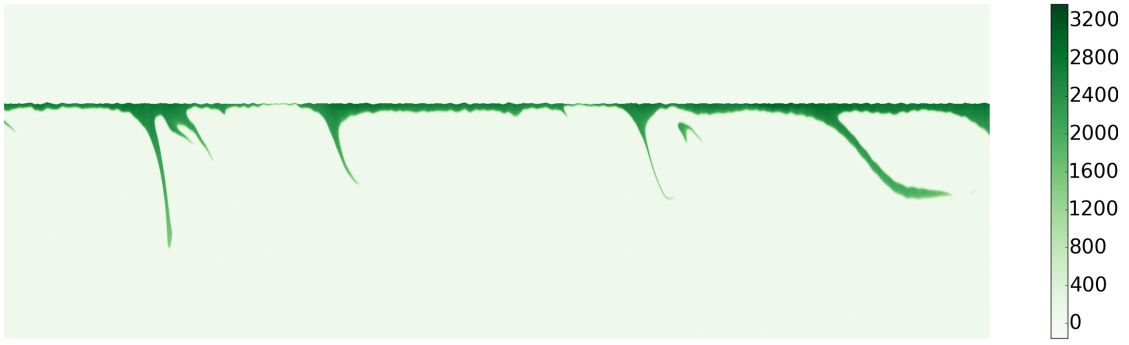

(d)

Figure 4.21.: The *t-z* images from the water-sided camera at a friction velocity of (a) 2.46 cm/s, (b) 3.13 cm/s, (c) 3.74 cm/s and (d) 4.51 cm/s. Shown images are false-color images with relative intensity values. The scale of the images is 10.0 s and 6.76 mm in time (horizontal) and depth (vertical) directions, respectively. The images were recorded at similar air-sided ammonia concentrations of roughly 14 ppm.

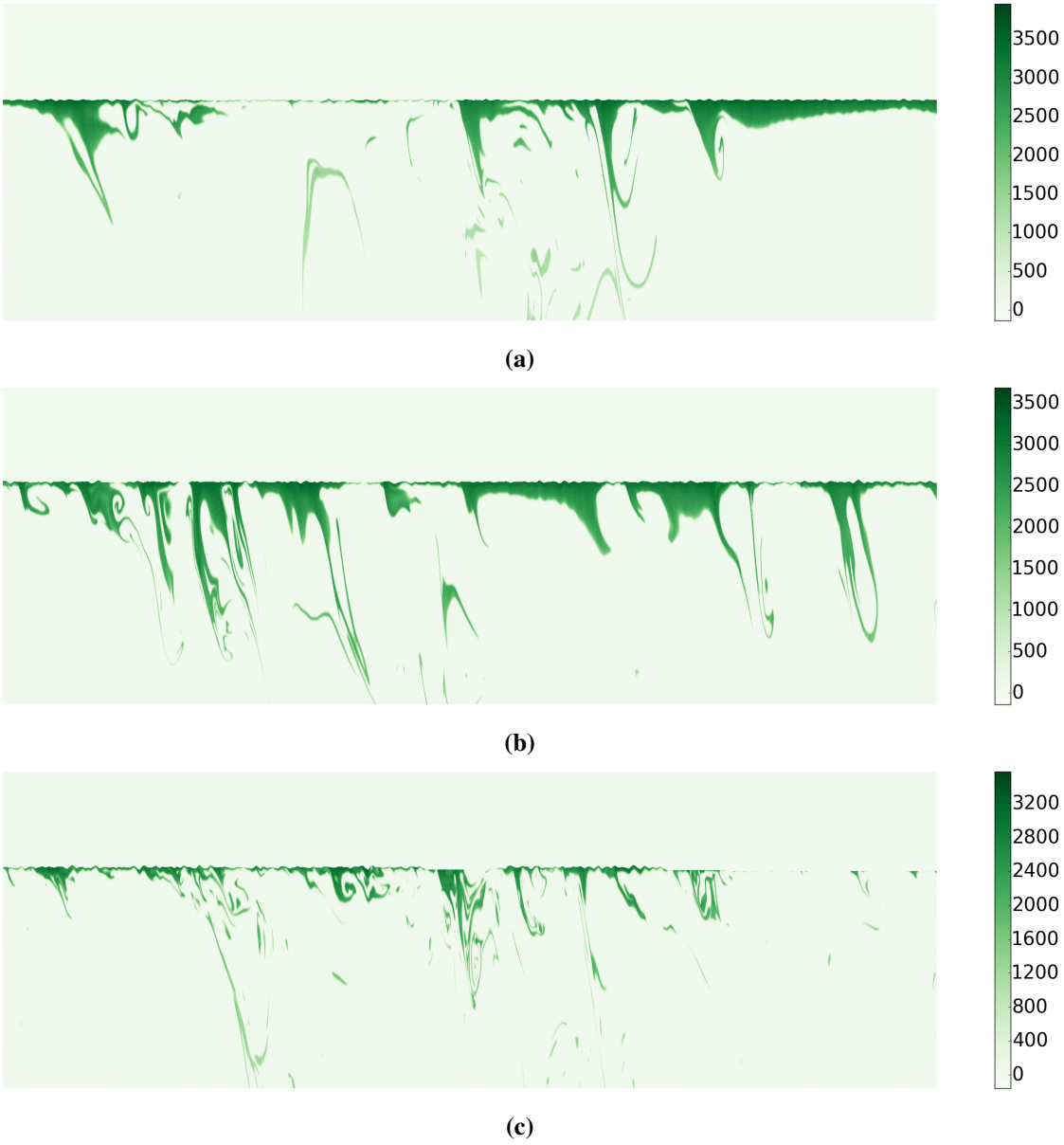

Figure 4.22.: The *t-z* images from the water-sided camera at a friction velocity of (a) 5.46 cm/s, (b) 6.11 cm/s and (c) 6.41 cm/s. Shown images are false-color images with relative intensity values. The scale of the images is 10.0 s and 6.76 mm in time (horizontal) and depth (vertical) directions, respectively. The images were recorded at similar air-sided ammonia concentrations of roughly 14 ppm.

present, only that the concentration is not sufficiently high to increase the pH value to 7. For each frame the concentration profile was transformed to the curvilinear coordinate system described in sec. 4.2.4.

The images in the figures 4.21 and 4.22 have a time scale of 10 s (x-direction). The y-direction is the depth coordinate and captures the water bulk till about 6.7 mm from the water surface position. The images are selected from the full sequences to provide with the typical examples of the turbulent structures for each wind speed condition.

At low wind speeds the water surface is flat. In fig. 4.21a and 4.21b, the friction velocity is 2.46 and 3.13 cm/s and no turbulent structures are visible in the aqueous mass boundary layer (the

fraction of the mass boundary layer is visualized by the fluorescent areas). The depth of the neutral layer z_{nl} is varying from 0.16 up to 0.31 mm. Since no gradient in the fluorescent brightness profile is visible, binary ammonia concentration profiles as stated in sec. 3.2 can be assumed.

Fig. 4.21c shows first undulations of the water surface. The image was recorded at a relatively low wind speed with a friction velocity of 3.74 cm/s. The range of the wave height fluctuations are about 0.05 mm. At this wind speed turbulent structures are revealed. The main characteristics of the structures are low frequency and relatively large spatial scales. With these turbulent processes, surface water with high ammonia concentration is transported from the water surface to the depth and outside of the neutral layer depth.

Fig. 4.21d - 4.22c show examples of the time-depth for increasing wind speeds. Waves with a small amplitude are observed. Due to surface tension the capillary waves are produced and they try to restore the equilibrium sate (Kinsman, 1965). The maximum surface elevation is varying for different friction velocities in the range from 0.06 mm for 4.51 cm/s up to 0.13 mm for 6.41 cm/s. The thickness of the visible fluorescent layer at the water surface is much larger at low wind speeds.

As one can see in figures 4.21 and 4.22, events of detachment of the fluorescent pattern from the water surface occur frequently at the higher wind speeds. The structures are taken towards the water bulk by the turbulent eddies. Therefore, for the higher wind speeds the fluorescent patterns can be found at large depth, as the spatial scale of the eddies is larger.

4.3.2. Statistical Analysis

The *t-z* images for different wind speeds were analysed to estimate the number of detachment events appearing per second as described in sec. 4.2.4. For each wind speed, time sequences of 2.73 min were evaluated. The ammonia concentration in the air space was kept at 14 ppm for all measurement runs. For the low wind speeds with friction velocities of 2.46 and 3.13 cm/s, there are no detachment events. For higher wind speed values, the number of detachment events increases up to around 7 events per second (see fig. 4.23a).

As one can see in fig. 4.23a, the number of detachment events increases greatly around a friction velocity of 6 cm/s. This sudden rise in the number of detachment events can be explained by considering the surface renewal model of gas exchange (see sec. 2.1.4) with the renewal rate λ:

$$\lambda = \gamma_p z^p \tag{4.16}$$

The transition from renewal rate with $p = 1$ with boundary conditions at rigid interface to $p = 0$ at free interface embraces the increase of renewal events. Therefore, at low wind speeds in case of a flat water surface and a low renewal rate, the boundary conditions are similar to a rigid interface. At higher wind speeds, in case of a wavy water surface and more renewal events, the boundary conditions are more similar to a free interface. A similar conclusion was made by Friedl (2013), Falkenroth (2007) and Münsterer and Jähne (1998).

Fig. 4.23b shows distributions of the neutral layer depth z_{nl}, estimated as described in sec. 4.2.4, for the three highest wind speeds used during the experiments. Below the neutral layer depth, the

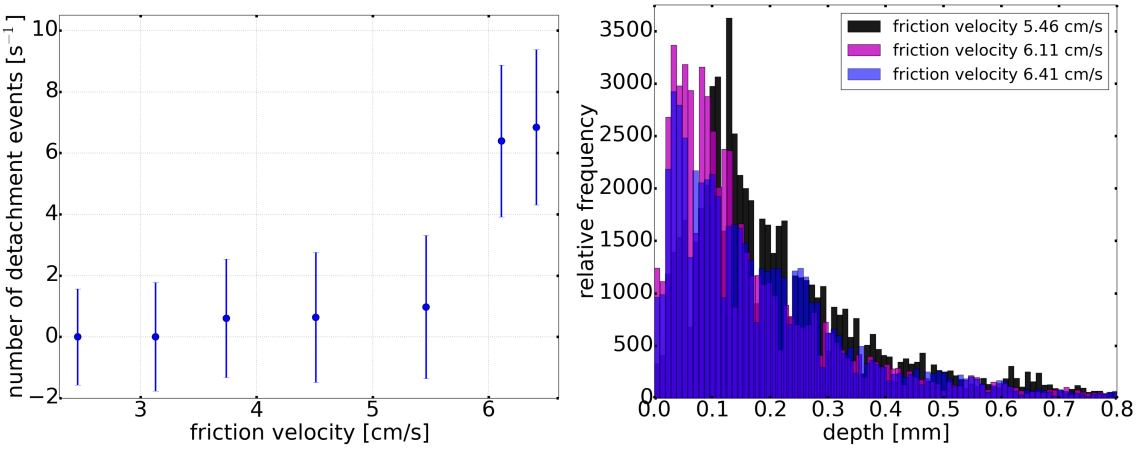

Figure 4.23.: (a) Number of detachment events in dependence of the observed wind speed as a function of the friction velocity. The sudden increase of surface renewal events is around friction velocity of about 6 cm/s. (b) Histograms of the mass boundary layer thickness distribution at different depths for increasing wind speeds (friction velocity from 5.46 to 6.41 cm/s).

fluorescent structures are not visible as the water bulk is sufficiently acid. With increasing wind speed, i.e. friction velocity, more turbulent eddies are present and transporting the fluorescent surface water down to the water bulk. Hence, the fluorescent layer close to the water surface is thinner and less fluorescent. Therefore, the maximum of the distributions of the neutral layer depth is shifting to lower z_{nl} values. It complies with the results by Ward (2007) and Krah (2014) concerning the change of the mass boundary layer thickness with different wind conditions.

The space scales of the turbulent structures were estimated in dependence of the depth coordinate. The turbulent eddies come closer to the air-water interface at higher wind speed. At the highest wind speed used in experiments the eddies can be found at a distance of 0.1 mm from the water surface. For the low wind speed the closest position of the eddies is 0.3 mm. The depth, the turbulent structures get transported to, increases with the wind speed - for high friction velocity of 6.41 cm/s, the fluorescence can be found at a distance of 11.2 mm from the water surface.

4.3.3. Analysis of the BLV Technique

The section presents the analysis of the brightness profiles from the experimental sets I and II to verify the BLV technique. The shapes of the profiles with different conditions during the experiments were examined and compared to simulated profiles.

I Ammonia concentration:

The first set of the experiments with different ammonia concentrations was performed to examine the dependency of the concentration profiles on the amount of ammonia in the air side. The profiles were simulated as described in sec. 4.1.2 and the results can be found in fig. 4.3c. Therefore one can expect a linear growth of the neutral layer depth with increasing the ammonia concentration.

The experimental data were preselected from set I. Data for seven different ammonia concen-

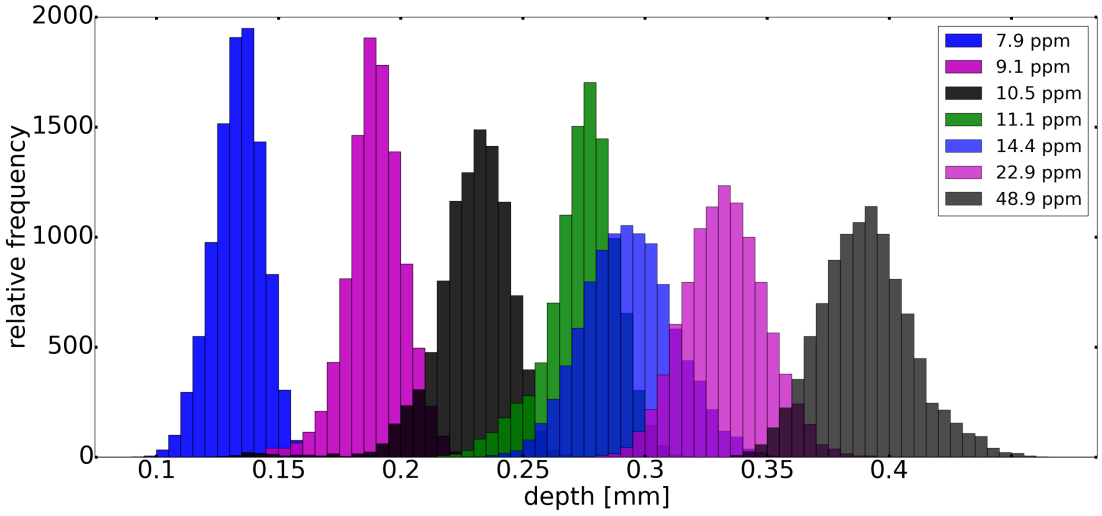

Figure 4.24.: The probability density function of the neutral layer depth for different ammonia concentration. The statistics was calculated for time-depth sequences of 2.73 min. The spread of the distribution for higher ammonia concentrations is due to the fast change of the conditions in the facility within the recorded time.

trations from 8 to 50 ppm were evaluated. Only data from equilibrium conditions (ammonia influx into air space equals to air-water flux) were processed. For each frame of recorded images the neutral layer depth was estimated as described in sec. 4.2.4. The probability density functions of the neutral layer depth for different ammonia concentrations were calculated and are presented in the form of histograms in fig. 4.24. The statistics of the neutral layer depth was collected during 2.73 min over 65535 frames for each ammonia flux.

One should note that, as the data were recorded with identical turbine frequency, higher ammonia concentrations were gained with higher ammonia fluxes. For ammonia concentrations in the air side of 14, 23 and 49 ppm, the probability density functions include higher variability of the neutral layer depth (seen as spreaded probability density functions in fig. 4.24). This is explained by a significant change in the ammonia concentrations during the acquisition time. There is to say, the equilibrium of ammonia in the air side was not reached as it takes longer time and the whole water in the facility starts to fluorescence at too high concentrations.

For that reason only the data from the first four ammonia concentrations with low flux rates were selected for further evaluation. The mean concentration profiles for that data are presented in fig. 4.25a. In order to reduce the variance in neutral layer depth due to a change in ammonia concentration, the averaging was performed over 25 sec. The profiles were normalized by the maximum brightness value at the water surface. The dependency of the estimated neutral layer depth over the air-sided ammonia concentration is presented in fig. 4.25b.

The linear fit in fig. 4.25b is in good correspondence with the estimated neutral layer depth. Moreover, the intersection of the linear fit with the x-coordinate provides the value of ammonia concentration at which the fluorescence starts to be seen. This concentration corresponds to the transition from eq. (3.17), when all H_3O^+ ions are consumed by the ammonia molecules. Schematically it can be seen in the left and right side of fig. 3.5.

The value of margin ammonia concentration is found to be 6.05 ppm, which complies with the

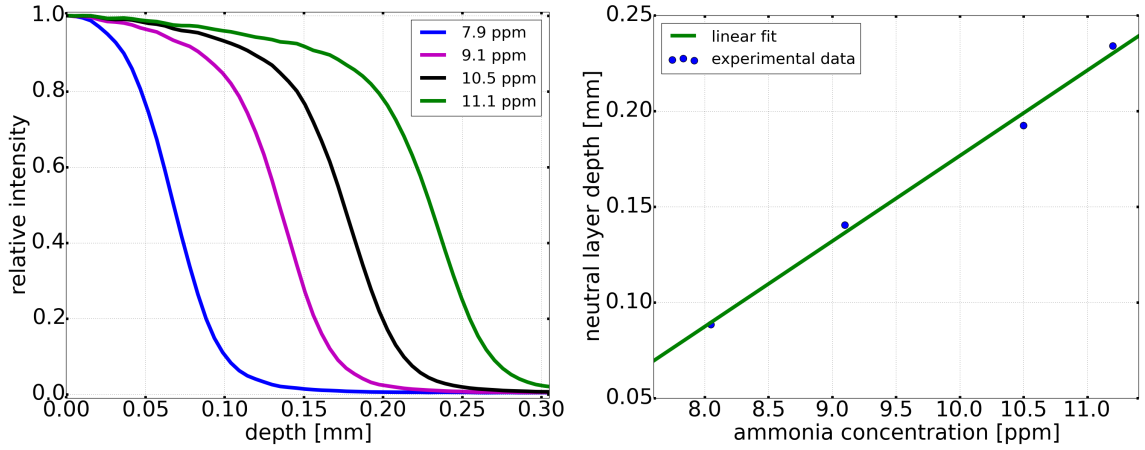

Figure 4.25.: (a) The mean experimental profiles for low ammonia concentration in the air side. The profiles were averages over 25 sec. For different ammonia concentrations, the drop in the brightness profile occurs at different depth from the water surface. (b) The dependency of estimated neutral layer depth on the air-sided ammonia concentration that agrees with the linear fit.

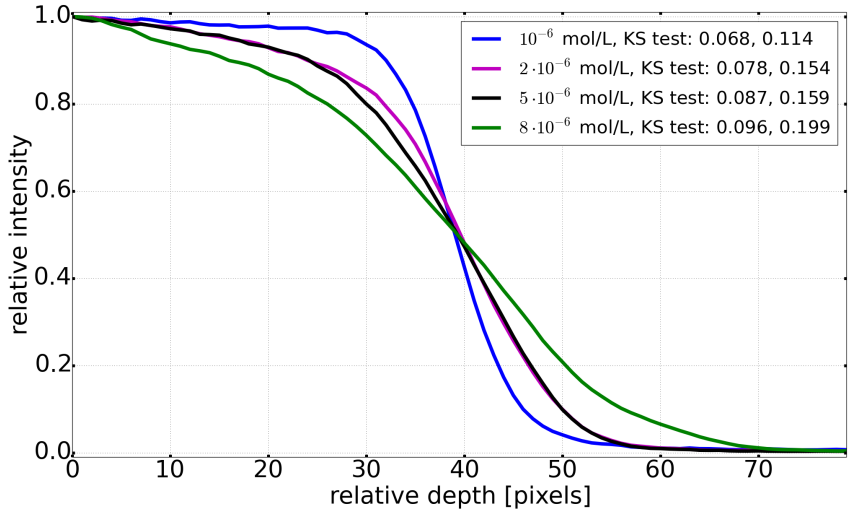

Figure 4.26.: The mean brightness profiles for different Pyranine concentrations in water. The profiles are averages over 25 sec. The slopes of the profiles are found to be steeper for lower concentrations of Pyranine.

ammonia concentration noted during the experiments.

II Pyranine concentration:

The evaluation of the BLV technique with different Pyranine concentrations was performed on data from the set II. Mean concentration profiles for identical conditions but Pyranine concentrations varying from 10^{-6} up to $8{\cdot}10^{-6}$ mol/L are shown in fig. 4.26. Higher values of Pyranine were recorded as well but were hard to compare with the profiles of low Pyranine concentrations. The experiments with higher Pyranine concentrations required lower initial pH values to avoid the saturation regime. Different pH values have an additional effect on the steepness of the brightness profile as shown by the simulations in sec. 4.1.

Due slightly different conditions during the experiments (mostly different ammonia concentra-

tions), the profiles comprise the sudden drop in the intensity at various distances from the water surface. To eliminate this issue, the depth of half from the maximum intensity of each profile was set to the same point as it is seen in fig. 4.26.

The estimation of the profile steepness was performed by Kolmogorov-Smirnov statistics (Bohm and Zech, 2010). The Kolmogorov-Smirnov test (KS test) is a nonparametric statistical test for comparing the empirical distribution function with the cumulative distribution function of the reference distribution. For comparing the mean brightness profile with a step-shaped profile, the empirical cumulative function of the experimental data was compared with the cumulative distribution function of a uniform distribution. The value of the KS test statistics quantifies the distance between the experimental profile and step function. For different Pyranine concentrations, the values of the KS test statistics are shown in fig. 4.26 for the left and right tails of the profiles. The lowest values of the KS test, i.e. closest to a step-shaped profile, are noted for the lowest Pyranine concentration of 10^{-6} mol/L.

4.3.4. Fit of the Models to the Data

The section gives a quantitative analysis of how well the surface renewal and small eddy models describe the data. The fitting of the experimental concentration profiles from sets I and III to the gas exchange models from sec. 2.1.4 was also performed in order to estimate the concentration of ammonia at the water surface and the mass boundary layer thickness.

The brightness profile $b(z)$ can be written as a function P of the concentration profile of ammonia with the scaling parameter C (see sec. 4.1):

$$b(z) = C \cdot P(c(z)) \tag{4.17}$$

As the mean concentration profile over depth depends on the concentration of ammonia at the water surface c_s and the mass boundary layer thickness δ_{mbl}, the mean brightness profile is a function of the depth coordinate with three parameters - C, c_s and δ_{mbl}. The straightforward fitting of the mean brightness profiles to the function from eq. (4.17) for different models of $c(z)$ leads to overfitting with an accurate alignment of the data to the simulated profiles but unreasonable values for the ammonia concentration at the water surface and the mass boundary layer thickness.

In order to prevent overfitting, the scaling parameter C was discarded by normalizing the simulated profiles to the brightness value at the water surface. The experimental data are then fitted to a profile $b_{norm}(z)$:

$$b_{norm}(z) = P(c(z))/P(c_s) \tag{4.18}$$

This step is feasible as the ammonia concentration at the water surface influences only the neutral layer depth and does not have an impact on the shape of the brightness profile.

I Ammonia concentration:

The four measured mean profiles selected from the data set I were fitted to the brightness profiles according to eq. 4.18 for the surface renewal and small eddy models at free and rigid interfaces. To

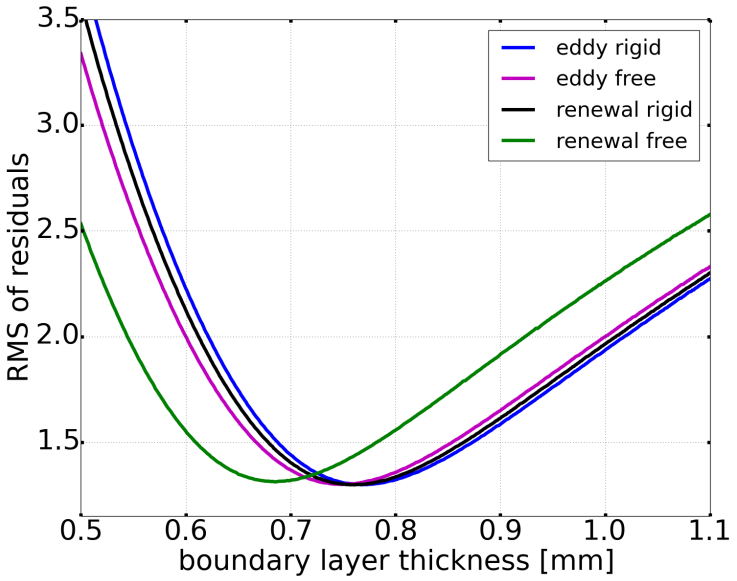

Figure 4.27.: The root mean square of the residuals for the small eddy and surface renewal models at rigid and free interfaces for various values of the mass boundary layer thickness. The minimum of the functions for the models at a rigid interface comply well. This provides an estimate of the mass boundary layer thickness of 0.76 mm.

prevent the overfitting, it was assumed that the mass boundary layer thickness is constant within the considered subset as the data were recorded at identical conditions (turbine frequency of 5 Hz). Therefore the cross validation for parameter tuning was performed for different models with varying the thickness of the mass boundary layer by 0.1 μm. Fig. 4.27 presents the quadratic mean of the residuals of the fitting for the considered models. The minimum of the curves comply well for the surface renewal and small eddy model at a rigid interface and mass boundary layer thickness was found to be 0.76 mm.

Observing the change in air-sided concentrations of ammonia, measured by differential optical absorption spectroscopy (DOAS), integrated transfer velocities can be found by fitting the concentration values to an exponential function (Kräuter, 2011a). With known ratio of the air to water-side transfer velocity (Liss and Slater, 1974), the estimation of mass boundary layer thickness is possible. For the current set, the value of 0.8 mm was calculated. The details can be found in appendix A.

With the known thickness of the mass boundary layer δ_{mbl}, the data can be fitted to the brightness profile as a function of the depth coordinate with one parameter - ammonia concentration at the water surface c_s. The results of the performed fitting are shown in fig. 4.28. The best fit is observed for the models at a rigid interface, that characterizes the case of a flat water surface.

The estimated concentrations of ammonia at the water surface for the four profiles are $3.39{\cdot}10^{-5}$, $3.77{\cdot}10^{-5}$, $4.04{\cdot}10^{-5}$ and $4.44{\cdot}10^{-5}$ mol/L. Worth mentioning here is that the estimated values are identical with the accuracy to two decimal places for the small eddy model and surface renewal models at a rigid interface.

The critical part of the fitting routine is to find appropriate values for the initial conditions at the facility, such as the concentration of $\mathrm{IH}_{\mathrm{tot}}$ and, most importantly, the initial pH value, defined

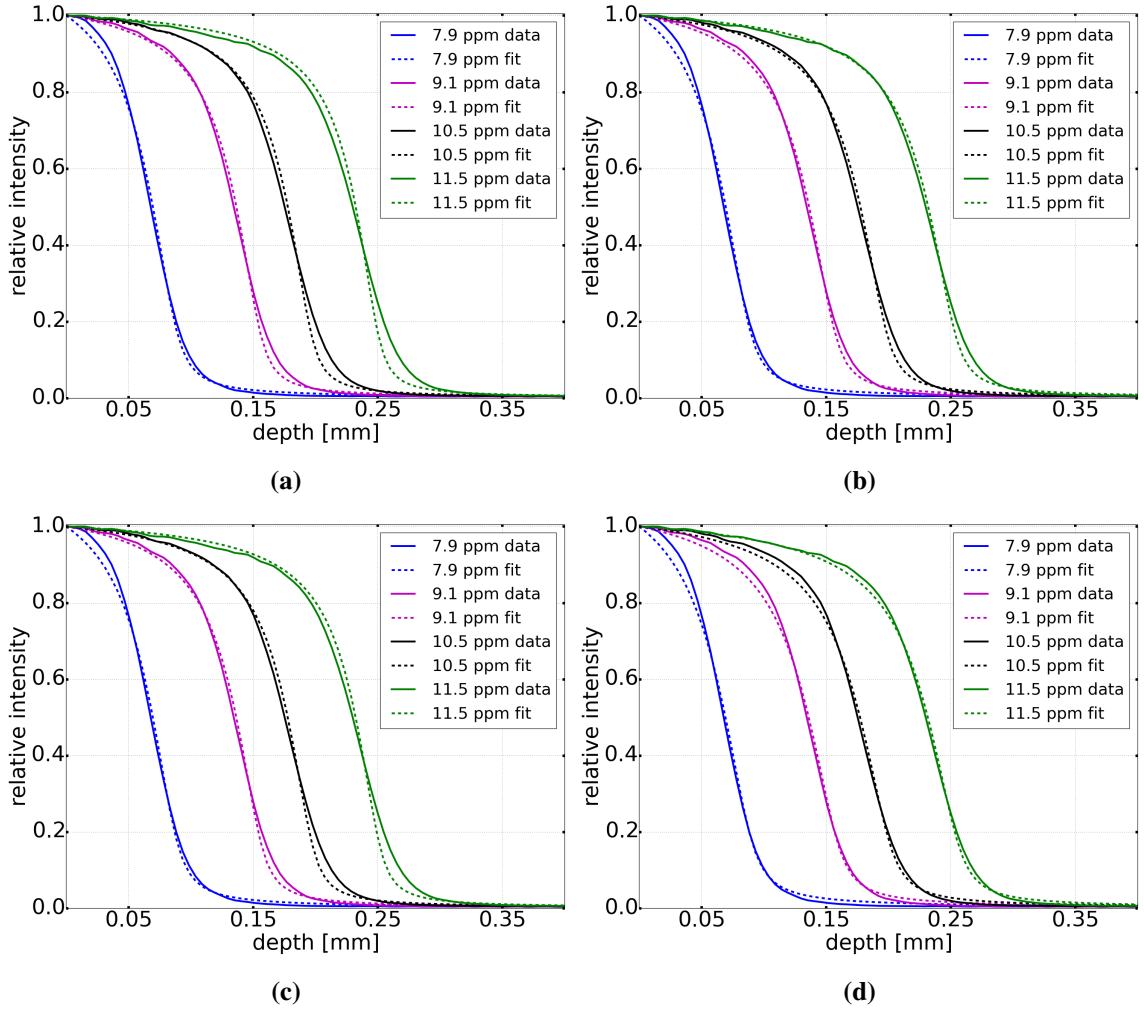

Figure 4.28.: The mean brightness profiles for different ammonia concentration in the air side fitted to (a) small eddy model at rigid interface, (b) small eddy model at free interface, (c) surface renewal model at rigid interface and (d) surface renewal model at free interface. The best fit corresponds to the models at rigid interface.

by the concentration of HCl. It is of importance as the shape of the simulated profiles directly depends on the fitting procedure. The appropriate guess of ammonia concentration was estimated by knowing that at least 10^{-4} mol/L of ammonia is needed for the fluorescence to start if the initial pH value is 4.

III Wind speed:

The main objective of evaluating the set III was to estimate the mass boundary layer thickness for different wind conditions. As one can see in fig. 4.3d, an increase in the mass boundary layer thickness shifts the profile over the depth direction towards the water bulk without any changes in the shape of the profile. Therefore, one can estimate the δ_{mbl} value from the mean brightness profile for different wind speeds.

The fitting for the next turbine frequency of 6 Hz, i.e. a friction velocity of 3.13 cm/s, was performed on the data collected from 4 separate experiments. The averaging of the recorded profiles was maintained over 2.73 min. The acquisition of data started after the ammonia in the air

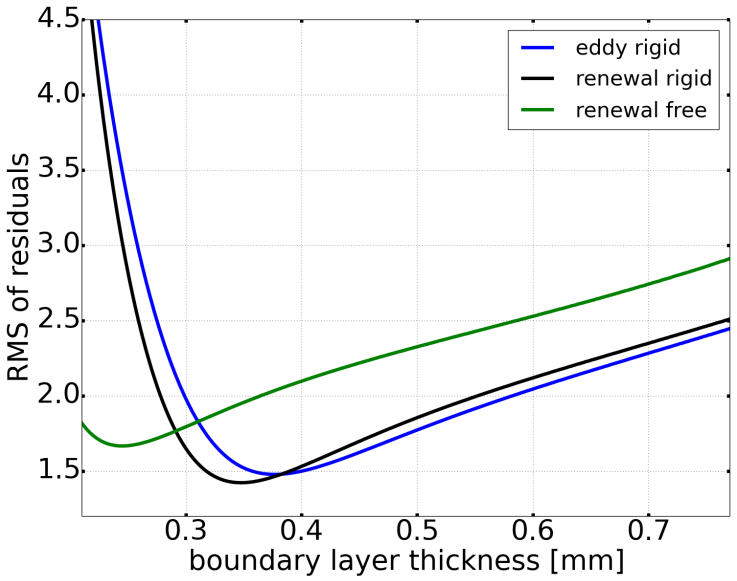

Figure 4.29.: The root mean square of the residuals for the small eddy and surface renewal models at rigid and free interfaces for various values of the mass boundary layer thickness. The minimum of the functions for the models at a rigid interface comply well. This provides an estimate of the mass boundary layer thickness of 0.36 mm.

side has approximately reached an equilibrium. The same procedure of cross validation as for the set I was performed in order to estimate the mass boundary layer thickness. The curves of the root mean square residuals for fitting the mean data for different models are presented in fig. 4.29.

The turbine frequency of 6 Hz maintains the condition of a flat water surface, therefore the surface renewal and small eddy models at a rigid interface retain the lower root mean square values of the fitting residuals. The minima of the curves are found at 0.35 and 0.38 mm for surface renewal and small eddy model, respectively. The small eddy model at a free interface does not describe the data well as the error of the fitting is much higher than for the models with boundary conditions for a rigid interface. Therefore, the curve of the root mean square of the residuals for the small eddy model at a free interface was discarded from fig. 4.29.

The fitting of the experimental data from the set III for higher wind speed values assembled additional difficulties. Higher wind speed values complicate the procedure of fitting as the time needed for ammonia to reach equilibrium was sufficient to change the conditions in the water, most importantly the pH value that directly influences the shape of the function P. To guess the change of local pH value was impossible as it was not monitored during the experiments.

Moreover, the procedure of cross validation for estimation of the mass boundary layer thickness was not feasible as the data for a certain wind speed was hard to record at a constant air-side concentration of ammonia. Additionally, with more ammonia penetrating through the air-water interface, the pH value near the water surface changes, that decreases the solubility of ammonia. This implies variability of ammonia concentration at the water surface with similar air-sided ammonia concentrations. Therefore the fitting includes two free parameters - c_s and δ_{mbl}. As one can see in fig. 4.3c and fig. 4.3d, the ammonia concentration at the water surface and the value of the mass boundary layer thickness have a similar impact on the profile. Thus, the fitting of the data to

the models for higher wind speed values induces overfitting with infeasible estimated values for the thickness of mass boundary layer.

5. Visualization Measurements with Trifocal Set-up

This chapter covers the measurements conducted at the Aeolotron, an annular wind-wave facility at the Institute of Environmental Physics at the University of Heidelberg. Sec. 5.1 presents the description of the experimental set-up, calibration procedure and the performance of the measurements. The data processing steps including full calibration of the cameras, image rectification and disparity map computation are summarized in sec. 5.2. The chapter ends with the results of the visualization measurements.

5.1. Aeolotron Measurements

The experiments at the Aeolotron have been conducted with the BLV technique (see sec. 3.2) to visualize the mass boundary layer and analyse the turbulent mechanisms in three dimensions. Three cameras observed the fluorescent structures, which are due to ammonia penetrating through the air-water interface. Three projections were necessary to reconstruct the binary representation of the concentration fields.

5.1.1. Experimental Set-up

Large annual facility

The experiments were conducted at the large annual wind-wave facility Aeolotron (for detailed description of the facility see Krall (2013) and Kräuter (2015)). The schematic top view of the tank is shown in fig. 5.1. The Aeolotron has a ring shaped water flume with an inner diameter of 9 m and a width of 0.6 m. With an average water level of 1 m, the air and water volumes are 25000 L and 18000 L, respectively. Two turbines mounted at the ceiling of the tank at segments 4 and 12 are generating wind with a maximum reference wind speed of 12 m/s. The facility is chemically resistant, thermally isolated and air tight providing a low leakage rate. The air-conditioning (AC) system installed at the sections 9 and 11 dehumidifies the air to allow infrared imaging of the heat flux with the air side of the facility being closed.

The trifocal set-up for the visualization of the mass boundary layer is installed at segment 13. The sketch of the experimental set-up is shown in fig. 5.2a. At this section the light sources suitable for the visualization technique were mounted beforehand along the work done by Kräuter (2015). The cameras are placed underneath the facility with a slight shift towards segment 14. The spectrometer set-up is mounted at segment 15.

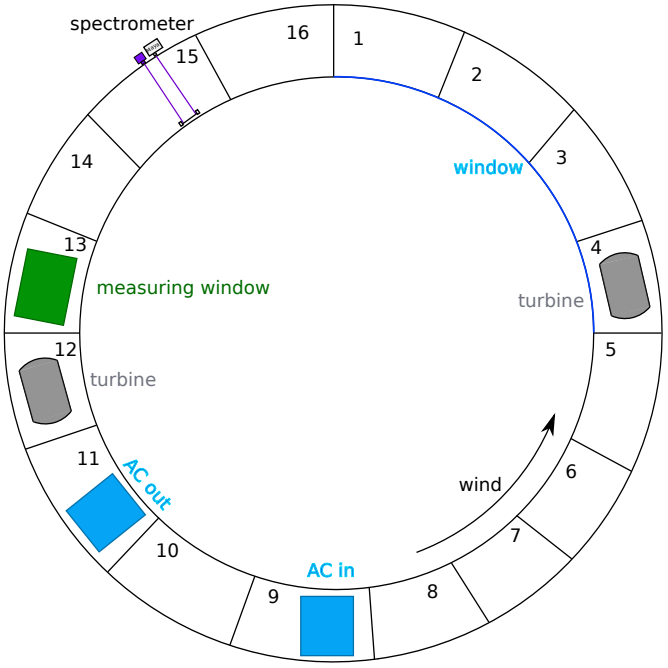

Figure 5.1.: Schematic view from the top of the Aeolotron facility with the wind generated turbines at segments 4 and 12, air conditioning inlet and outlet at segments 9 and 11, respectively, spectrometer set-up at segment 15 and the measuring window at the segment 13.

Additionally, an infrared camera Velox 327k M by IRcam for the visualization of the heat flux is installed in an inclined position in the roof of segment 13. The infrared camera and the set of three cameras in the visible range are capturing the same patch of the water surface. An imaging slope gauge (ISG) is installed at segment 13 that allows to measure the wave slope (for more details see Kiefhaber et al. (2014)). Temperature sensors (Pt-100) in the air and water, humidity sensors, a conductivity sensor, a pH sensor, an anemometer and a pitot tube in the air and an acoustic Doppler anemometer in the water are also installed at the Aeolotron.

Light source

As a relatively large area of the water surface needs to be illuminated, the usage of the laser as a light source is no longer practical. Therefore, it is favorable to select LEDs as a light source. As the Pyranine molecules in an alkaline solution are excited at the wavelength of 455 nm, blue high power LEDs are used. Osram *OSLON SSL* LEDs with the peak at a wavelength of 463 nm are chosen. The operation of the LEDs is possible with the maximum current of 2 A in a pulsed mode.

To increase the signal-to-noise ratio, 14 light sources with 18 LEDs each are installed above the glass window on the top of the facility. As the LEDs are mounted at a distance of 1.4 m from the water surface, the light needs to be focused. For this reason, *Carclo* lenses are mounted on each LED, that enhanced the intensity of emitted light by a factor of approximately 38 (Kräuter, 2015).

The broad spectrum of the LEDs enhances the probability of exciting the Pyranine molecules in the acid solution as well as in the alkaline solution. Hence, additional filtering, restricting the wavelength range of emitted light, is required. New custom made bandpass filters Delta, BP

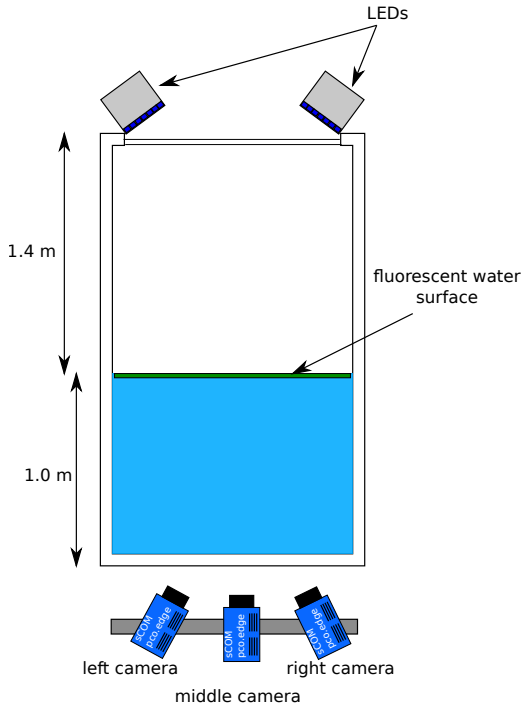

(a)

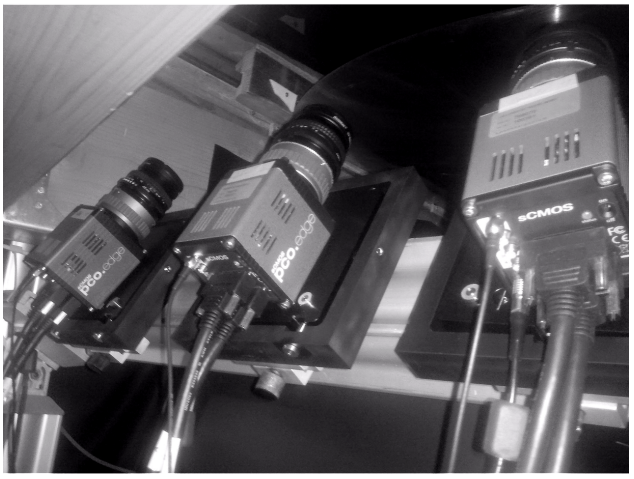

(b)

Figure 5.2.: (a) Sketch of the experimental set-up in a side view. LEDs are mounted on top of the ceiling glass window of the facility. Three cameras are placed on a horizontal bar underneath the facility at a distance of 48 cm between the left and right camera. The cameras are focused on the water surface to capture the fluorescent patch. (b) Photo of the three cameras illustrating the tilt necessary for capturing the LED illuminated patch at the water surface.

(470×35 nm) are mounted on each LED to suppress the undesirable excitation of Pyranine at low pH values.

Cameras

To capture the fluorescent light scene, scientific CMOS cameras are placed at the measuring section underneath the facility at a distance of 35 cm from the bottom of the tank. Due to limited space available, the number of the cameras is set to three. A photo of the cameras mounted at the Aeolotron is shown in fig. 5.2b. A vertical orientation of the cameras is not possible as the ISG light source is mounted at segment 13 underneath the bottom of the facility as well. Therefore, the cameras are shifted towards segment 14 by roughly 50 cm and tilted in such a way that they observe the illuminated patch of the water surface. Additionally, the side cameras are tilted along the axis of a stereo base, providing the view at different angles. The length of the stereo base is about 48 cm.

The scientific CMOS camera enables high-speed, high-resolution and low-noise measurements. At a full image resolution of 2160×2560 and in the rolling shutter mode, the maximum frame rate is 100 Hz. The pixel size is $6.5 \times 6.5\,\mu m^2$. As only the fraction of the mass boundary layer is fluorescent, the fluorescent signal is very low. Therefore, the low-noise cameras are of necessity for the experiments. The sCMOS cameras have a non-uniform dark signal and photo response of less than 0.3 e^- rms and 0.2 %, respectively.

Minolta Rokkor-x objectives are mounted on the cameras for focusing on the water surface. The focal length and the aperture range of the objectives are 45 mm and f/2-16, respectively. The aperture size was manually set to 2.8 in order to provide higher signal-to-noise ratio. Additionally, bandpass filters by Edmund Optics BP (525×45 nm) are mounted in front of the camera objectives to suspend blue light from LEDs.

The *PCO.edge* camera has a pixel bit depth of 16 bit (the gray value from 0 to 65535). With full image resolution and continuous image acquisition, the saving of such amount of data is challenging. Therefore, the compression of the data to 8 bit data format is implemented by the use of gain compression (Jähne, 2013). The gray values of the image are transformed non-linearly in the following way:

$$c(x,y) = \sqrt{\text{gain} \cdot (g(x,y) - \text{offset})} \tag{5.1}$$

where $c(x,y)$ is a output saved image, $g(x,y)$ is the raw image from the camera, and gain and offset are user selectable values.

With the compression to 8 bit, the data are saved continuously to the computer hard disks with image resolution of 1840×2240.

Spectrometer Set-up

In order to monitor the concentration of ammonia in the air side of the Aeolotron, a custom made UV spectrometer is mounted at segment 15. The spectrometer set-up is similar to the set-up used at the linear wind-wave facility (see sec. 4.2.1). The detailed description of the used spectrometer and the geometry of the light beam path are given in Kräuter (2015).

5.1.2. Calibration

The recorded images from three cameras need to be corrected for the fixed pattern noise, undesirable fluorescence from the water bulk and inhomogeneous LED illumination.

Dark and bulk water corrections

For each camera, the dark images were recorded in order to minimize image noise by dark-frame subtraction. Additionally, to correct for the fluorescent light due to fluorescence from the acid bulk, images with turned on LEDs and no tracer gas in the air side of the facility were acquired. Those images are further referred as zero images. Zero images were taken with the camera settings, exposure time and frame rate as during the experiments. Examples of dark and zero images for the right camera are presented in fig. 5.3a and fig. 5.3b, respectively. To additionally reduce the fluorescent light from the acid bulk water, the absorbing dye Tartrazine was added to the water prior to the experiments (for more details see Kräuter (2015)).

Correction for LED illumination

As the LED illumination of the water surface patch is not homogeneous, a correction of the images for the distribution of the LED light is required. To record calibration images for the LED correction, two borofloat glass plates were used. They were placed on a distance of 2.5 mm and

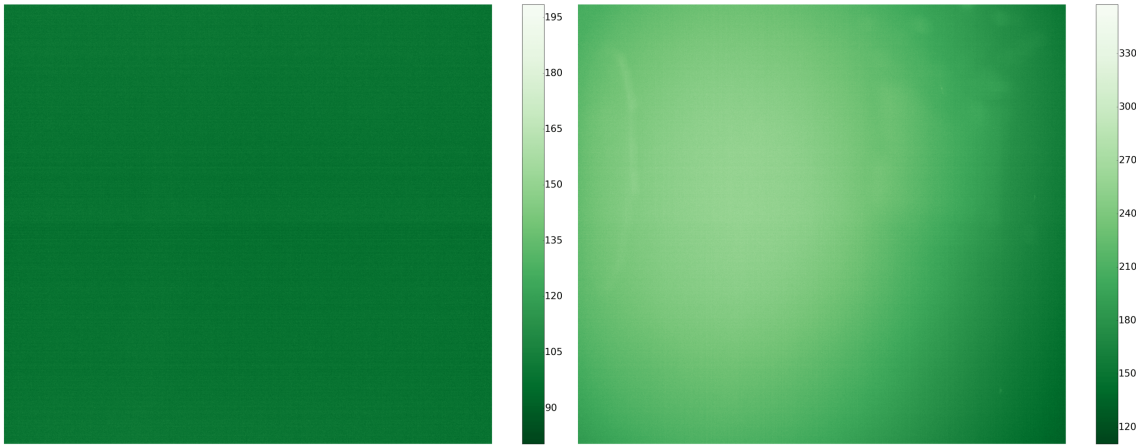

(a) **(b)**

Figure 5.3.: (a) Averaged dark image (1500 images) recorded with a closed lens. The acquisition time was similar as during the experiments. (b) Zero image showing the signal from the water bulk with visible pattern of non-homogeneous LED illumination. The non-linear transformation due to data compression was applied to both images.

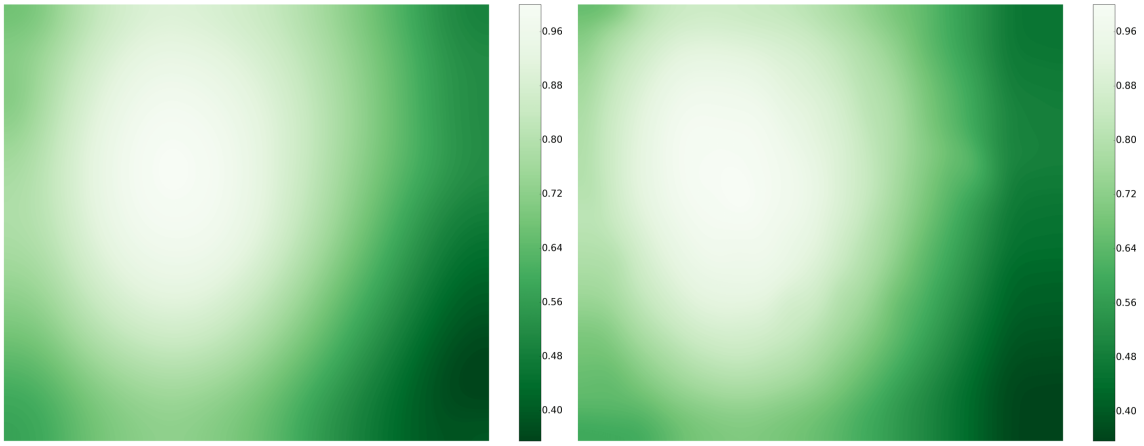

(a) **(b)**

Figure 5.4.: Normalized brightness images from (a) the left and (b) right camera. The images were taken with an equally distributed Pyranine solution at a high pH value. The solution was injected in the prepared horizontal plates. The non-linear transformation due to data compression and normalization were applied to both images.

closed from all sides. The space in between the plates was filled with an alkaline solution with premixed Pyranine. The images were recorded with integration time of 10 ms in order to gain a high fluorescent signal. Further, those images are referred as brightness images. An examples of the LED brightness images from left and right cameras are shown in fig. 5.4.

Cameras calibration

As the images from the three cameras are used further in stereo algorithm, a full calibration of the three cameras, i.e. estimation of the position and orientation of each camera, is required. For that purpose the checkerboard with 18×23 chequered $1\times1\,\mathrm{cm}^2$ patterns was used as a calibration target. It was placed in the water close to the interface at different positions. In order to get a good

calibration, the checkerboard was moved around so the checkerboard is filling the whole field of view of all three cameras. Additionally, the checkerboard was tilted to the left, right, top and bottom to provide non symmetric images of the chequered patterns. The checkerboard was also placed underneath the water surface at different tilting angles. An examples of the images with the checkerboard at a certain position from the left and right cameras are shown in fig. 5.5a and 5.5b. Altogether 40 images of the checkerboard at different positions were recorded.

In order to estimate the camera matrices, the chequered pattern needs to be determined. It was performed using *cv2.findChessboardCorners()* function of *OpenCV* package in *iPython*. Examples of the found checkeboard corners in the images are presented in fig. 5.5c and 5.5d. Having a sufficient number of images, the camera matrices are found using *cv2.calibrateCamera* function that performs the calibration of a single camera. For the left and right camera, the camera matrices are:

$$\begin{aligned} \Lambda_{\text{left}} &= \begin{bmatrix} 8.8 \cdot 10^3 & 0 & 7.1 \cdot 10^2 \\ 0 & 9.4 \cdot 10^3 & 2.5 \cdot 10^3 \\ 0 & 0 & 1 \end{bmatrix} \\ \Lambda_{\text{right}} &= \begin{bmatrix} 8.9 \cdot 10^3 & 0 & 1.9 \cdot 10^3 \\ 0 & 9.4 \cdot 10^3 & 2.5 \cdot 10^3 \\ 0 & 0 & 1 \end{bmatrix} \end{aligned} \tag{5.2}$$

The estimated parameters of focal distances f_x and f_y are in pixels units. Furthermore, the distortion coefficients are found for left and right camera:

$$\begin{aligned} [k_1, k_2, k_3, p_1, p_2]_{\text{left}} &= [0.528, -4.701, 0.103, -0.029, 22.625] \\ [k_1, k_2, k_3, p_1, p_2]_{\text{right}} &= [0.588, -5.709, 0.102, 0.024, 28.143] \end{aligned} \tag{5.3}$$

The distortion coefficients are used further to undistort the images from the cameras prior to proceeding with the stereo algorithm.

Estimating the pose for each view of the checkerboard position was found using the *cv2.solvePnPRansac* function. Fig. 5.5e and 5.5f show the estimated orientation of the checkerboard in the left and right image. The rotation matrix and translation vector for the left and right cameras are:

$$\boldsymbol{\Omega} = \begin{bmatrix} 0.983 & -0.015 & 0.185 \\ 0.013 & 0.999 & 0.008 \\ -0.185 & -0.005 & 0.983 \end{bmatrix} \tag{5.4}$$

$$\boldsymbol{\tau} = \begin{bmatrix} 46.49 \\ 0.37 \\ 3.48 \end{bmatrix} \tag{5.5}$$

The estimated distances are in units of the checkerboard patterns, i.e. centimeters. The dis-

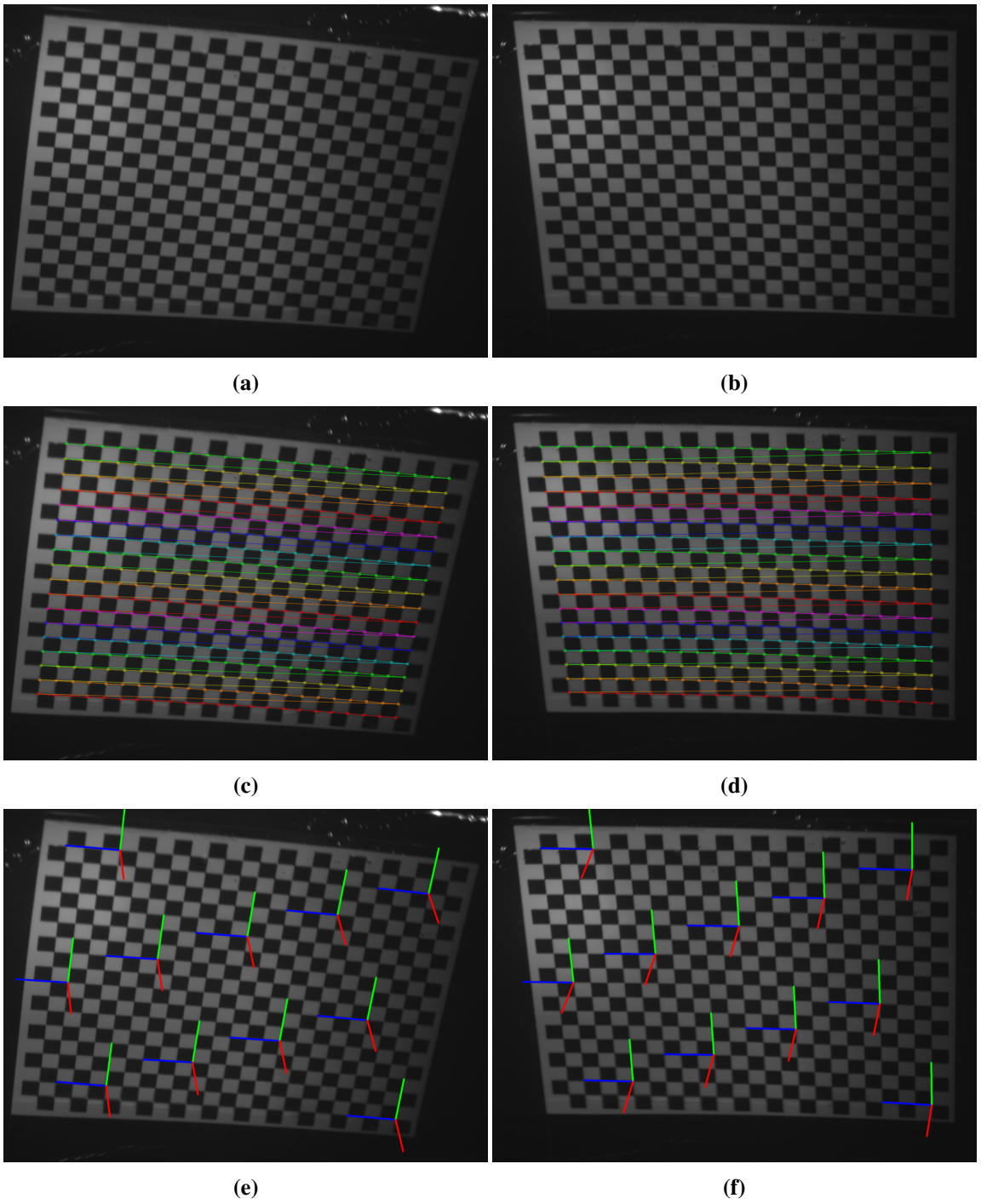

Figure 5.5.: Images of the checkerboard at a certain orientation from (a) left and (b) right camera. The images are cropped to the checkerboard edges for each image individually. The corners of the chequered patterns are found and shown in (c) and (d) for left and right camera, respectively. The pose estimation for 11 points in each image is presented in (e) and (f).

tance between the cameras are roughly equal to the length of the stereo base. Additionally, the

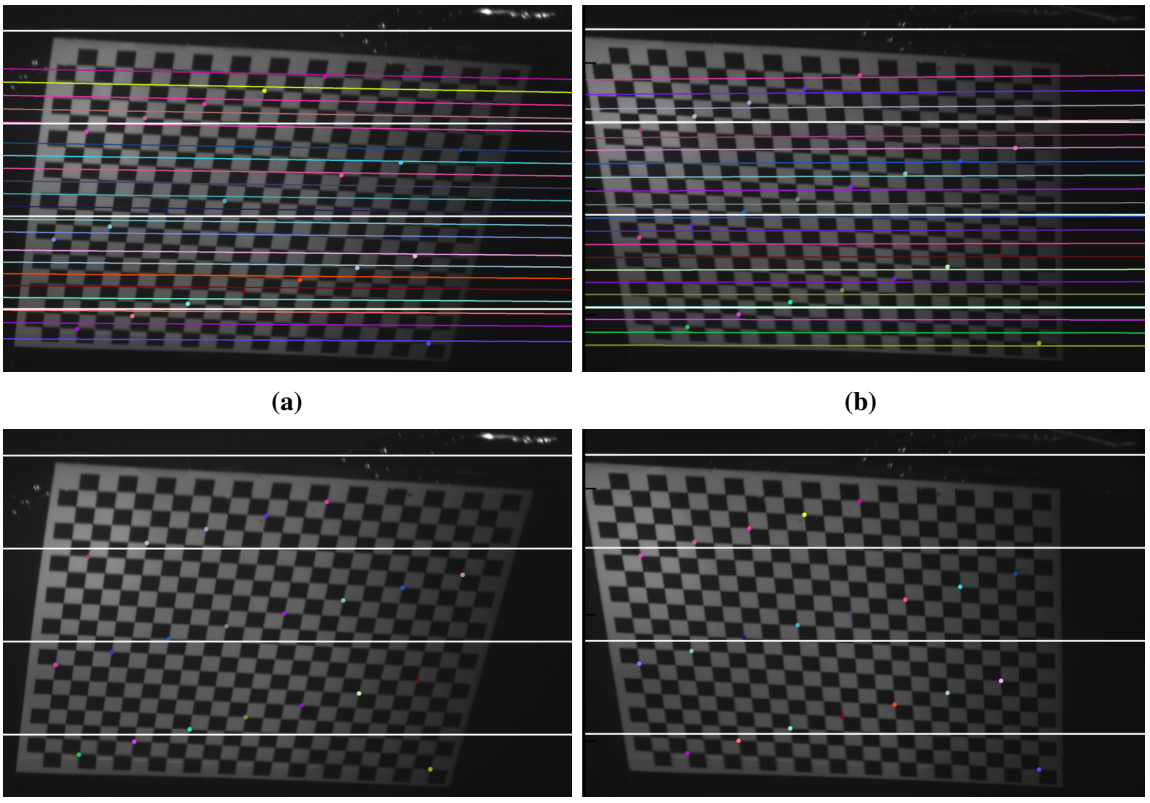

(a) **(b)**

(c) **(d)**

Figure 5.6.: The images of the checkerboard with drawn epipolar lines for (a) left and (b) right cameras. To check the rectification of the images, four arbitrary horizontal lines are shown. The lines cross the same corners of chequered patterns in both (c) left and (d) right images.

fundamental matrix was calculated using the function *cv2.stereoCalibrate*:

$$\mathbf{F} = \begin{bmatrix} -1.05 \cdot 10^{-9} & 1.50 \cdot 10^{-7} & -2.17 \cdot 10^{-4} \\ 2.25 \cdot 10^{-7} & 1.23 \cdot 10^{-8} & -1.79 \cdot -2 \\ -4.53 \cdot 10^{-4} & 1.74 \cdot 10^{-2} & 1 \end{bmatrix} \tag{5.6}$$

Rectified images of the checkerboard were analysed to check the quality of the performed calibration. For that purpose the estimated epipole lines in both images of the chekerboard were plotted in fig. 5.6a and 5.6b for left and right images, respectively. As the cameras are tilted in a small angle, the epipole lines are hardly tilted and the epipoles are not visible.

The horizontal white lines are plotted to notice the fact that they need to cross the left and right image at the exactly same positions. One can see in fig. 5.6c and 5.6d, that the lines intersect with the same chequered patterns of the checkerboard in both images.

5.1.3. Experimental Procedure

The experiments at the Aeolotron were performed with deionised water with a filling level of 1 m. Prior to the experiments, Pyranine, hydrogen chloride and Tatrazine were well mixed to the water. At first, the wind was turned on and the wave equilibrium was reached. The injection of ammonia

f [Hz]	u_{ref} [m/s]	u_* [cm/s]	T_w [°C]	T_a [°C]	λ [μS/cm]	NH_3 [mL/min]	IH_{tot} [mol/L]	IR	ISG
5	1.52	0.2	21.3	22.3	11.5	40	10^{-5}	×	×
7	2.16	0.31	21.3	22.2	11.5	50	10^{-5}	×	×
9	2.79	0.4	21.6	26.3	11	60	10^{-5}	✓	×
12	3.88	0.53	21.6	26.0	10	90	10^{-5}	✓	×
5	1.52	0.2	21.4	28.8	10	45	10^{-5}	✓	×
7	2.16	0.31	21.4	20.8	9.5	60	10^{-5}	✓	×
12	3.88	0.53	21.8	22.5	9.5	90	10^{-5}	✓	✓

Table 5.1.: Measurement conditions at the Aeolotron facility. With AC system being on, the simultaneous measurements with infrared camera are available. The ISG was running for one last measurement run only.

from a gas bottle into the air space of the facility was started. The flux of ammonia was fixed by a flux controller. Finally, with enough amount of ammonia in the air side, the measurements was initialized. In order to gain synchronized measurements with the infrared camera and the ISG, the three cameras were triggered externally by the infrared camera. The visual range cameras were working in rolling shutter mode with a frame rate of 100 Hz and an integration time of 9.9 ms. All pixels of the sensor were active after 8.8 ms. To avoid the effect of a rolling shutter, the LEDs were turned on for 1 ms with a delay of 8.8 ms. At last, the ammonia flux was turned off, the cameras were stopped.

The measurements were conducted at four different wind speeds partly with and without the air conditioning system which was necessary to conduct simultaneous heat exchange measurements. The summary of the used conditions can be found in tab. 5.1. The measurements were conducted in a low wind speed regime, since the images would have been blurred at high wave amplitudes due to the small depth of field.

5.2. Data processing

5.2.1. Preprocessing

Prior to the employment of stereo algorithms on the boundary layer visualization images, preprocessing steps are required. The scheme of the preprocessing applied on the images from each camera is presented in fig. 5.7. As the images were compressed for saving purposes (see sec. 5.1.2), the decompression needs to take place first. The averaged dark, zero and brightness images along with raw images itself were corrected for gain compression according to equation:

$$f(x,y)_{corr} = \frac{f(x,y)^2}{4} + 80 \tag{5.7}$$

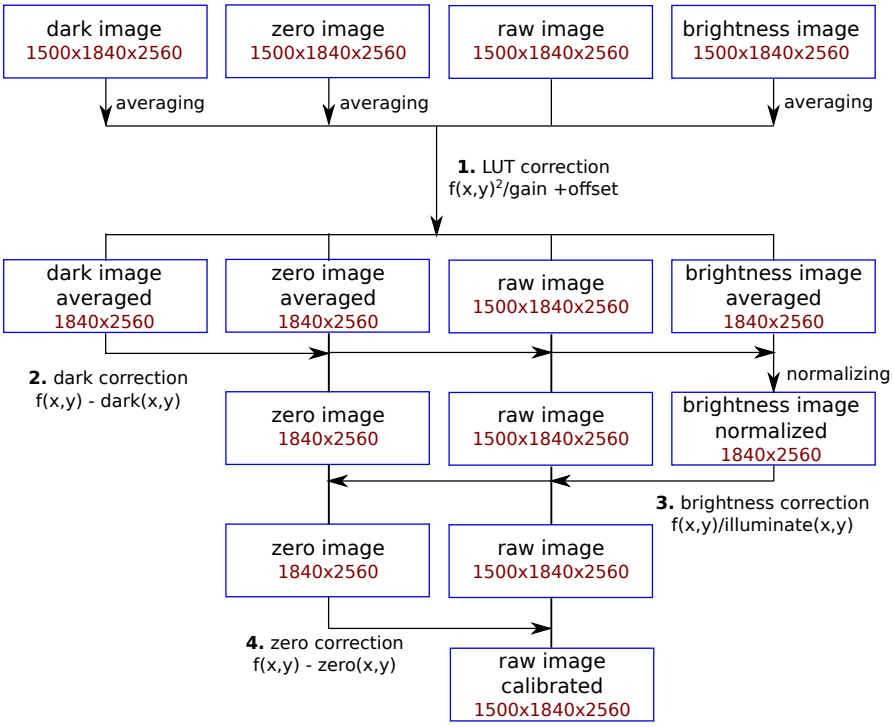

Figure 5.7.: Preprocessing steps for the images taken with the cameras. Four main steps are highlighted - LUT correction, dark image subtraction, brightness image correction and zero image subtraction.

Zero image, brightness image and each single frame of the raw image were corrected for fixed-pattern noise by subtracting the dark image (step two in fig. 5.7). Zero and raw image were also corrected for inhomogeneous LED illumination of the water surface with division to the normalized brightness image - step three. And finally, zero image was subtracted from each single frame of the raw image. Example of a single image from the right camera along preprocessing steps is shown in fig. 5.8.

Fig. 5.8a presents the image saved to the hard drive during the experiments. Fig. 5.8b shows the same image after the correction according to eq. (5.7). As one can see, the decompression brings up higher gray values and damp low gray values that make the structures of fluorescence more pronounced. The image corrected for fixed-pattern noise is discarded as no visible difference can be seen. The image corrected for LED illumination and zero image is seen in fig. 5.8c. One should note here, that the structures on the sides of the image are visualized with higher intensities as the LED light distribution on the sides of the images are reduced.

5.2.2. Image Rectification

As the images from the left and right camera are used further in stereo algorithms, they need to be rectified according to the position of each camera. It is used in computer stereo vision to simplify the problem of finding matching points between the images. At first, the rectification procedure includes un-distortion of the images. Using rotation matrices for each camera, rotation transform puts the images on the same plane, while scaling makes the image frames be the same size. Additionally, skew adjustments makes the image pixel rows directly line up. The rectification

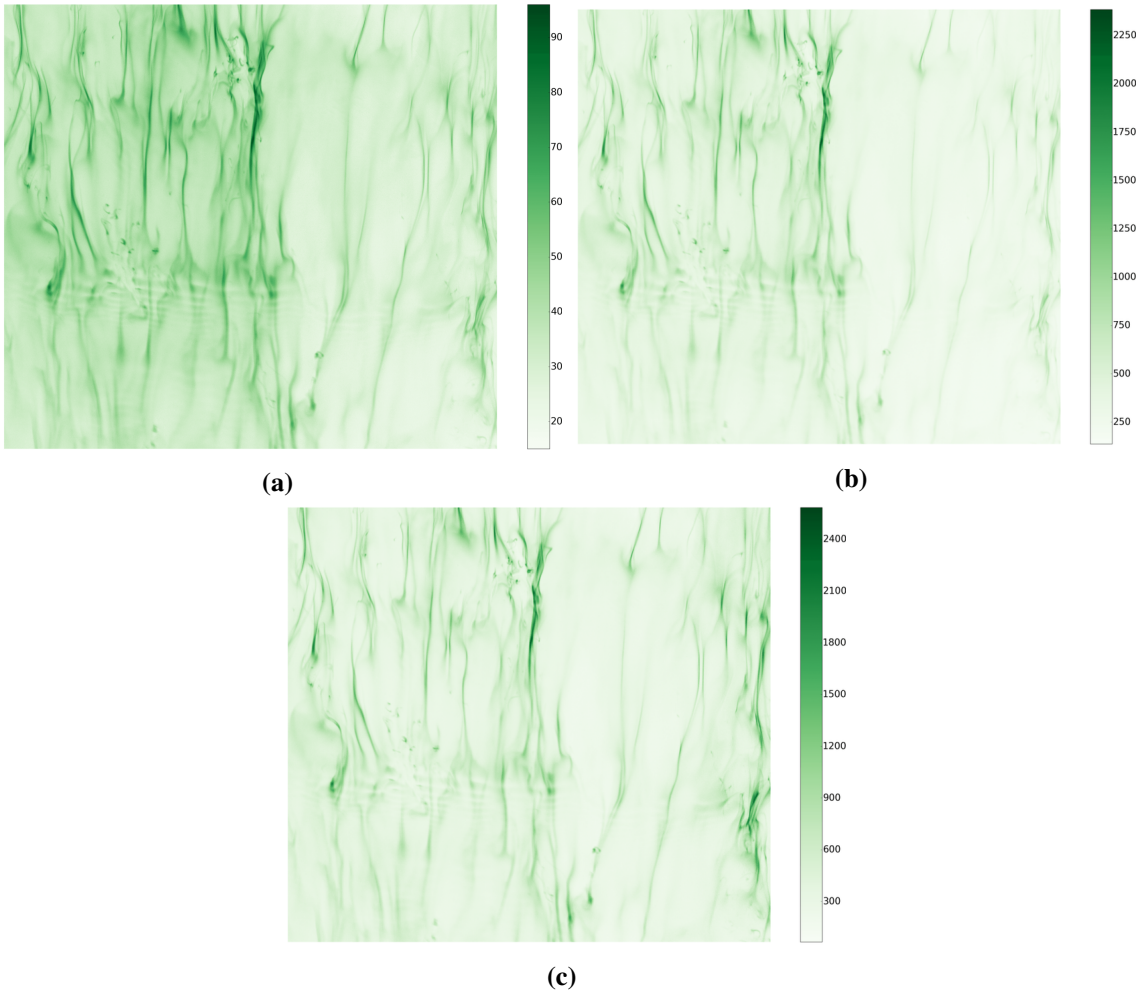

Figure 5.8.: Illustration of data processing steps for a single image from right camera. (a) The original image recorded at the reference wind speed of 2.16 m/s with turned off AC system. The size of the image is 30×40 cm^2. The ammonia concentration in the air side is about 7 ppm. (b) The image after LUT correction, that corresponds to eq. (5.7). (c) The image corrected for inhomogeneous illumination of the water surface and zero image. As one can see, the structures on the side of the image become well defined.

transformation is found using *cv2.stereoRectify* function with known camera matrices, distortion coefficients, rotation matrix and translation vector between coordinate systems of the first and the second cameras. The parameters for the left and right camera mentioned above are specified in eq. 5.2, eq. 5.3, eq. 5.4 and eq. 5.5, respectively. The remapping maps for each camera in both x- and y-directions are estimated using *cv2.initUndistortRectifyMap* function (for more details see appendix B).

An example of the rectified images of a single frame from the left and the right camera are shown in fig. 5.9.

As one can expect, the structures on the image from the left camera (fig. 5.9a) are tilted to the right in comparison to the image from the right camera (fig. 5.9b). Pictured horizontal lines at the same height intersect with the structures at different angles and locations. Rectified images from left and right cameras are shown in fig. 5.9c and 5.9d, respectively. The enlargement of the scene is a consequence of performed rectification. Therefore, the change of magnification is

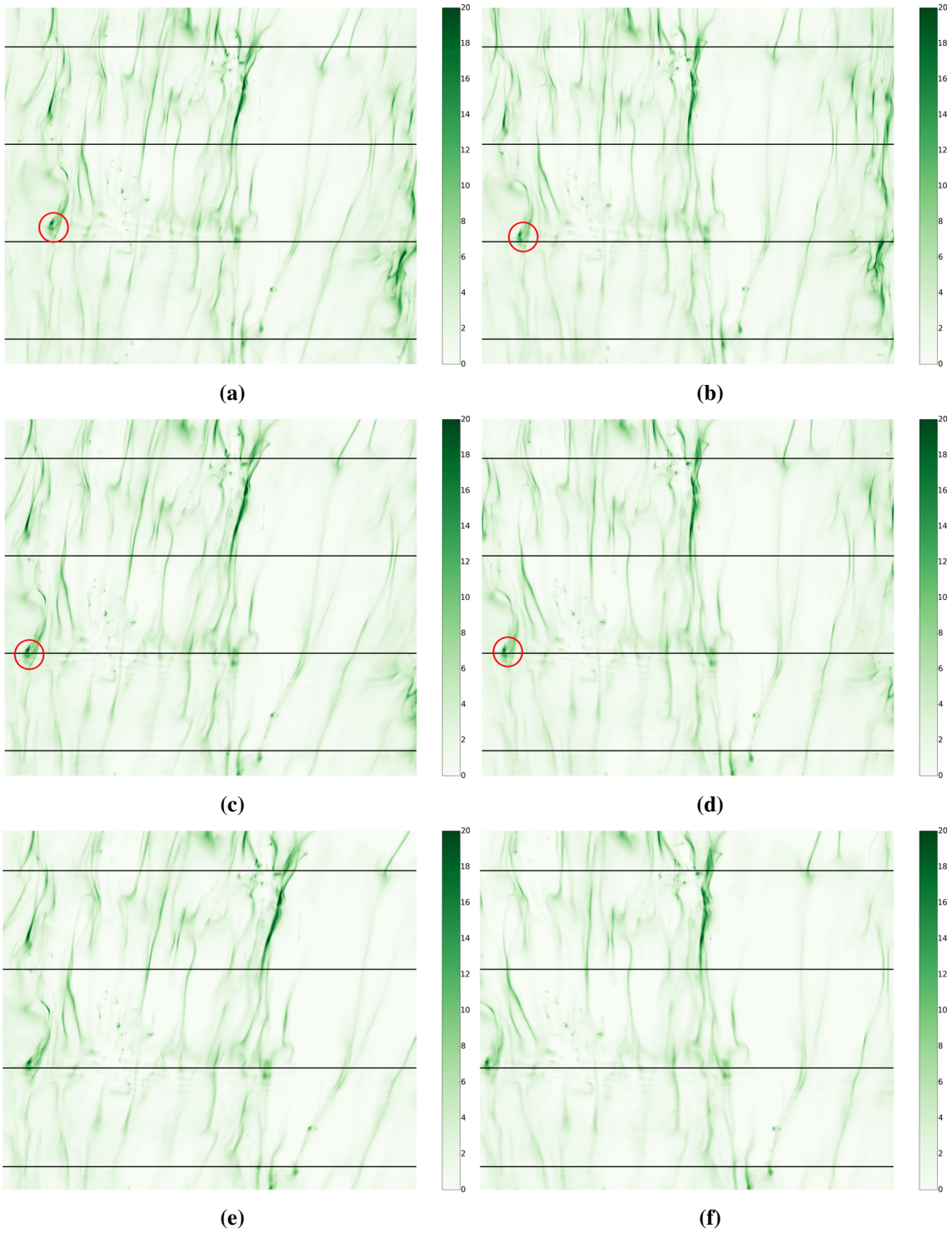

Figure 5.9.: Illustration of the rectification of preprocessed images from (a) left and (b) right cameras. The structures in the images touch the horizontal lines in different locations. The visual example of noticeable fluorescent pattern is marked in red cycle. In rectified images from (c) left and (d) right cameras, the horizontal line strike the pattern at the exact point. Preprocessed images from (e) left and (f) right cameras are obtained by additional cropping and shifting operations.

noticeable. The horizontal lines in the rectified images strike the structures at the same location. As the visible example, the red circle with a distinct fluorescent pattern is shown on both non-rectified

and rectified images from both cameras.

Prior to the disparity calculation in addition to rectification transform, preprocessing steps are required. It involves shifting and cropping of the images (the details can be found in appendix B). The preprocessing steps are necessary to observe the same scene (in this case, the same patch of the water surface) in the left and right image. An example of the images are shown in fig. 5.9e for the left and 5.9f for the right cameras.

Worth mentioning here, that the tilt of the structures remains in the rectified images as the cameras observing the scene at tilted angles.

5.2.3. Disparity Map Computation

Disparity itself refers to the difference in location of a certain object in corresponding left and right images of this object. The disparity value is estimated by a best match of small image regions around considered pixel in corresponding image. The disparity of a pixel is equal to the distance shift value that leads to minimum sum-of-squared-differences for that particular pixel.

To estimate a disparity map (distance map) having rectified images from left and right cameras, one needs to use feature detection and matching algorithms. The basic block-matching stereo algorithm works by using small "sum of absolute difference" (SAD) windows to find the matching between the points in the left and right images. The correspondence is searched for along the horizontal epipolar lines by a sliding SAD window. This algorithm finds only strongly matching points with high-texture.

The performance of the block-matching method, initialized with *cv2.StereoSGBM* function, depends on the number of specified parameters. The *minDisparity* parameter controls the matching search and identifies the start of the disparity for the algorithm. *numDisparities* parameter is a number of pixels the matching is searched over. Reducing the allowed number of disparities cuts down the computation time by limiting the length of a search for a matching point along epipolar line. *SADWindowSize* is a size a a matching block in pixels. The parameters *P1* and *P2* control disparity smoothness. *P1* is the penalty on the disparity change by plus or minus one between neighbour pixels. *P2* is the penalty on the disparity change by more than one between neighbour pixels. Suggested by *OpenCV* calculation of the parameters follows the rule:

$$P_i = penalty \cdot channels \cdot SAD^2 \tag{5.8}$$

where channels is a number of image channels, penalty is a number for penalty costs and SAD is a SAD window size in pixels.

For the processed images, the *minDisparity* parameter was set to zero. The *numDisparities* parameter was fixed the half of the resized image width - 560 pixels. The best value for SAD window size is 11 pixels. This value is used for block-matching method for all the images recorded at low wind speed values, as well as at higher wind speeds. The $P1$ and $P2$ parameters were varied from $P1 = 3 \cdot SAD^2$ and $P2 = 3 \cdot SAD^2 + 1$ up to $P1 = 8 \cdot SAD^2$ and $P2 = 24 \cdot SAD^2 + 1$.

An example of a disparity map, estimated for a single frame, presented in fig. 5.8 and 5.9, is shown in fig. 5.10.

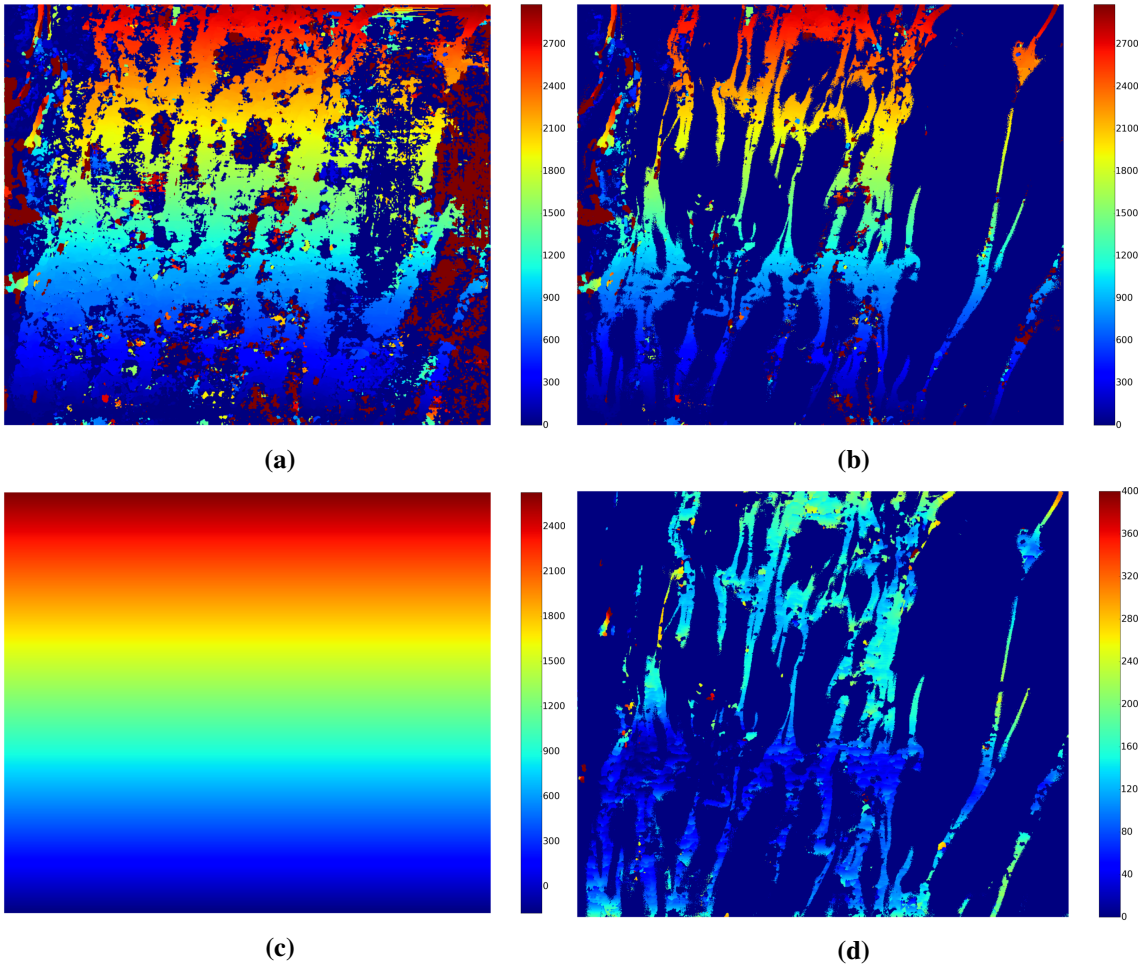

Figure 5.10.: The processing steps for disparity map estimation. High values of a disparity pixel shift represent smaller distances of the pixel to the origin of coordinate system and vice versa. (a) The original disparity map with the gradient of a pixel shift from the top to the bottom of the image and presence of artifacts. (b) Preselected disparity map for the areas with sufficient fluorescent signal. (c) Estimated tilting plane included in disparity map due to the tilt of the cameras. (d) The final disparity map with no tilting effect and illuminated artifacts.

As the fluorescent patterns in the image have a shape of long extended formation, the block-matching algorithm might not find appropriate match along the epipolar line in the image from the other camera. It is preferable for the images to contain well-defined corners of the fluorescent patterns. Supposedly due to scattering of light along 1 m of the water column and low depth of field, the corners of the fluorescent segments appear indistinct. Additionally, as the observed scene is transparent, the fluorescent pattern might change its presentation strongly. As an example, one can think of a case of one camera looking at two fluorescent segments located along the line from the optical center of the camera. In this case only one fluorescent segment will appear in the image with the joined intensity of two segments. While the other camera will see two roughly separated (depending on the distance between the segments) patterns. This scenario is not desirable for a block-matching algorithm, as at least one fluorescent pattern would not have any correspondence in the image from the other camera.

As it can be seen in fig. 5.10a, the area with relatively low fluorescent signal originates the gap

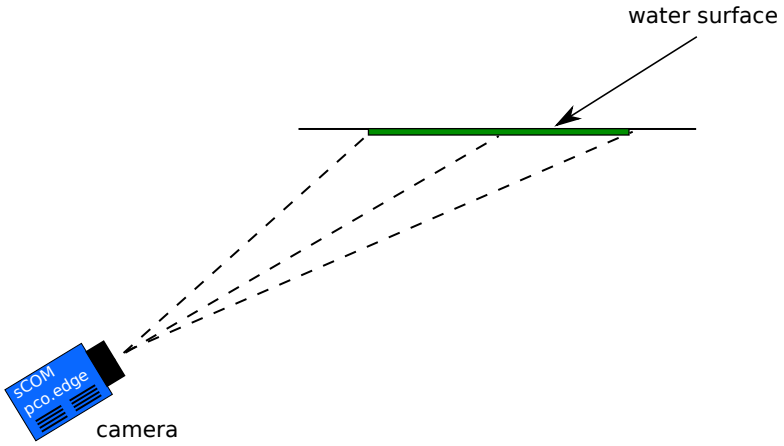

Figure 5.11.: A sketch explaining the gradient of estimated disparity values from the top to the bottom of the images. The wind direction is from left to right. The image is rotated in counter clockwise direction. Lower part of the image is on the right side of the sketch. The distance from the camera to the lower part of the image is larger, than to the upper part of the image.

in the disparity map. This occurs, as there are no initiative features to find correspondence to. Besides, the areas with no fluorescence or low intensities do not yield representative disparity shift values. To exclude this effect, one should estimate a binary mask of the fluorescent images from the left camera (as block-matching algorithms compute the disparity shift of a pixel in the left image that corresponds to the equivalent pixel in the right image). The result of this procedure is shown in fig. 5.10b.

The areas, where the algorithm fails to find a good matching point, have inconsistent large values for a disparity shift. Those areas are shown with dark red color in fig. 5.10a and 5.10b. To abandon those artifacts, the disparity map is corrected with manually setting the highest allowed shift (see text above).

Performed rectification includes the rearrangement of the cameras in a way, that the optical axes of both cameras are parallel to each other. As the cameras are additionally tilted in orthogonal to stereo base direction, the estimated disparity map has noticeable gradient from lower to upper part of the image. A sketch explaining this effect in presented in fig. 5.11. The tilt of the camera causes the lower part of the acquired image being further away, i.e. at the large distances from the camera, hence, lower disparity values.

In order to remove the tilting effect, the disparity map was estimated with high $P1$ and $P2$ parameters for additional smoothing. The tilting plane was fitted to averaged disparity map (see fig. 5.10c) and subtracted from disparity map of each frame. The disparity map after illuminating the tilt effect is presented in fig. 5.10d. Most of the structures have comparable disparity shift value, implying their location at the water surface.

As one can see on the fluorescent image (see fig. 5.8a), there is a wave in the lower part of the image. In the disparity map, it can be seen as a horizontal area of low disparity values, meaning larger distances. One should also note here, that there is a variation in the disparity shift values within number of single structures. That means that the streaks itself are moving closer or further away relative to the origin of coordinate system (in this case - the center of left camera).

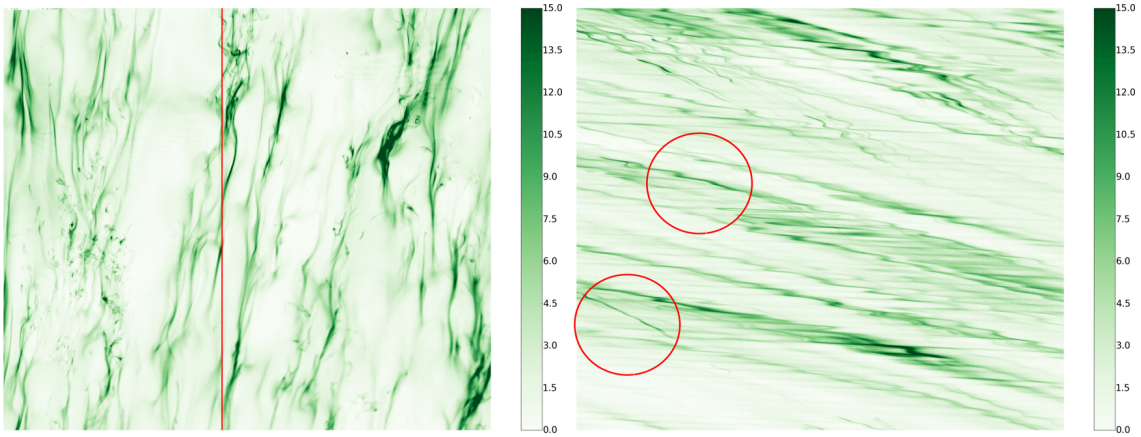

(a) **(b)**

Figure 5.12.: (a) The fluorescent image with fixed vertical line for the analysis of the streak's velocities. (b) Time-space image with noticeable different velocities of the streaks. Vertical and horizontal directions are time and space coordinates with scales of 15 s and 30 cm, respectively. The steep lines possess low velocity values, when low-pitched line have higher velocities and, therefore, assumed to be at the water surface.

Originally, to estimate the distance z of the object in the image having the disparity value, one simply can use a formula:

$$z = b\frac{f}{d} \tag{5.9}$$

where b is a length of the stereo base, f is a focal parameter in pixels and d is estimated disparity value. The estimated stereo base and the focal parameters are specified in sec. 5.1.2. Unfortunately, this formula does not include the tilt of the cameras towards the center of the measuring section and the distances at the different positions in the images appear with noticeable divergence.

Therefore, one needs to find the coordinates of each pixel in the real world. To estimate the coordinates of the objects in the images from the disparity values, one can use disparity-to-depth mapping matrix $\mathbf{Q}$ that is computed by *cv2.stereoRectify* function. With known $\mathbf{Q}$ matrix and disparity value for each pixel, *cv2.reprojectImageTo3D* function transforms the disparity map to a 3-channel image. The 3-channel image represents a 3D point cloud (for more details see appendix C).

5.2.4. Velocity Analysis

In addition to the dense reconstruction, the images from the cameras are evaluated for estimating the velocities of the fluorescent structures. To do so, one needs to fix a vertical line in the rectified images and illustrate this line at different time steps (similar to t-z image of one dimensional concentration profiles.) An example of the fluorescent image with specified vertical line and time sequence of this line along 1500 frames are given in fig. 5.12.

The vertical direction in fig. 5.12b represents the time coordinate, while the horizontal - space coordinate in along wind direction. The time and space scales of presented image are 15 s and roughly 30 cm, respectively. One can see that the structures undergo the vertical line with differ-

ent velocities - steep lines present slow movements, while small-inclined lines are faster as over same time, the distances they pass are larger. In order to estimate the value of the velocities, one needs to detect the lines in the image and to calculate the slope. The lines can be found using *cv2.HoughLines* function that detects the edges with Canny filtering procedure. The detection of the lines at the surface are complicated by the fact that the structures at the water surface are modulated by the waves. In particular the algorithm identifies single straight lines that are not modulated by the waves. Therefore, the line detection algorithm is excluded from the image evaluation.

It is well known, that at a wind driven interface, the water surface moves faster than the water bulk. It is assumed, that the steeper lines, i.e. the lines with lower velocities, are moving below the water surface. And the low-pitched lines are at the surface and possess high velocities.

5.3. Results of Aeolotron Measurements

5.3.1. Analysis of Near-Surface Turbulence

This section presents examples of snapshots of fluorescent footprint at the water surface for different wind conditions and gives a short description of the observed processes. The size of a single snapshot is $30\times40\,\mathrm{cm}^2$. The wind is blowing from the top towards the lower part of the image. The green areas in the images represent the region of high intensities of light emitted by Pyranine. As it was mentioned in sec. 3.2, the light is emitted if the pH value is larger than 7. Consequently, the green areas present the region with a high enough local ammonia concentration, sufficient to increase the pH value from the initial value of 4 to 7.

Example images for the reference wind speeds 1.52, 2.16, 2.79 and 3.88 m/s are given in fig. 5.13.

As one can see in the images in fig. 5.13, the ammonia penetrated through the air-water interface is accumulated in streaks along the wind direction. Due to an interaction of the shear stress induced by the wind and waves, counter-rotating vortices are forming in cross-wind direction. Those vortices are called Langmuir circulations. The vortices push the alkaline ammonia enriched surface water and transport acid bulk water to the surface. Therefore, fluorescent streaks almost parallel to the wind direction are visible in the images. Beneath those lines, the surface converges due to downward motion. In between the streaks there is upwelling motion.

Another type of along wind structures is referred to as fish-scale streaks. In comparison to Langmuir circulations, the fish-scales have a shorter life time and are independent of waves (Handler et al., 2001; Schnieders et al., 2013). Typical examples of Langmuir circulations and fish-scales are marked in the images for the lower reference wind speed values (1.52 and 2.16 m/s) in fig. 5.13a and 5.13b.

An essential characteristic of the streaks is the space scale L in between the streaks. As one can see in fig. 5.13, the distance between the streaks in cross wind direction decreases with increasing wind speed (for a quantitative analysis of the streaks scales, see Schnieders et al. (2013)).

At the reference wind speed of 2.16 m/s surface renewal events are visible (marked in fig. 5.13b). They can be interpreted as a replacement of the fluorescent surface water with "fresh" acid bulk

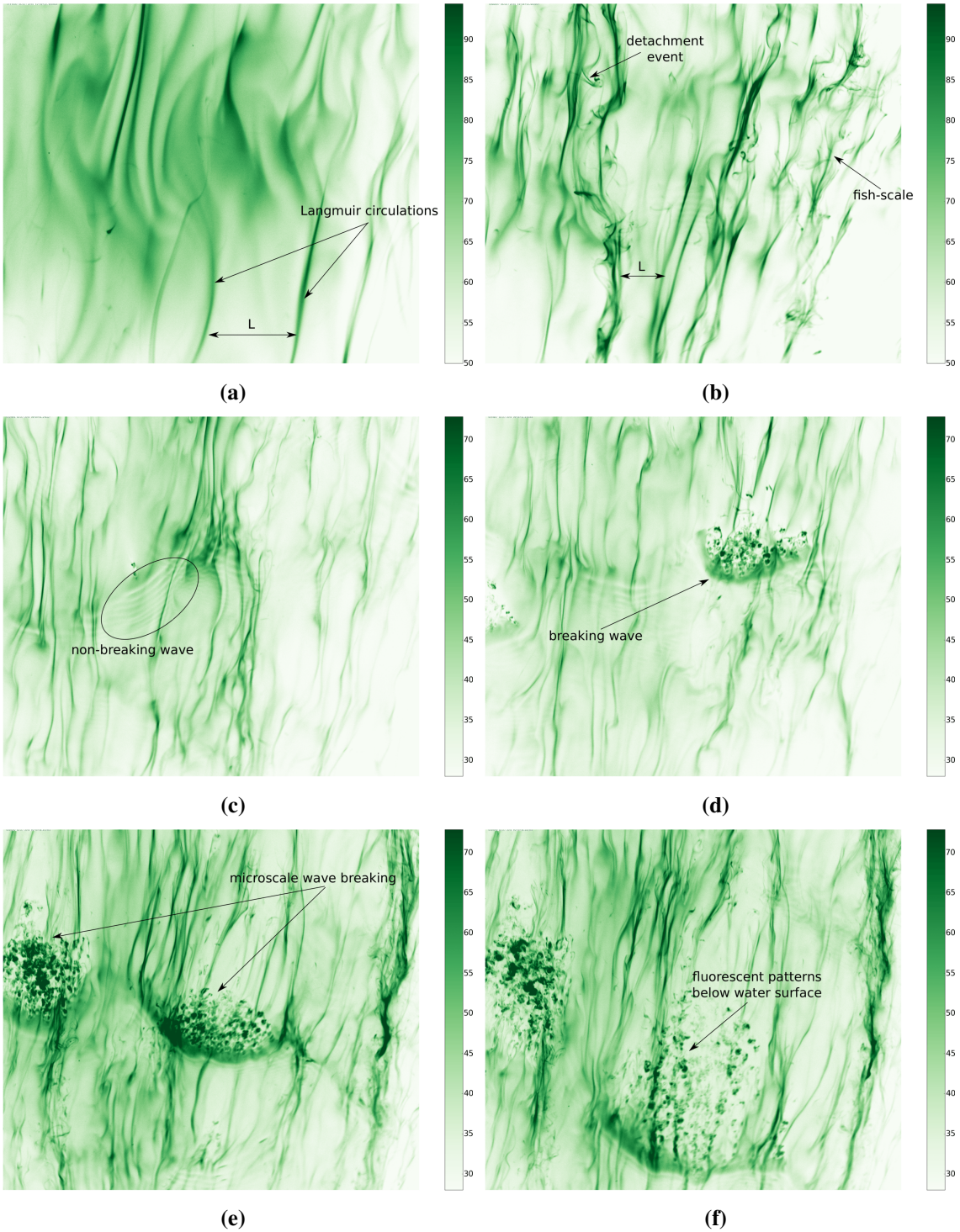

Figure 5.13.: Example images of the visualization of the mass boundary layer. The size of the images is $30 \times 40\,\mathrm{cm}^2$. The color map shows the relative intensity of the observed fluorescence emitted by Pyranine, where the local concentration of ammonia is sufficiently high to increase the pH value up to 7. Snapshots of the water surface at reference wind speeds of (a) 1.52 m/s, (b) 2.16 m/s, (c),(d) 2.79 m/s and (e),(f) 3.88 m/s. At lower wind speeds, the fluorescent streaks appear at larger distances in cross wind direction. Distinct detachment events occur starting with a wind speed of 2.16 m/s. They transport the fluorescent water close to the water surface downwards. At the higher wind speeds microscale wave breaking events are observed. The processes mentioned above enhance the gas transfer through the air-water interface.

water. With this processes the local area of high ammonia concentration is transported downwards to the water bulk. Therefore, the surface renewal events enhance the air-water gas transfer.

With increasing wind speed, the shear stress instability starts generating local wind waves. A capillary wave is a wave travelling along the boundary of a fluid, whose dynamics are dominated by the effects of surface tension. Turbulent wind flows form random pressure fluctuations at the water surface. The pressure fluctuations generate small capillary waves with a wavelength in the order of few centimeters. An example of a capillary wave can be seen in fig. 5.13c at the reference speed of 2.79 m/s. Those wave are non-breaking waves. The crest of the wave is visualized by the set of capillary formations and is marked in fig. 5.13c. In this case, the shear stress is stable and the waves are not breaking.

With the wind acting on the initially fluctuated water surface, the waves become larger. The pressure differences get larger along to the wave and the wave grows as well. Then the shear instability expedites the growing of the wave.

With increasing shear stress, the capillary waves become unstable and dissipate their energy. This event is called microscale wave breaking. The temporal development of typical microscale wave breaking is seen in fig. 5.13e and 5.13f. The time period in between the images is 0.1 s. As one can see, at first, ammonia is accumulated at the wave crest. After the wave is breaking, ammonia is transported toward the water bulk (illustrated with separate dark green patterns) with non-fluorescent area following the wave.

The interactions between the waves on the surface generate longer and larger gravity waves. Those waves modulate the height of the water surface and, therefore, reduce the sharpness of the images due to a small depth of field.

5.3.2. Dense Reconstruction

The images from the left and the right camera from the sets with 4 different wind speeds with active AC system were preprocessed and rectified as described in sec. 5.2.1 and 5.2.2. The disparity map was computed with the penalty parameters $P1 = 3 \cdot SAD^2$ and $P2 = 3 \cdot SAD^2 + 1$ for low wind speeds of 1.52 and 2.16 m/s and $P1 = 5 \cdot SAD^2$ and $P2 = 5 \cdot SAD^2 + 1$ for higher wind speeds of 2.79 and 3.88 m/s.

Examples of the disparity maps for a single frame at each wind condition are presented in fig. 5.14 and 5.15. In addition, the corresponding images of the fluorescent structures at the same time frame from the left camera are given.

At a turbine frequency of 5 Hz, the observed structures are smooth and wide. The distances in between the turbulent structures in cross wind direction are relatively large. The air conditioning slows down the flow of the water surface. Therefore, the downward motion of the fluorescent water close to the surface is not visible. Within separate streak in along wind direction, the disparity value does not vary notably and remains close to 200 pixels (see fig. 5.14b). This results in an assumption of a non wavy water surface as the distances of the structures to the camera are approximately equal. The disparity map is noisy as the straight prolong structures possess insufficient number of high texture features that are necessary to detect the correspondence between two

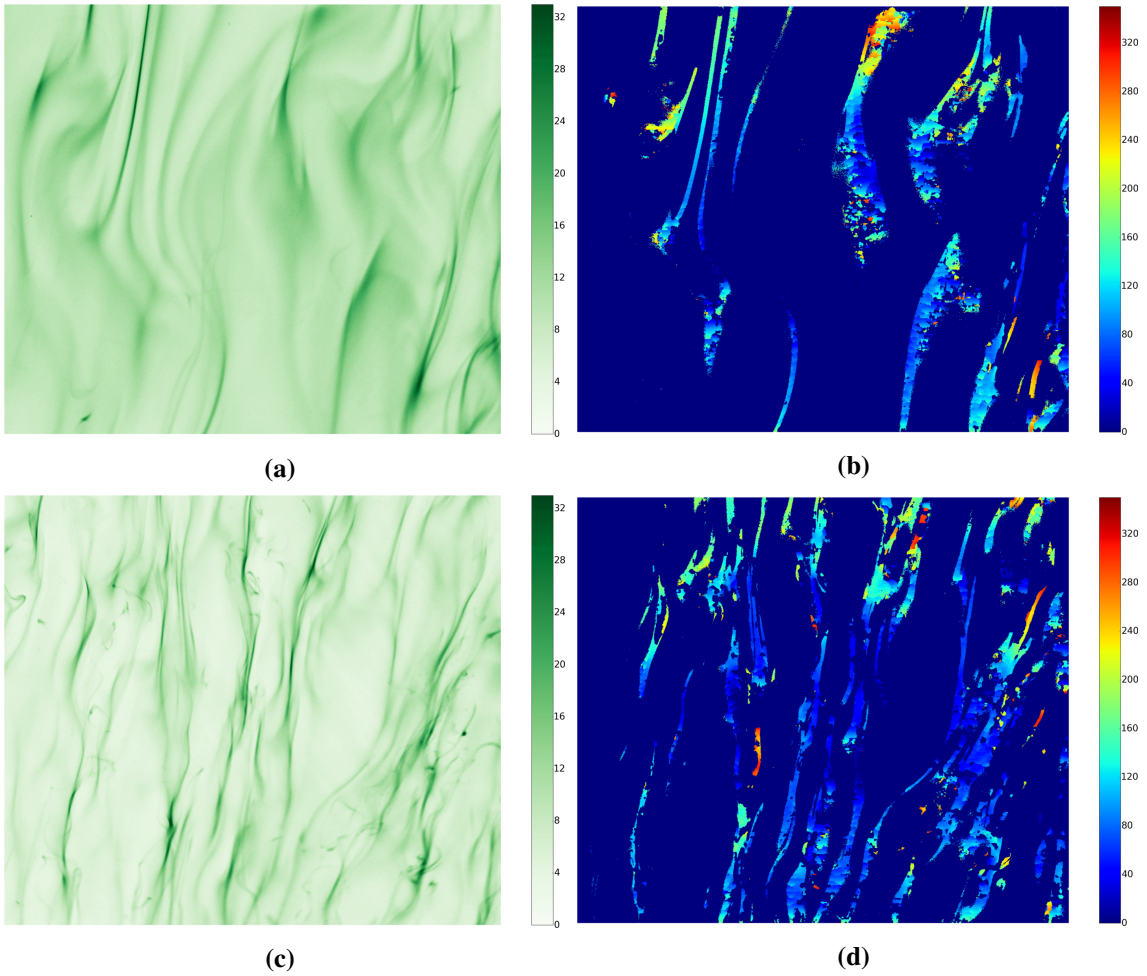

Figure 5.14.: Examples of fluorescent images along with a disparity map for low wind speeds of (a, b) 1.52 m/s and (c, d) 2.16 m/s. The typical characteristic of the images are prolong in a wind direction fluorescent streaks. As the block-matching algorithm does not cope with low texture features of stripes, the disparity maps include noisy shift values. At the higher reference wind speed of 2.16 m/s, the gradient of the disparity shift appears larger within separate streak. It implies large movements of the structures relative to the camera position.

images. Therefore, the algorithm fails to identify appropriate corresponding points of smooth and non-edgy areas.

At the reference wind speed of 2.16 m/s, the fluorescent streaks appear thinner and more frequent in cross wind direction. The detachment events occur and can be seen as tinier structures on the side of the main streaks. This also can be seen at the disparity map in fig. 5.14d. The shift value within the single fluorescent structure varies by a maximum of 200 pixels. As it can be seen in the figure, there is an area with low disparity values in the middle of the image. Supposably, it indicates a modulation of the water surface height by the presence of a wave.

The disparity map for the wind speed of 9 Hz is presented in fig. 5.15b. The typical wave at this wind condition is observed. As one should expect, the wave crest is illustrated in the disparity map with lower pixel shift values. This indicates, that the wave crest is positioned at a larger distance relative to the cameras than the rest of the fluorescent scene. The fluorescent patterns behind the wave (upper part of the image) are the separate areas of water with high ammonia concentration

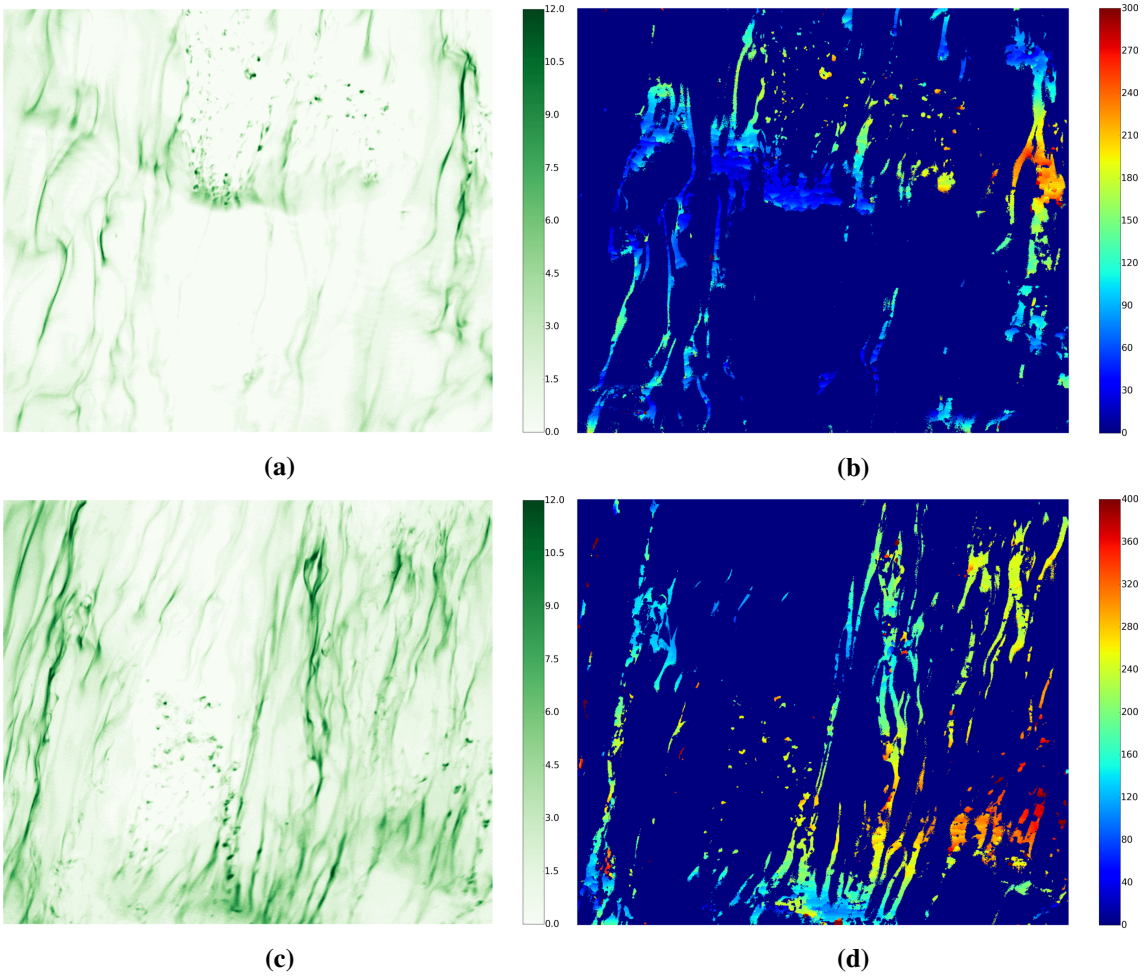

Figure 5.15.: Examples of fluorescent images along with a disparity map for high wind speeds of (a, b) 2.79 m/s, and (c, d) 3.88 m/s. The microscale wave breaking event and the number of detached fluorescent pattern increase. This simplifies the procedure of finding correspondence of pixels in the images. The disparity maps indicate the presence of the waves and change of the location of the fluorescent patterns relative to the cameras.

that got detached from the surface by renewal event. Those structures are moving towards the water bulk. This can be seen in the disparity map as the gradient in the disparity shift value rises in along wind direction (from wave crest to the upper side of the image). One should note here, that the disparity maps look more clear and less noisy as there are more high texture features detected in the images. The detected points are the result of a breaking wave, that leads to the appearance of separate well spotted structures that possess corner-shaped edges.

The disparity map for a wind condition with the turbine frequency of 12 Hz is shown in fig. 5.15d. At such a wind speed, the highest disparity of 400 pixels is observed. The frequency of wave breaking events is increasing (see Kräuter (2015)) with an increased number of separate fluorescent patterns detached from the water surface. As there is a number of good texture features in the fluorescent image, the disparity map is not as sparse as for conditions with lower wind speeds. Although the long structures across the full image get unreasonable disparity value. In those areas the block matching algorithm does not cope with finding an appropriate corresponding point in the

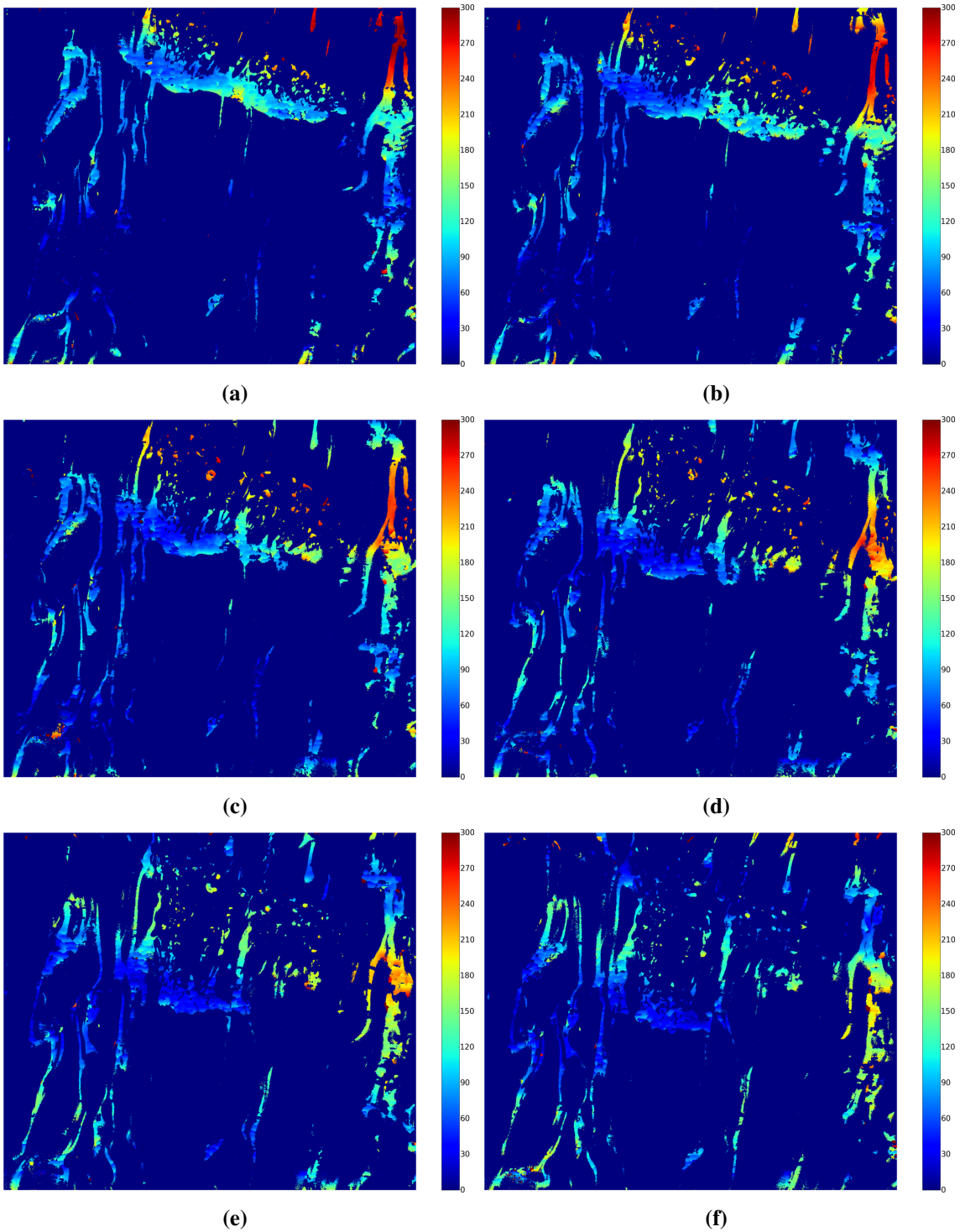

Figure 5.16.: Sequence of the disparity map at a reference wind speed of 2.79 m/s. The images are taken 0.04 s apart. The change of the disparity value within the separate streak is significant and can be observed in a time evolution of the structure on the right side of the image. The temporal development of the microscale wave breaking event is visualized. (a) The wave crest is formed and carry low disparity shift values, that indicate large distances of the wave from the cameras. (b) The fluorescent separate patterns are changing the disparity value implying the movement towards the water bulk. (d) The wave crest is fading out due to the break of the wave. (f) The fluorescent structures behind the wave dissolve in the water bulk and become invisible as the fluorescence is absorbed.

image from the other camera.

As the disparity map is calculated for each time frame separately, the time development of the water surface and the fluorescent structures can be followed in the time sequences of the disparity maps. For the case of the reference wind speed of 1.79 m/s the example of six images of the disparity map is presented in fig. 5.16.

The illustrated images are four time frames, i.e. 0.04 s, apart. The breaking microscale wave is moving by from the top of the image in along wind direction. In fig. 5.16a, the wave crest is developed and seen explicitly. Within the wave crest, the variation of the disparity value is present. In the upcoming time frame (fig. 5.16b), the fluorescent patterns behind the wave change the disparity shift to higher values, meaning the decrease of the distance to the cameras. In fig. 5.16d, the wave crest starts fading out. In fig. 5.16f the fluorescent pattern either is getting back to the water surface by a followed wave with lowering their disparity shift, or most likely, dissolving in the acid water bulk. One should note here, that the range of the pixel shift within the structure is higher in comparison to the lower wind speeds. The long structure along wind direction at the right side of the image is changing the disparity value from 300 pixels down to 200 pixels.

The analysis of the temporal development of the disparity maps allows following the movement of the structures within the third direction - depth coordinate. Worth mentioning, that the temporal evolution of the water surface is seen better when observing the video of the disparity maps rather than single images. Examples of temporal evolution of estimated disparity maps for different wind conditions can be found in appendix D.

5.3.3. Velocity-Based Analysis

As it was pointed out in sec. 5.2.4, the space-time images give an estimate of the velocity, the fluorescent streaks move with. As the quantitative analysis of velocities at the different wind speed conditions was out of scope of the thesis, the velocity of the streaks were estimated for a single measurement at the turbine frequency of 7 Hz with the reference wind speed of 2.16 m/s. The AC system was not in operation for the selected measurement. This condition was chosen, as it provides with fast moving structures in the absence of waves with high altitudes that might disturb the focusing of the cameras.

The time-space images, similar to the fig. 5.12b, for two vertical lines at the position of 70 and 370 pixels are shown in fig. 5.17. The vertical direction represents the time coordinate, while the horizontal direction - the space coordinate along wind direction. The time and space scales of the images are 6 s and 30 cm, respectively.

For the considered time-space images of two independent positions of the vertical line, the estimated velocity values for the first, second, third and fourth lines are 6.7, 4.9, 7.1 and 5.2 cm/s, respectively. As the magnification changes along the vertical line of the fluorescent image due to the tilting of the camera (see fig. 5.11), the estimated velocities need to be calculated with the known distance from the camera. One can clearly see in fig. 5.17b, that the line three bends along the time coordinate. This can be explained by the change of the magnification for the pixels along wind direction. To estimate the distance of the pixels, presenting the lines, the areas of interest

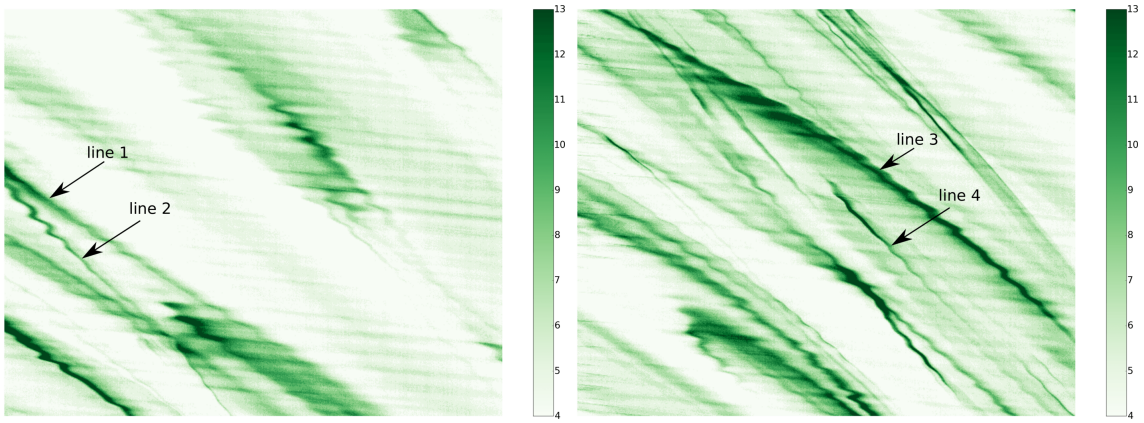

(a) **(b)**

Figure 5.17.: The time-space images for estimating the velocity of the structures moving at the different depth. The lines at the images have different slopes and, therefore, indicate various value of the velocities they move with. The lines 1 and 3 have lower slope in comparison to the lines 2 and 4, i.e. have higher velocities. It is assumed, that the line with higher velocities move at the water surface, while the structures with lower velocities move below the water surface.

were selected from the disparity map of corresponding time frames. The distances were calculated using the *cv2.reprojectImageTo3D* function that transforms the disparity map to a 3-channel image (sec. 5.2.3). For the first and the third line, the estimated distance is in order of 1.6 m, while for the second and fourth - 1.8 m. The obtained distance values were corrected for the refraction index of the water as the cameras are looking through the air-water interface. The details of the estimation of the streaks velocities can be found in appendix C.

The estimated velocities and the distances prove the suggestion of the structures at the water surface moving faster, than the structures below the water surface. Worth mentioning here, that the estimated velocities correspond with the measured velocities of the water bulk (see Bopp (2014)).

6. Discussion

6.1. Operability of Visualization Technique

The measurements at the linear wind-wave facility have been conducted in order to investigate the details of the novel LIF technique for the visualization of the mass boundary layer. As mentioned in sec. 4.3.3, one dimensional concentration profiles of a trace gas can be modified by tuning the concentration values of the used chemicals. With appropriate adjustments of the concentrations of the fluorescent dye, the trace gas and the initial conditions, the brightness profiles, corresponding to the concentration profiles, possess a steep drop at a certain neutral depth. Experiments with a high spatial resolution are necessary. Consequently, the measurements at the small linear facility were conducted as a first verification step of the novel LIF technique.

As it is mentioned in sec. 4.3.4, the estimation of the mass boundary layer thickness and local concentrations of ammonia at the water surface are not as trivial, as for LIF technique for concentration profiles (similar work was done by Friedl (2013)). It is associated with a non-linearity of the function P that defines the relation between the local concentration of ammonia and the fluorescent intensity (see eq. (4.6)). The fitting of the experimental brightness profiles to the corresponding concentration profiles for different gas exchange model (sec. 2.1.4) includes additional complexity. Therefore, the usage of the BLV technique is impractical for estimating the mass boundary layer thickness as a gas transfer parameter.

The measurements of one dimensional concentration profiles are suitable for the analysis of the operability of the novel LIF technique for the visualization of the mass boundary layer. It has been proven in sec. 4.3.3, that the concentration fields can be represented in a binary form. The binary brightness fields have been accomplished by tuning the necessary parameters as Pyranine, ammonia and HCl concentrations. Accordingly, the observed fluorescent light scene and, hence, the turbulent structures, maintain a fixed brightness value. Simplified in such a way concentration fields have a benefit for the visualization of mass boundary layer in three spatial dimensions, as the brightness of the observed fields is not depth dependent.

The research of air-water gas exchange is aiming to understanding the insights of the processes governing gas transfer at large scales in full three spatial and temporal dimensions. Therefore, the binary presentation of the concentration fields, accomplished by the BLV technique, was captured at the large annual Aeolotron facility. The same concentrations as during the experiments at the linear facility were used to provide binary form of concentration fields. Hence, a simplified scene of the observed turbulent processes was achieved and was thought to be reconstructed in the third spatial dimension.

6.2. Applicability of Trifocal Set-up

The number of cameras capturing the fluorescent light scene was fixed to three due to the limited amount of space available at the Aeolotron. With three projections of simplified light scene at different angles, tomographic reconstruction is intuitively sufficient to identify two fluorescent patterns separated by a non-fluorescent region. Additionally, as the observed fluorescent scene is transparent, the tomography seems suitable for reconstruction purposes.

A large field of research involving imaging of transparent objects is computerized tomography, which can be defined as the reconstruction of sectional slices of an object from images taken from different orientations. The tomographic imaging process can be described mathematically by a parallel projection known as the Radon transform (Anastasio et al., 2001). The Fourier slice theorem gives a simple relationship (in the Fourier domain) between the object and its projections. Specifically, the Fourier transform of a 1D projection can be shown to be equivalent to a slice of the 2D Fourier transform of the original object in a direction perpendicular to the direction of the projection.

The filtered back-projection algorithm, which can be seen as a computer implementation of Radon's inverse transform, plays an important role in reconstruction problems due to its simplicity and large number of available implementations in many programming languages. However, the reconstruction based on the filtered back-projection algorithm requires the projections for all angles from 0 to π. Additionally, it requires a number of projections at different angles to be in the order of hundred (Balazs and Gara, 2009; Batenburg, 2007).

The Algebraic Reconstruction Technique (ART) is a class of iterative algorithms used in computed tomography at a limited number of orientation angles. It permits to use a prior knowledge of the observed scene before its reconstruction, which makes it suitable for many practical applications (Batenburg et al., 2013). Additionally, Discrete Algebraic Reconstruction Tomography (DART) focuses on the problem of reconstruction from a small number of their projections, solving the limited angle tomography problem (Krimmel et al., 2005). There is a number of sparse discrete tomographic algorithms maintaining reconstruction of the scene at limited angles and restricted set of observed intensities.

According to Krimmel et al. (2005), the number of required projection used in DART are in the order of ten, which is still much larger than the number of projections used in the Aeolotron measurements. Within this reason, stereo algorithms were considered to gain additional depth information of the observed scene.

6.3. Reconstruction of Concentration Field

Many traditional computer stereo vision techniques are couched in a series of restrictive assumptions (Xu and Zhang, 1996; Zollhofer et al., 2014):

- the objects of interest are opaque, distinctively textured, and approximately Lambertian
- their motion is well approximated by affine transformations

- the cameras are well-calibrated
- viewing conditions are clear

These assumptions are typically met by using synthetic data or by operating in carefully crafted laboratory settings with set up scene. In real-world applications, those assumptions are relaxed and computer vision systems are deployed.

For the experiments conducted at the Aeolotron, the observed fluorescent scene does not obey many of the mentioned assumptions. The fluorescent light scene is highly transparent and scattered. The scene contains regions with low sharpness due to the change of the depth of field. The motion of the turbulence structures are extremely arbitrary and can involve shearing transform, that can not be explained by affine transformations. Viewing conditions are blurred as the cameras are looking through 1 m of water. Additionally, due to the tilt of the cameras in along wind direction, the fluorescent streaks in the left and right images are additionally tilted in opposite directions, that can not be corrected by image rectification.

Among many stereo vision variations, block-matching as a correspondence matching algorithm was selected due to its computational simplicity (Stuke et al., 2004). Although the block-matching algorithm is known to be noise-and light-sensitive, the disparity maps can been estimated with reasonable pixel shift values. One should mention here, that the stereo algorithm gives an estimate of the distance between the observed object and the camera. In the case of moving fluorescent structures, it is of interest to estimate the distance of the streaks relative to the water surface. With known water surface position, the full picture of the structures, their length and location below the water surface can be found. With this, the temporal development of the turbulent structures in three spatial dimensions can be achieved.

7. Conclusion and Outlook

7.1. Conclusion

Verification of BLV technique

In this thesis a novel technique for the visualization of the mass boundary layer has been developed. It is a radical departure from all previously used LIF techniques, which measure concentration profiles in the mass boundary layer (see sec. 3.1). In comparison to these techniques, it is suitable for visualizing the boundary layer at larger scales and simplifies the investigation of the turbulent structures by maintaining binary concentration fields. Therefore, the technique is suitable to visualize concentration fields in three spatial dimensions.

To visualize concentration fields, the alkaline tracer ammonia is penetrating through the air-water interface to slightly acid water, which contains the fluorescent dye Pyranine. By a change in pH to a threshold value of 7, ammonia is visualized in the mass boundary layer (see sec. 3.2). For a verification of the BLV technique and for finding the most suitable concentrations to maintain binary concentration fields, measurements of one dimensional brightness profiles were performed at the small linear wind-wave facility (see sec. 4.2). The measurements allowed the analysis of the one dimensional profiles with high spatial and temporal resolution. Mean brightness profiles corresponding to mean concentration profiles were recorded at different wind conditions and with different concentrations of the used chemicals. In the experiments, a dual-camera set-up was used (see sec. 4.2.1). It allowed the implementation of a surface detection algorithm on the basis of the images from an air-sided camera, which solved the complications faced in the work of Friedl (2013).

The analysis of the measured profiles at different concentrations allowed to draw the conclusion that a binary representation of the concentration fields can be maintained (see sec. 4.3.3). If the Pyranine concentration and the initial pH value are approx. 10^{-5} mol/L and 4, the brightness profiles have a sharp drop in intensity at the neutral layer depth (pH = 7). Most importantly, it has been proven that the technique can be used to reconstruct concentration fields with a multiple view geometry.

The mean brightness profiles were also analysed and fitted to different gas exchange models (see sec. 4.3.4). The estimation of the mass boundary layer thickness was complicated due to the non-linearity of the transmission to the BLV technique. For low wind speeds, the fitting has been realized by a cross-validation algorithm. The estimated boundary layer thickness conforms with the estimated transfer velocity calculated from the air-sided concentration of ammonia.

Towards four dimensional visualization

Experiments with a trifocal camera set-up were conducted at the large annual facility Aeolotron (see sec. 5.1). The aim of these measurements was to reconstruct the concentration fields in four dimensions. The full calibration of the cameras was performed in order to estimate the exact positioning and orientation of the cameras. This is of importance for a decent performance of the stereo algorithm. With the limited number of three cameras, the stereo vision algorithm was selected as a method for extracting information about the turbulent structures in the third spatial dimension. The left and right camera were used to perform the disparity map estimations (see sec. 5.2.3). Within the range of available correspondence algorithms, the block-matching algorithm was used due to its simplicity and fast time performance. Reasonable disparity maps were achieved for the recorded wind conditions (see sec. 5.3.2).

The temporal evolution of the estimated disparity maps preserve the temporal turbulent movements. In such a way, the processes, governing the gas exchange through the air-water interface, such as Langmuir circulations, detachment events from the water surface and microscale wave breaking, have been observed in three spatial and the temporal dimensions (see sec. 5.3).

7.2. Outlook

With the set-up used in the current study, there is a number of possible improvements. At first, the tilting of the cameras complicates the calibration and rectification procedures (as it includes non-linearity of the calibration due to the refraction index of water). As a result of the tilt, the disparity maps maintain positive and negative disparities, as the structures at the top and at the bottom of the image move towards different sides. The tilt can be simply avoided by placing the cameras straight under the observed scene.

Additionally, simultaneous water surface elevation measurements are required to estimate the location of the structures relative to the water surface. Within this information, the full scene of the turbulent processes can be achieved. Worth mentioning here, that the first data were recorded along the work of this thesis, although the data processing is yet to be done.

The comparison of the BLV images with infrared images are of interest to find a correspondence between the mass and momentum transfer. The first steps towards this concept was made by Kräuter (2015). Within this thesis, the data with a larger patch of the water surface was recorded and available for further processing.

Finally, by having a full four dimensional picture of the measured turbulent structures, a comparison to numerical simulations of turbulence can be maintained in all four dimensions.

Bibliography

Anastasio, M. A., Pan, X., and Clarkson, E.: Comments on the filtered backprojection algorithm, range conditions, and the pseudoinverse solution, IEEE Transactions on Medical Imaging, 20, 539–542, 2001.

Asher, W. and Litchendorf, T.: Visualizing near-surface concentration fluctuations using laser-induced fluorescence, Exp. Fluids, 46, 243–253, doi: 10.1007/s00348-008-0554-9, 2009.

Avnir, Y. and Barenholz, Y.: pH determination by pyranine: medium-related artifacts and their correction, Analytical biochemistry, 347, 34–41, 2005.

Avnir, Y. and Barenholz, Y.: Erratum to "pH determination by pyranine: Medium-related artifacts and their correction" [Anal. Biochem. 347 (2005) 34–41], Analytical Biochemistry, 351, 317, 2006.

Bakker, D. C. E., Bange, H. W., Gruber, N., Johannessen, T., Upstill-Goddard, R. C., Borges, A. V., Delille, B., Löscher, C. R., Naqvi, S. W. A., Omar, A. M., and Santana-Casiano, J. M.: Air-sea interactions of natural long-lived greenhouse gases (CO_2, N_2O, CH_4) in a changing climate, in: Ocean-Atmosphere Interactions of Gases and Particles, edited by Liss, P. S. and Johnson, M. T., pp. 113–169, Springer, doi: 10.1007/978-3-642-25643-1_3, 2014.

Balazs, P. and Gara, M.: An evolutionary approach for object-based image reconstruction using learnt priors, in: Image Analysis, pp. 520–529, Springer, 2009.

Barnadas-Rodríguez, R. and Estelrich, J.: Photophysical Changes of Pyranine Induced by Surfactants: Evidence of Premicellar Aggregates, The Journal of Physical Chemistry B, 113, 1972–1982, 2009.

Batenburg, K. J.: A network flow algorithm for reconstructing binary images from discrete X-rays, Journal of Mathematical Imaging and Vision, 27, 175–191, 2007.

Batenburg, K. J., Fortes, W., Hajdu, L., and Tijdeman, R.: Bounds on the quality of reconstructed images in binary tomography, Discrete Applied Mathematics, 161, 2236–2251, 2013.

Beutelspacher, A. R. U.: Projective Geometry: From Foundations to Applications, Cambdridge Univ. Press, 1998.

Bigler, E.: Depth of field and Scheimpflug's rule: a "minimalist" geometrical approch, 2002.

Binney, J. and Skinner, D.: The Physics of Quantum Mechanics, Capella Archive, 2008.

Bohm, G. and Zech, G.: Introduction to Statistics and Data Analysis for Physicists, Verlag Deutsches Elektronen-Synchrotron, 2010.

Bopp, M.: Luft- und wasserseitige Strömungsverhältnisse im ringförmigen Heidelberger Wind-Wellen-Kanal (Aeolotron), Masterarbeit, Institut für Umweltphysik, Universität Heidelberg, Germany, URL http://www.ub.uni-heidelberg.de/archiv/17151, 2014.

Bradski, G., K. A.: Learning OpenCV: Computer Vison with the OpOpen Library, O'reilly, 2008.

Braud, C., Heitz, D., Braud, P., Arroyo, G., and Delville, J.: Analysis of the wake-mixing-layer interaction using multiple plane PIV and 3D classical POD, Exp. Fluids, 37, 95–104, doi: 10.1007/s00348-004-0789-z, 2004.

Clegg, S. L. and Brimblecombe, P.: Solubility of ammonia in pure aqueous and multicomponent solutions, J. Phys. Chem, doi: 10.1021/j100357a041, 1989.

Coantic, M.: A model of gas transfer across air–water interfaces with capillary waves, J. Geophys. Res., 91, 3925–3943, doi: 10.1029/JC091iC03p03925, 1986.

Crimaldi, J. P.: Planar laser induced fluorescence in aqueous flows, Exp. Fluids, pp. 44:851–863, doi: 10.1007/s00348-008-0496-2, 2008.

Csanady, G.: Turbulent diffusion in the environment, D. Reidel Publishing Company, 1973.

Danckwerts, P. V.: Significance of a liquid-film coefficients in gas absorption, Ind. Eng. Chem., 43, 1460–1467, doi: 10.1021/ie50498a055, 1951.

Dani, A., Guiraud, P., and Cockx, A.: Local measurement of oxygen transfer around a single bubble by planar laser-induced fluorescence, Chemical Engineering Science, 62, 7245 – 7252, doi: DOI:10.1016/j.ces.2007.08.047, URL http://www.sciencedirect.com/science/article/pii/S0009250907006914, 8th International Conference on Gas-Liquid and Gas-Liquid-Solid Reactor Engineering, 2007.

Dasgupta, P. K. and Dong, S.: Solubility of ammonia in liquid water and gerneration of trace levels of standard gaseous ammonia, Atmospheric Environment, 20, 565–570, doi: 10.1016/0004-6981(86)90099-5, 1986.

Davies, J. T.: Turbulence Phenomena. An Introduction to the Eddy Transfer of Momentum, Mass, and Heat, Particularly at Interfaces, Academic Press, New York, 1972.

Doney, S. C., Fabry, V. J., Feely, R. A., and Kleypas, J. A.: Ocean acidification: the other CO2 problem, Annu. Rev. Marine Sci., 1, 169–192, doi: 10.1146/annurev.marine.010908.163834, 2009.

Engelmann, D.: 3D-Flow Measurement by Stereo Imaging, Dissertation, IWR, Fakultät für Physik und Astronomie, Univ. Heidelberg, URL http://www.ub.uni-heidelberg.de/archiv/1070, 2000.

Fabry, E. P.: 3D holographie PIV with a forward-scattering laser sheet and stereoscopic analysis, Exp. Fluids, 24, 39–46, 1998.

Falkenroth, A.: Visualisation of Oxygen Concentration Profiles in the Aqueous Boundary Layer, Dissertation, Fakultät für Chemie und Geowissenschaften, Univ. Heidelberg, URL http://www.ub.uni-heidelberg.de/archiv/7672, 2007.

Friedl, F.: Investigating the Transfer of Oxygen at the Wavy Air-Water Interface under Wind-Induced Turbulence, Dissertation, Institut für Umweltphysik, Fakultät für Physik und Astronomie, Univ. Heidelberg, URL http://www.ub.uni-heidelberg.de/archiv/14582, 2013.

Friedl, F., Arnold, N., and Jähne, B.: Visualization of vertical cross-wind oxygen concentration fields at the air-water interface, in: 7th International Symposium on Gas Transfer at Water Surfaces, Seattle, May 18–21, 2015, abstract, accepted as poster, 2015.

Hales, J. M. and Drewes, D. R.: Solubility of ammonia in water at low concentrations, Atmospheric Environment, 13, 1133–1147, doi: 10.1016/0004-6981(79)90037-4, 1979.

Handler, R. A., Smith, G. B., and Leighton, R. I.: The thermal structure of an air–water interface at low wind speeds, Tellus A, 53, 233–244, doi: 10.1034/j.1600-0870.2001.00158.x, 2001.

Harriott, P.: A random eddy modification of the penetration theory, Chem. Eng. Sci., 17, 149–154, doi: 10.1016/0009-2509(62)80026-8, 1962.

Hartley, R. and Zisserman, A.: Multiple View Geometry in Computer Vision, Cambridge Univ Press, 2 edn., 2003.

Herlina and Jirka, G. H.: Turbulent gas flux measurements near the air-water interface in a grid-stirred tank, in: Transport at the Air Sea Interface — Measurements, Models and Parameterizations, edited by Garbe, C. S., Handler, R. A., and Jähne, B., pp. 25–41, Springer-Verlag, Berlin, Heidelberg, doi: 10.1007/978-3-540-36906-6_2, 2007.

Herzog, A.: Imaging of Water-sided Gas-Concentration Fields at a Wind-Driven, Wavy Air-Water Interface, Dissertation, Institut für Umweltphysik, Fakultät für Physik und Astronomie, Univ. Heidelberg, URL http://www.ub.uni-heidelberg.de/archiv/11220, 2010.

Herzog, A. G., Friedl, F., and Jähne, B.: Spatio-temporal fluctuations of water-sided gas concentration fields under wind-induced turbulence, in: 6th Int. Symp. Gas Transfer at Water Surfaces, Kyoto, May 17–21, 2010, doi: 10.5281/zenodo.14929, abstract, 2010.

Hiby, J. W.: Eine Fluoreszenzmethode zur Untersuchung des Transportmechanismus bei der Gasabsorption im Rieselfilm, Wärme- und Stoffübertragung, 1, 105–116, doi: 10.1007/BF00750793, 1968.

Hiby, J. W.: The chemical indicator: a tool for the investigation of concentration fields in liquid, Ann. N. Y. Acad. Sci., 404, 348–349, doi: 10.1111/j.1749-6632.1983.tb19494.x, 1983.

Higbie, R.: The rate of absorption of a pure gas into a still liquid during short periods of exposure, Trans. Am. Inst. Chem. Eng., 31, 365–389, 1935.

Holzwarth, G., Balmer, R. G., and Soni, L.: The fate of chlorine and chloramines in cooling towers, Water Research, 18(11), 1421–1427, 1984.

Hsu, C. T., Hsu, E. Y., and Street, R. L.: On the structure of turbulent flow over a progressive water wave: theory and experiment in a transformed, wave-following co-ordinate system, J. Fluid Mech., 105, 87–117, doi: 10.1017/S0022112081003121, 1981.

IPCC: Climate Change 2007: The Physical Science Basis. Contribution of Working Group I to the Fourth Assessment Report of the Intergovernmental Panel on Climate Change, Cambridge University Press, Cambridge, United Kingdom and New York, NY, USA, URL http://www.ipcc.ch/, 2007.

Jähne, B.: Zur Parametrisierung des Gasaustauschs mit Hilfe von Laborexperimenten, Dissertation, Institut für Umweltphysik, Fakultät für Physik und Astronomie, Univ. Heidelberg, doi: 10.5281/zenodo.10443, URL http://www.ub.uni-heidelberg.de/archiv/16796, iUP D-145, Link Nationalbibliothek http://d-nb.info/810123614, 1980.

Jähne, B.: Transfer processes across the free water interface, Habilitation thesis, Institut für Umweltphysik, Fakultät für Physik und Astronomie, Univ. Heidelberg, doi: 10.5281/zenodo.12202, URL http://www.ub.uni-heidelberg.de/archiv/16798, iUP D-200, 1985.

Jähne, B.: From mean fluxes to a detailed experimental investigation of the gas transfer process, in: 2nd International Symposium on Gas Transfer at Water Surfaces - Air–Water Mass Transfer, Minneapolis 1990, edited by Wilhelms, S. C. and Gulliver, J. S., pp. 244–256, ASCE, doi: 10.5281/zenodo.12204, 1991.

Jähne, B.: Air-sea gas exchange, in: Encyclopedia Ocean Sciences, edited by Steele, J. H., Turekian, K. K., and Thorpe, S. A., pp. 147–156, Elsevier, doi: 10.1016/B978-012374473-9.00642-1, invited, 2009.

Jähne, B.: Compression by Noise Equalization, doi: 10.5072/zenodo.12761, 2013.

Jähne, B. and Haußecker, H.: Air-water gas exchange, Annu. Rev. Fluid Mech., 30, 443–468, doi: 10.1146/annurev.fluid.30.1.443, 1998.

Jähne, B. and Münnich, K. O.: Momentum induced gas exchange through a smooth water surface, models and experimental results from linear and circular wind-water tunnels, in: Berichte aus dem Sonderforschungsbereich 94 Meeresforschung - Symposium on Capillary Waves and Gas Exchange, Trier July 2–6, 1979, edited by Broecker, H. C. and Hasse, L., 17, pp. 55–62, Univ. Hamburg, doi: 10.5281/zenodo.10257, 1980.

Jähne, B., Wais, T., Memery, L., Caulliez, G., Merlivat, L., Münnich, K. O., and Coantic, M.: He and Rn gas exchange experiments in the large wind-wave facility of IMST, J. Geophys. Res., 90, 11,989–11,998, doi: 10.1029/JC090iC06p11989, 1985.

Jähne, B., Libner, P., Fischer, R., Billen, T., and Plate, E. J.: Investigating the transfer process across the free aqueous boundary layer by the controlled flux method, Tellus, 41B, 177–195, doi: 10.1111/j.1600-0889.1989.tb00135.x, 1989.

Kerr, D. A.: The Scheimpflug Principles, Tech. rep., 2006.

Khatiwala, S., Tanhua, T., Mikaloff Fletcher, S., Gerber, M., Doney, S. C., Graven, H. D., Gruber, N., McKinley, G. A., Murata, A., Ríos, A. F., and Sabine, C. L.: Global ocean storage of anthropogenic carbon, Biogeosciences, 10, 2169–2191, doi: 10.5194/bg-10-2169-2013, URL http://www.biogeosciences.net/10/2169/2013/, 2013.

Kiefhaber, D.: Optical Measurement of Short Wind Waves — from the Laboratory to the Field, Dissertation, Institut für Umweltphysik, Fakultät für Physik und Astronomie, Univ. Heidelberg, URL http://www.ub.uni-heidelberg.de/archiv/16304, 2014.

Kiefhaber, D., Reith, S., Rocholz, R., and Jähne, B.: High-speed imaging of short wind waves by shape from refraction, J. Europ. Opt. Soc. Rap. Public., 9, 14 015, doi: 10.2971/jeos.2014.14015, 2014.

Kinsman, B.: Wind Waves: Their Generation and Propagation on the Ocean Surface, Prentice-Hall, Englewood Cliffs, 1965.

Kock, A., Schafstall, J., Dengler, M., Brandt, P., and Bange, H. W.: Sea-to-air and diapycnal nitrous oxide fluxes in the eastern tropical North Atlantic Ocean, Biogeosciences, 9, 957–964, doi: 10.5194/bg-9-957-2012, 2012.

Krah, N.: Visualization of air and water-sided concentration profiles in laboratory gas exchange experiments, Dissertation, Institut für Umweltphysik, Fakultät für Physik und Astronomie, Univ. Heidelberg, URL http://www.ub.uni-heidelberg.de/archiv/16895, 2014.

Krall, K. E.: Laboratory Investigations of Air-Sea Gas Transfer under a Wide Range of Water Surface Conditions, Dissertation, Institut für Umweltphysik, Fakultät für Physik und Astronomie, Univ. Heidelberg, URL http://www.ub.uni-heidelberg.de/archiv/14392, 2013.

Kraus, S.: DOASIS a framework design for DOAS, Dissertation, Technische Informatik, Univ. Mannheim, 2006.

Krimmel, S., Baumann, J., Kiss, Z., Kuba, A., Nagy, A., and Stephan, J.: Discrete tomography for reconstruction from limited view angles in non-destructive testing, Electronic Notes in Discrete Mathematics, 20, 455–474, 2005.

Kräuter, C.: Aufteilung des Transferwiderstands zwischen Luft und Wasser beim Austausch flüchtiger Substanzen mittlerer Löslichkeit zwischen Ozean und Atmosphäre, Diplomarbeit, Institut für Umweltphysik, Fakultät für Physik und Astronomie, Univ. Heidelberg, URL http://www.ub.uni-heidelberg.de/archiv/13010, 2011a.

Kräuter, C.: Partitioning of the Transfer Resistance Between Air and Water for Moderately Soluble Volatile Tracers, in: 4th Annual SOPRAN Meeting, 2011b.

Kräuter, C.: Visualization of air-water gas exchange, Dissertation, Institut für Umweltphysik, Fakultät für Physik und Astronomie, Univ. Heidelberg, URL http://www.ub.uni-heidelberg.de/archiv/18209, 2015.

Kräuter, C., Trofimova, D., Kiefhaber, D., Krah, N., and Jähne, B.: High resolution 2-D fluorescence imaging of the mass boundary layer thickness at free water surfaces, J. Europ. Opt. Soc. Rap. Public., 9, 14 016, doi: 10.2971/jeos.2014.14016, 2014.

Lakowicz, J. R.: Principles of Fluorescence Spectroscopy, Springer, 3. edn., doi: 10.1007/978-0-387-46312-4, 2006.

Lewis, W. K. and Whitman, W. G.: Principles of gas absorption, Industrial and Engineering Chemistry, 16, 1215–1220, doi: 10.1021/ie50180a002, 1924.

Liansheng, S., J. Z. D. C.: Image Rectification Using Affine Epipolar Geometric Constraint, Journal of Software, 4, 26–33, 2009.

Liss, P. S. and Slater, P. G.: Flux of gases across the air-sea interface, Nature, 247, 181–184, doi: 10.1038/247181a0, 1974.

Loop, C. and Zhang, Z.: Computing Rectifying Homographies for Stereo Vison, Tech. rep., Microsoft Research, 1999.

Mühlfriedel, K. and Baumann, K.-H.: Concentration measurements during mass transfer across liquid-phase boundaries using planar laser induced fluorescence PLIF, Exp. Fluids, 28, 279–281, 2000.

Münsterer, T.: LIF Investigation of the Mechanisms Controlling Air–Water Mass Transfer at a Free Interface, Dissertation, Institut für Umweltphysik, Fakultät für Physik und Astronomie, Univ. Heidelberg, doi: 10.5281/zenodo.14542, 1996.

Münsterer, T. and Jähne, B.: LIF measurements of concentration profiles in the aqueous mass boundary layer, Exp. Fluids, 25, 190–196, doi: 10.1007/s003480050223, 1998.

O'Neil, M. J.: The Merck Index. An Encyclopaedia of Chemicals, Drugs and Biologicals, Merck Research Laboratories, 14 edn., 2006.

Platt, U. and Stutz, J.: Differential Optical Absorption Spectroscopy, Principles and Applications, Physics of Earth and Space Environments, Springer, doi: 10.1007/978-3-540-75776-4, 2008.

Platt, U., Perner, D., and Pätz, H. W.: Simultaneous Measurement of Atmospheric CH_2O, O_3 and N_2O by Differential Optical Absorption., J. Geophys. Res., 84, 6329–6335, 1979.

Prayer, C.: Etude du transfert photoinduit de proton dans un hydroxyarène, la pyranine. Compétition avec le transfert photoinduit d'électron à un accepteur, le méthylviologène., Ph.D. thesis, L'Université Paris VI, Frankreich, 1997.

Prince, S. J. D.: Computer vision: models, learning and inference, Cambdridge Univ. Press, 2012.

Raffel, M., Gharib, M., Ronneberger, O., and Kompenhans, J.: Feasibility study of three-dimensional PIV by correlating images of particles within parallel light sheet planes, Exp. Fluids, 19, 69–77, doi: 10.1007/BF00193852, 1995.

Ramalingam, S. P., Tardif, J.-P., Gasparini, S., and Barreto, J.: Camera Models and Fundamental Concepts Used in Geometric Computer Vision, Mitsubishi Electric Research Labortatories, 2011.

Sander, R.: Compilation of Henry's law constants, version 3.99, Atmos. Chem. Phys. Discuss., 14, 29 615–30 521, doi: 10.5194/acpd-14-29615-2014, 2014.

Schnieders, J., Garbe, C., Peirson, W., Smith, G., and Zappa, C.: Analyzing the footprints of near surface aqueous turbulence - an image processing based approach, J. Geophys. Res., 118, 1272–1286, doi: 10.1002/jgrc.20102, 2013.

Shi, Q., Davidovits, P., Jayne, J., Worsnop, D., and E., K. C.: Uptake of gas-phase ammonia. 1. Uptake by aqueous surfaces as a function of pH, Journal of Physical Chemistry A, 103, 8812–8823, doi: 10.1021/jp991696p, 1999.

Society, T. R.: Ocean acidification due to increasing atmospheric carbon dioxide, The Royal Society, 2005.

Stuke, I., Aach, T., Mota, C., and Barth, E.: Estimation of multiple motions using block-matching and Markov random elds, in: Visual Communication and Image Processing, 2004.

Szeliski, R.: Computer Vision: Algorithms and Applications, Springer, 2010.

Thorpe, S. A.: Langmuir Circulation, Annu. Rev. Fluid Mech., 36, 55–79, 2004.

Tran-Thi, T.-H., Gustavsson, T., Prayer, C., Pommeret, S., and Hynes, J. T.: Primary ultrafast events preceding the photoinduced proton transfer from pyranine to water, Chemical Physics Letters, 329, 421–430, 2000.

Turney, D. E., Anderer, A., and Banerjee, S.: A method for three-dimensional interfacial particle image velocimetry (3D-IPIV) of an air-water interface, Meas. Sci. Technol., 20, 045 403; 1–12, doi: 10.1088/0957-0233/20/4/045403, 2009.

Van Doorne, C. W. H., Hof, B., Lindken, R. H., Westerweel, J., and Dierksheide, U.: Time resolved stereoscopic PIV in pipe flow. Visualizing 3D flow structures, in: Proceedings of 5th International Symposium on Particle Image Velocimetry. Busan, South-Korea, September 2003, 2003.

Veron, F. and Melville, W. K.: Experiments on the stability and transition of wind-driven water surfaces, J. Fluid Mech., 446, 25–65, doi: 10.1017/S0022112001005638, 2001.

Walker, J. W. and Peirson, W. L.: Measurement of gas transfer across wind-forced wavy air–water Interfaces using laser-induced fluorescence, Exp. Fluids, 44, 249–259, doi: 10.1007/s00348-007-0398-8, 2008.

Wang, B., Liao, Q., Bootsma, H. A., and Wang, P.-F.: A dual-beam dual-camera method for a battery-powered underwater miniature PIV (UWMPIV) system, Exp. Fluids, 52, 1401–1414, doi: 10.1007/s00348-012-1265-9, 2012.

Ward, B.: Air-water interfacial temperature measurements, in: Transport at the Air Sea Interface — Measurements, Models and Parameterizations, edited by Garbe, C. S., Handler, R. A., and Jähne, B., chap. Air–Water Interfacial Temperature Measurements, Springer-Verlag, doi: 10.1007/978-3-540-36906-6_14, 2007.

Warken, P.: Hochauflösende LIF-Methode zur Messung von Sauerstoffkonzentrationsprofilen in der wasserseitigen Grenzschicht, Diplomarbeit, Institut für Umweltphysik, Fakultät für Physik und Astronomie, Univ. Heidelberg, 2010.

Winter, R.: Fluorescent Tracers for air-sided Concentration Profile Measurements at the Air-Water Interface, Dissertation, Institut für Umweltphysik, Fakultät für Physik und Astronomie, Univ. Heidelberg, URL http://www.ub.uni-heidelberg.de/archiv/12105, 2011.

Wolfbeis, O. S., Fürlinger, E., Kroneis, H., and Marsoner, H.: Fluorimetric analysis 1. A study on fluorescent indicators for measuring near neutral ("physiologieal") pH-values, Fresenius Z. Anal Chem, 314, 119–124, doi: 10.1007/BF00482235, 1983.

Xu, G. and Zhang, Z.: Epipolar Geometry in Stereo, Motion and Object Recognition, Kluwer Academic Publishers, Dordrecht, The Netherlands, 1996.

Yaws, C. L.: Chemical Properties Handbook: physical, thermodynamic, environmental, transport, safety, and health related properties for organic and inorganic chemicals, McGraw-Hill, 1999.

Zang, W. and Prasad, A. K.: Performance evaluation of a Scheimpflug stereocamera for particle image velocimetry, Appl. Optics, 36, 8738–8744, doi: 10.1364/AO.36.008738, 1997.

Zappa, C. J., Asher, W. E., and Jessup, A. T.: Microscale wave breaking and air-water gas transfer, J. Geophys. Res., 106, 9385–9391, doi: 10.1029/2000JC000262, 2001.

Zollhofer, M., Niessner, M., Izadi, S., Rehmann, C., Zach, C., Fisher, M., Wu, C., Fitzgibbon, A., Loop, C., Theobalt, C., et al.: Real-time non-rigid reconstruction using an rgb-d camera, ACM Transactions on Graphics, TOG, 4, 2014.

A. Calculations of transfer velocities from partitioning of the gas exchange

The fluxes of ammonia in the air and water side of the facility can be described as:

$$j_a = k_a([\mathrm{NH_3}]_{\mathrm{b,a}} - [\mathrm{NH_3}]_{\mathrm{s,a}}) \tag{A.1}$$

$$j_w = k_w([\mathrm{NH_{aq}}]_{\mathrm{s,w}} - [\mathrm{NH_{aq}}]_{\mathrm{b,w}}) \tag{A.2}$$

with the air- and water-side transfer velocities k_a and k_w, the ammonia concentration in the air bulk $[\mathrm{NH_3}]_{\mathrm{b,a}}$ and at the surface $[\mathrm{NH_3}]_{\mathrm{s,a}}$, the water-side concentration of ammonia and ammonium at the surface $[\mathrm{NH_{aq}}]_{\mathrm{s,w}}$ and in the bulk $[\mathrm{NH_{aq}}]_{\mathrm{b,w}}$.

With mass conservation, the fluxes in the water and air side are equal, that results in the relation of k_a and k_w:

$$\frac{k_a}{k_w} = \frac{([\mathrm{NH_{aq}}]_{\mathrm{s,w}} - [\mathrm{NH_{aq}}]_{\mathrm{b,w}})}{[\mathrm{NH_3}]_{\mathrm{b,a}} - [\mathrm{NH_3}]_{\mathrm{s,a}}} \tag{A.3}$$

As the exchange of ammonia is air-side controlled, the surface concentration $[\mathrm{NH_3}]_{\mathrm{s,a}}$ is much small than the bulk air concentration $[\mathrm{NH_3}]_{\mathrm{b,a}}$. Additionally, the ammonia concentration for pH > 8 is much snaller than the ammonium concentration, the eq. (A.3) can be simplified:

$$\frac{k_a}{k_w} = \frac{([\mathrm{NH_4^+}]_{\mathrm{s,w}} - [\mathrm{NH_4^+}]_{\mathrm{b,w}})}{[\mathrm{NH_3}]_{\mathrm{s,a}}} \tag{A.4}$$

As the fluxes of ammonium and hydrogen in the water must be opposite and equal due to charge conservation, the ratio of k_a and k_w is written as:

$$\frac{k_a}{k_w} = \frac{([\mathrm{H^+}]_{\mathrm{b,w}} - [\mathrm{H^+}]_{\mathrm{s,w}})}{[\mathrm{NH_3}]_{\mathrm{s,a}}} \tag{A.5}$$

Finally, in the case of acid water at the start of the experiments, the pH value is small (high concentration of $\mathrm{H^+}$) and increases at the water surface only, therefore the the surface concentration of hydrogen can be neglected:

$$\frac{k_a}{k_w} = \frac{[\mathrm{H^+}]_{\mathrm{b,w}}}{[\mathrm{NH_3}]_{\mathrm{s,a}}} \tag{A.6}$$

The air-sided concentration of ammonia has been monitored using UV spectrometer as described in sec. 4.2.1. An example of temporal change of air-sided ammonia concentration for lowest turbine frequencies of 5 Hz is presented in fig. A.1.

In order to get integrated transfer velocities, the air-sided concentration has be fitted to an exponential function:

$$c(t) = x_0 + x_1(1 - exp(-\lambda t)) \tag{A.7}$$

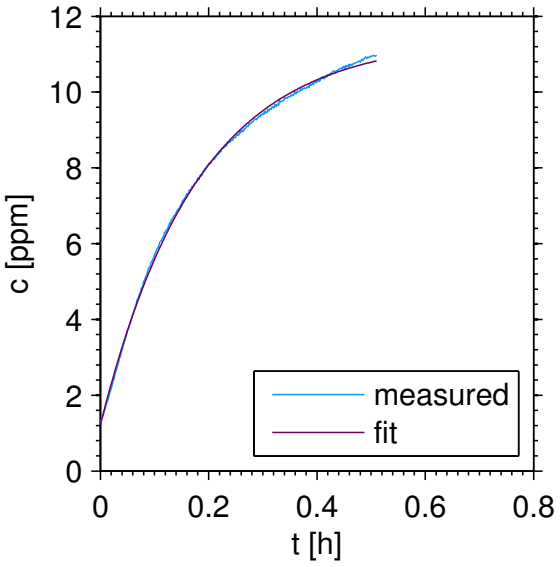

Figure A.1.: Estimation of the transfer velocity. Fir of the air-side concentration of ammonia over time at a wind speed of 2.46 cm/s. The blue line shows the measured concentration and the purple line - the fit of the data.

With fitting the exponential function to the air-sided concentration of ammonia, the transfer velocity can be estimated as:

$$k = \lambda h_a \tag{A.8}$$

where h_a is the height of the air space of the facility.

The water-side transfer velocity k_w and, hence, the water-side mass boundary layer can be estimated using the definition of total transfer velocity (or total resistance) according to:

$$R_{tot} = \alpha R_a + R_w \tag{A.9}$$

With known relation of resistances R_a and R_w, the water-sided transfer velocity is defined as:

$$k_w = 1/R_w = \frac{1}{C\alpha R_{tot}} \tag{A.10}$$

With estimated k_w, the mass boundary layer thickness at the water side z_*^w can be calculated with known diffusivity constant. For the turbine frequency of 5 Hz, the mass boundary layer thickness at the water side was found to be equal to 0.8 mm.

B. Full Calibration of the Cameras and Image Rectification

The calibration of the cameras was performed using build-in function *cv2.stereoCalibrate* from *openCV* in *iPython*. The criteria and flags for this function was set up to (cv2.TERM-CRITERIA-MAX-ITER + cv2.TERM-CRITERIA-EPS, 100, $1 \cdot 10^{-6}$) and (cv2.CALIB-FIX-ASPECT-RATIO + cv2.CALIB-FIX-INTRINSIC).

The rectification maps for the left and right camera were estimated using *cv2.initUndistortRectifyMap* function. The function computes the undistortion and rectification transformation map. The transformation map for the left and right camera are presented in fig. B.1.

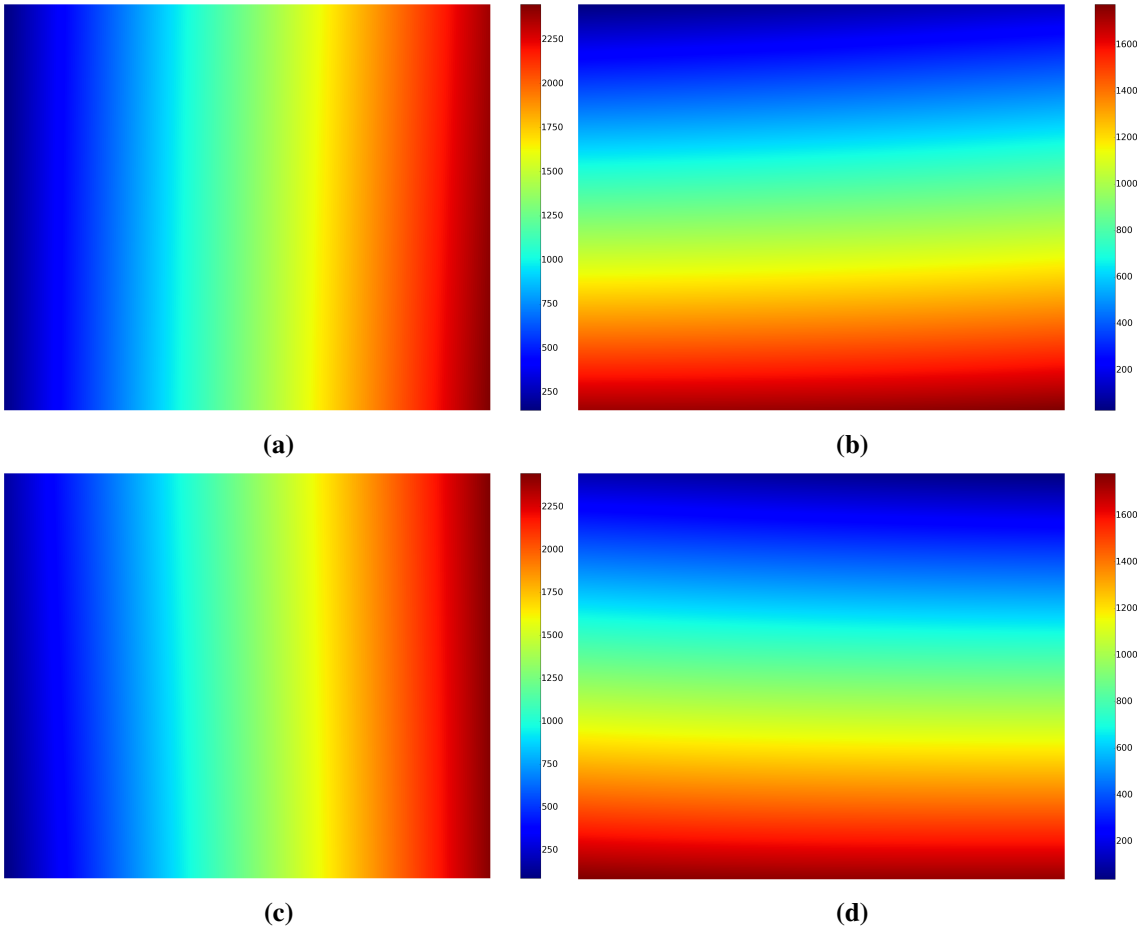

Figure B.1.: Transformation maps for the (a),(b) left and (c),(d) right camera in x- and y-direction.

The undistorted image looks like original, as if it is captured with a camera using modified camera matrix and zero distortion. Also, it orients the camera differently in the coordinate space, according to R matrix. That, for example, helps to align two heads of a stereo camera so that the epipolar lines on both images become horizontal and have the same y- coordinate (in case of a horizontally aligned stereo camera).

The function builds the maps for the inverse mapping algorithm that is used further by function *remap()*. For each pixel in the corrected and rectified image, the function computes the corresponding coordinates in the source image (in the original image from camera).

C. Stereo Dense Reconstruction

In order to estimate the distance of a pixel to the camera, the function *cv2.reprojectImageTo3D* was used. The function reprojects a disparity image to 3D space with transforming a single-channel disparity map to a 3-channel image. Example of a single frame for the condition of turbine frequency of 7 Hz with no AC working is presented in fig. C.1.

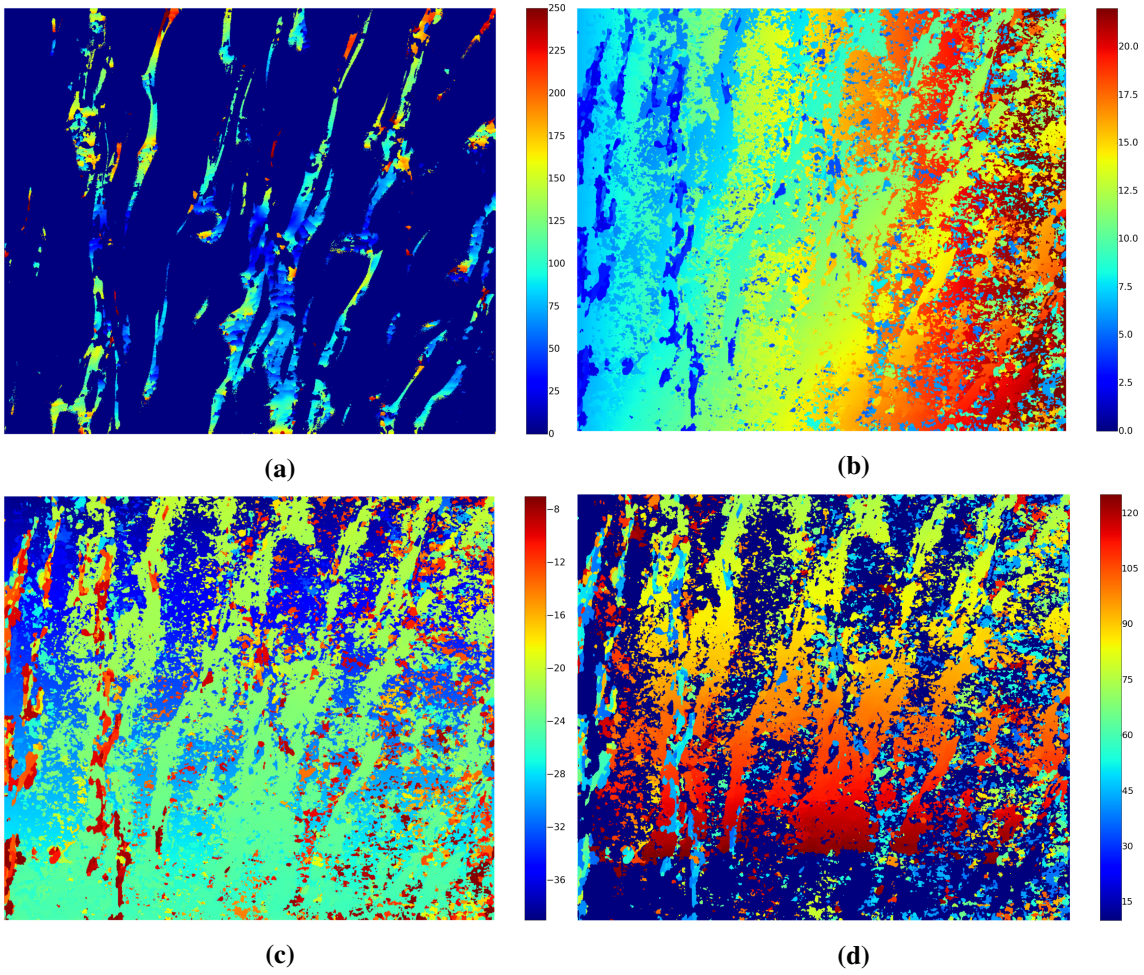

Figure C.1.: (a) The disparity map for arbitrary frame. The estimated coordinates for each pixel in (b) cross wind, (c) along wind and (d) vertical directions.

The area with no fluorescence were not eliminated from the images in order to notice the gradient in the distances from the camera in cross wind, along wind and vertical directions.

D. Disparity Map Sequences for Different Wind Conditions

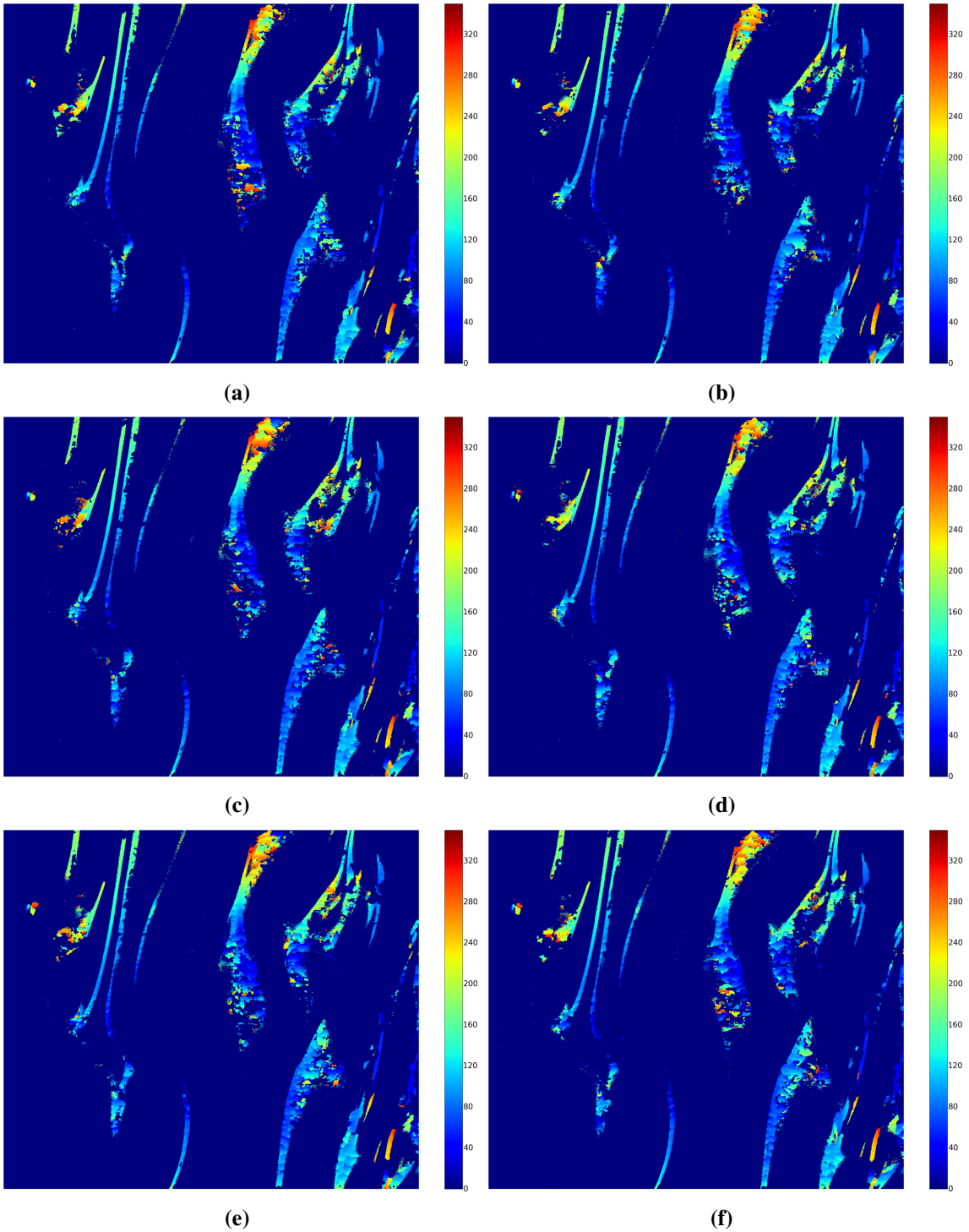

Figure D.1.: Sequence of the disparity map at a reference wind speed of 1.52 m/s.

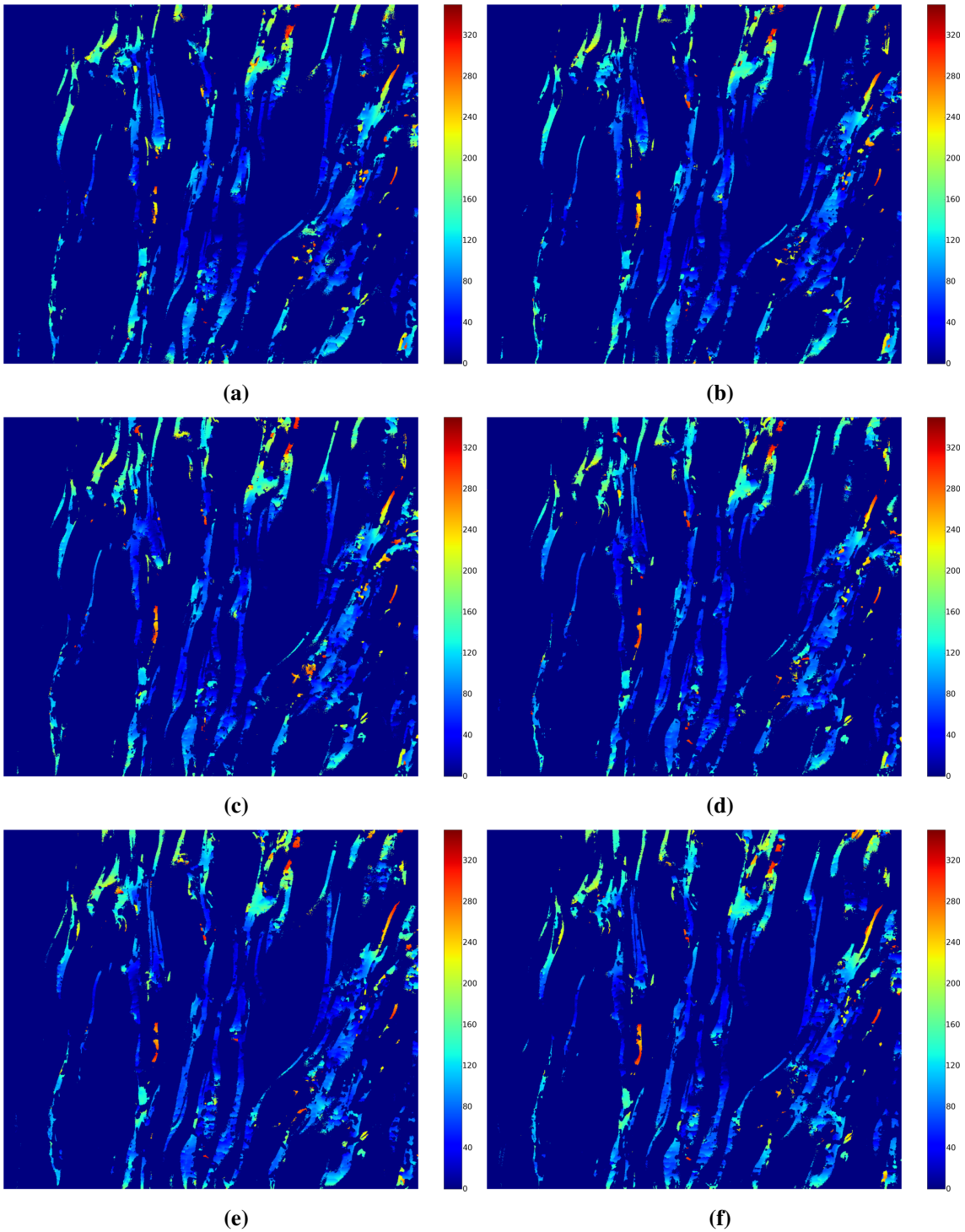

Figure D.2.: Sequence of the disparity map at a reference wind speed of 2.16 m/s.

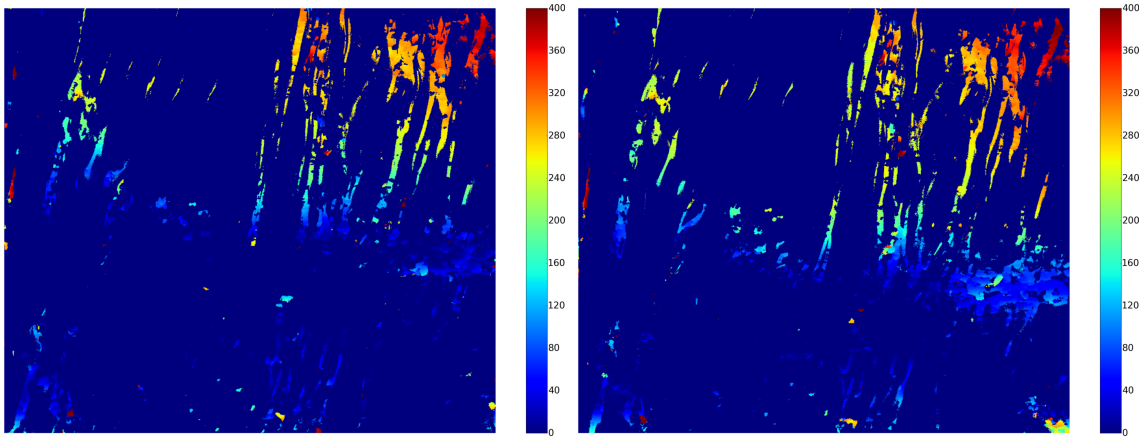

(a) (b)

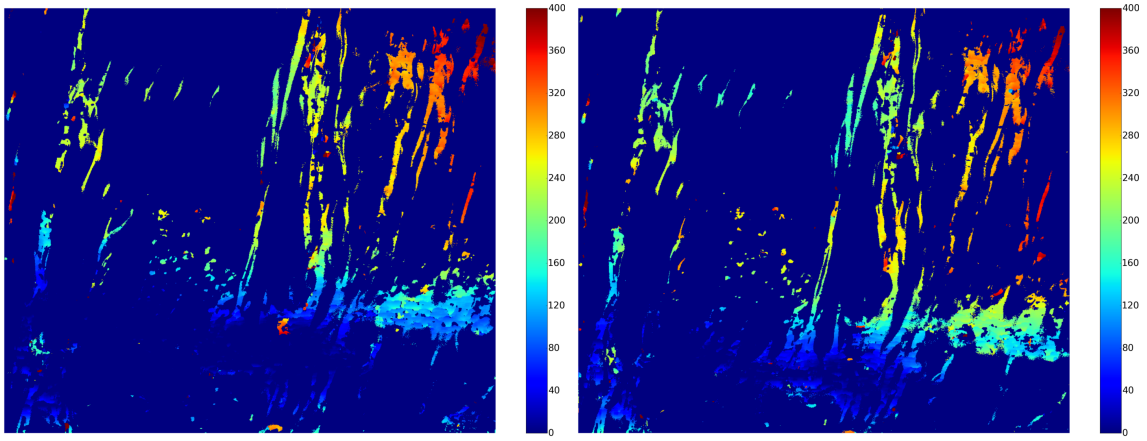

(c) (d)

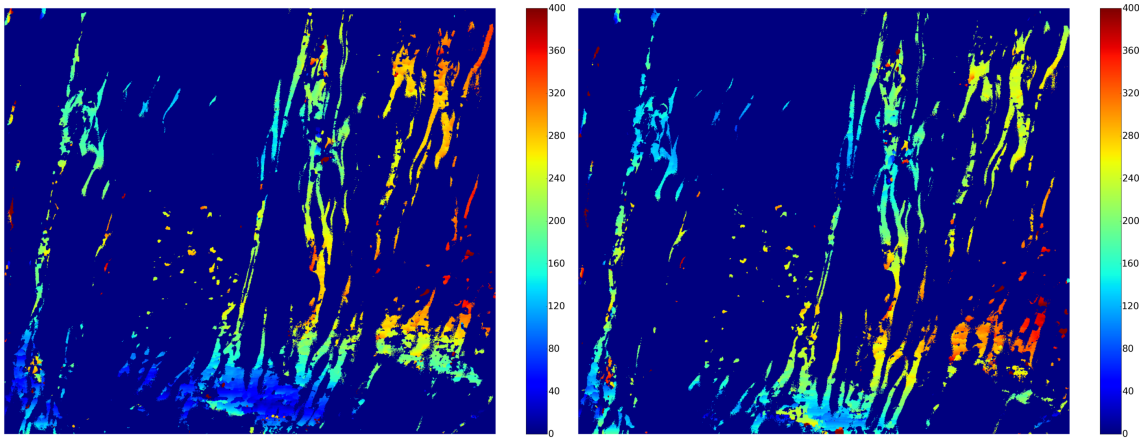

(e) (f)

Figure D.3.: Sequence of the disparity map at a reference wind speed of 3.88 m/s.

Acknowledgements

I am very grateful to Prof. Bernd Jähne for trusting me with such a challenging project and supporting me during my PhD work.

I thank Prof. Kurt Roth for reviewing my thesis. I thank Prof. Tilman Plehn and Prof. Ulrich Uwer for agreeing to be a part of my oral exam committee.

I would like to acknowledge the great help from Barbara Werner and Karin Kruljac with all bureaucracy I needed to go through.

I acknowledge the funding from GRK1114 Graduiertenkolleg and lots of travel support from IWR Graduate School.

There is no way I can manage to thank everyone that has been involved in my PhD life. But here is a try.

My first big “thank you“ goes to Christine Kräuter and Wolfgang Mischler for handling me for the last couple of months. I would never be able to find courage for finishing and to manage so many things at once, if it was not with their help, support and, most importantly, their friendship. They did a great job in correcting most of my thesis and in teaching me how to use the articles. It was such a pleasure to be a part of our pathetic team. I thank Daniel Kiefhaber for proof reading a great part of my thesis and holding some “big picture“ talks with me (I have to say, number of sleepless nights goes into his count). I thank Günther Balschbach for many discussions during coffee breaks and most nicest corrections of my theory and introduction chapters. I thank the members of air-sea interaction group - Max Bopp, Kerstin Krall and Jakob Kunz - for creating a healthy in some way atmosphere that was a pleasure to work in. I thank the former members of the group - Nils Krah, Felix Friedl, Roland Rocholz, Leila Nagel, Svenja Reith and Marcel Gutsche - for many talks and great help at the start of my PhD.

I thank Katrin Honaüer, who was willing to help and struggle together over the code for the stereo algorithm. I do not think I would get such nice disparity maps without her involvement.

I thank my office mates, Therese Weißbach and Sebastian Kazarski, for being patient with me and Felix Reixinger for providing me with countless advices on color maps and notations to use.

I am grateful to all my friends for a huge amount of support I was receiving. I am thankful to Anna Burdukova, Eugenia Neumann, Emre Hidalgo, Elena Facco and Luca Fiaschi - just to name a few. I thank many of my climbing friends, Christian Schomann and Jürgen Gutekunst in particular, for distracting and motivating me whenever either one was needed.

I have to admit, staying away from my family for such a long time was not as easy as I expected. Luckily, I was getting plenty of love, attention and anxiety through tons of emails, messages and skype conversations. I have to say big thank you to my father, Vladimir Trofimov, for “driving by“ over 1700 km just for spending couple of hours with me (not once he did that). I thank my mother,

Tatiana Trofimova, who, I know, was thinking and worrying about me during the last three years. I am grateful to my elder sisters, who have always been a good example for me. I thank my sister Alexandra for taking a look at the first draft of my thesis, for doing such a great work with 3D sketch and also for being so loyal to me during my studies back in Minsk. I thank my sister Maria for her great support, trust in my efforts and her kind cheering-up messages.

I thank my best friend, Marat Seroglazov, for being such a devoted and faithful friend to me despite everything, for a constant encouragement, motivation and inspiration of my efforts during much longer time than the last three years. He managed to help me out with so many sentimental struggles I had and not only.

Finally, I thank my spiritual teacher and greatest friend, Anastasia Melissi, whom I was lucky enough to meet in the first year of my PhD studies. I thank her for talking me through the most valuable lessons I've learned so far and taking great care of me.